

The Arizona-Montréal spectroscopic survey of hot subluminous stars [★]

M. Latour¹, E. M. Green², M. Dorsch³, V. Van Grootel⁴, P. Chayer⁵, S. Charpinet⁶, U. Heber⁷, S.K. Randall⁸, and X.-Y. Ma⁴

¹ Institut für Astrophysik und Geophysik, Georg-August-Universität Göttingen, Friedrich-Hund-Platz 1, 37077 Göttingen, Germany
 e-mail: marilyn.latour@uni-goettingen.de

² Steward Observatory, University of Arizona, 933 N. Cherry Avenue, Tucson, AZ 85721, USA

³ Institut für Physik und Astronomie, Universität Potsdam, Haus 28, Karl-Liebknecht-Str. 24/25, 14476 Potsdam, Germany

⁴ Space sciences, Technologies and Astrophysics Research (STAR) Institute, Université de Liège, 19C Allée du 6 Août, B-4000 Liège, Belgium

⁵ Space Telescope Science Institute, 3700 San Martin Drive, Baltimore, MD 21218, USA

⁶ Institut de Recherche en Astrophysique et Planétologie, CNRS, Université de Toulouse, CNES, 14 Avenue Edouard Belin, 31400 Toulouse, France

⁷ Dr. Karl Remeis-Observatory and Erlangen Centre for Astroparticle Physics, Friedrich-Alexander-Universität Erlangen-Nürnberg, Sternwartstr. 7, 96049 Bamberg, Germany

⁸ ESO, Karl-Schwarzschild-Str. 2, 85748 Garching bei München, Germany

Received 19/09/2025; accepted 3/11/2025

ABSTRACT

Context. Hot subdwarf B (sdB) and O (sdO) type stars are evolved helium-burning objects that lost their hydrogen envelope before the helium flash when their progenitors were close to the tip of the red giant branch. They populate the extreme horizontal branch (EHB) in the Hertzsprung-Russel diagram (HRD). The mass distribution of canonical hot subdwarfs is expected to peak at the core mass required for helium ignition under degenerate conditions, in the 0.45 to 0.5 M_{\odot} range. However, non-degenerate helium ignition from intermediate-mass progenitor and non-canonical pathways, such as the merger of helium white dwarfs and delayed helium flashes, are also expected to contribute to the hot subdwarf population.

Aims. Using the high-quality, homogeneous spectra of 336 hot subluminous star candidates from the Arizona-Montréal Spectroscopic Survey, we aim to improve our understanding of the atmospheric and stellar properties of hot subdwarf stars. Our focus is on the mass distribution of the different types of hot subdwarfs and their connections to the various formation scenarios.

Methods. We used large grids of model atmospheres to fit the observed spectra and derived their atmospheric parameters: effective temperature (T_{eff}), surface gravity, and helium abundance. The model grids were further utilized to fit the spectral energy distribution of each star and the *Gaia* parallax was used to compute the stellar parameters radius, luminosity, and mass.

Results. Our spectroscopic sample mostly consists of H-rich sdBs and sdOs, but also contains 41 He-rich sdOs. Additionally, the sample includes 11 intermediate-helium stars and 19 horizontal branch objects with $T_{\text{eff}} \gtrsim 14$ kK. We detected the presence of helium stratification in six sdB stars with T_{eff} around 30 kK, making them good candidates for also showing ^3He enrichment in their atmospheres. Our sdB distribution along the EHB shows a gap near 33 kK, visible in both the Kiel ($\log g - T_{\text{eff}}$) diagram and HRD, corroborating previous observations and predictions. The mass distributions of H-rich sdBs and sdOs are similar and centered around 0.47 M_{\odot} , consistent with the canonical formation scenario of helium ignition under degenerate conditions. Among the H-rich hot subdwarfs, we found no difference between the mass distributions of close binaries and apparently single stars. The He-sdOs have a significantly wider mass distribution than their H-rich counterparts, with an average mass of about 0.78 M_{\odot} . In the HRD, the He-sdOs lie on the theoretical helium main sequence for masses between 0.6 and 1 M_{\odot} . This strongly favors a merger origin for these He-rich objects. We identified a small number of candidate low-mass ($< 0.45 M_{\odot}$) sdBs located below the EHB that might have originated from more massive progenitors. These low-mass sdBs preferentially show low helium abundances. Finally, we identified more than 80 pulsating stars in our sample and find these to fall into well-defined p - and g -mode instability regions.

Key words. Stars: subdwarfs – Stars: horizontal branch – Stars: atmospheres – Stars: fundamental parameters – Hertzsprung-Russell and C-M diagrams

1. Introduction

The majority of hot subdwarf B and O type stars (sdBs and sdOs) are evolved helium-burning objects that have been stripped of their hydrogen envelope before the helium flash, when their low-mass ($\lesssim 2.3 M_{\odot}$) progenitors were at the tip of the red giant branch (RGB, Heber 2009, 2016, 2024). This is what is re-

ferred to as the canonical formation scenario (Sweigart 1987; Dorman et al. 1993). Hot subdwarfs essentially sit at the very hot end of the horizontal branch and are also referred to as extreme horizontal-branch stars (EHB). The mass distribution of the canonical hot subdwarfs is expected to peak at the core mass required for helium ignition under degenerate conditions, which lies in the 0.45–0.5 M_{\odot} range (Iben 1967; Sweigart 1987; Salaris & Cassisi 2005). The evolution of intermediate-mass progenitors ($\gtrsim 2.3 M_{\odot}$), igniting core-He burning under non-degenerate

[★] Dedicated to the memory of Prof. Gilles Fontaine

conditions, is expected to produce lower core and total masses, down to $\sim 0.33 M_{\odot}$ (Montalbán & Noels 2013; Noels-Grotsch & Miglio 2025). The part of the Hertzsprung-Russell diagram (HRD) where hot subdwarfs are located can also be crossed by stars in other evolutionary phases, such as low-mass post asymptotic giant branch (post-AGB, Heber 1991) stars and stars cooling down as He-core white dwarfs (WDs, Driebe et al. 1998; Istrate et al. 2016). More exotic stellar products, resulting from the merger of, among other possibilities, two He-core WDs, can also end up as core-He burning objects and be found close to the EHB and the adjacent helium main sequence in the HRD (Webbink 1984; Saio & Jeffery 2002).

One way to disentangle the various evolutionary phases populating the HRD in the hot subdwarf region is via the masses of the stars. However, precise stellar mass measurements independent of evolutionary tracks can readily be obtained only for certain special cases, such as eclipsing binary systems. For hot subdwarfs, it has also been possible to derive accurate masses from asteroseismology for pulsating sdBs (Charpinet et al. 2002, 2005b) and through light-curve modeling coupled with spectroscopic observations for close binaries exhibiting eclipses, reflection effects, or ellipsoidal deformations (Vučković et al. 2007; For et al. 2010). A compilation of literature masses derived for 22 hot subdwarf pulsators and binaries led to a first empirical mass distribution for hot subdwarfs, peaking at $0.47 M_{\odot}$ with a narrow range of $0.44\text{--}0.50 M_{\odot}$ containing 68% of the stars (Fontaine et al. 2012). This aligned very well with the expectations from canonical stellar evolution theory. Moreover, the seismic models obtained for the 14 pulsators in the sample yielded predicted distances in good agreement with the parallaxes from the second *Gaia* Data Release (Fontaine et al. 2019).

The availability of accurate parallaxes, and thus distances, for most of the nearby ($\lesssim 3$ kpc) hot subdwarfs from the *Gaia* Data Release (EDR3, Riello et al. 2021) finally permits the mass to be estimated for large samples of hot subdwarfs based on the fit of their spectral energy distribution (SED). However, this requires a few additional key ingredients: observed magnitudes in different filters, theoretical model grids to compute the expected flux in these filters, and reliable estimates of the atmospheric parameters of the star, most notably the effective temperature and surface gravity (Heber et al. 2018). Mass distributions obtained from a combination of spectroscopic analysis, parallaxes and SED fits for a large sample of hot subdwarfs were first presented in Lei et al. (2023) using LAMOST spectra. While the authors found an average mass ($\sim 0.47 M_{\odot}$) in line with the theoretical expectations for their hydrogen-rich sdBs, their distribution is very broad, extending from 0.2 to $1.0 M_{\odot}$. Their mass distribution for hydrogen-rich sdO masses revealed itself to be unrealistically flat, with a very low mean mass of $0.36 M_{\odot}$. Similarly, the mass estimates of hot subdwarfs in globular clusters, whose distances are relatively well constrained by methods other than parallax measurements, remain systematically lower than expected, despite significant improvements in model atmospheres and data obtained over the years (see, e.g. Moni Bidin et al. 2011; Latour et al. 2018). Note that most of the dispersion seen in the mass distributions from parallaxes and SED fits in the literature is due to the uncertainty on the atmospheric parameters - especially the surface gravity, which dominates the error budget in the mass determination - rather than intrinsic to the stars themselves.

Atmospheric parameters derived from high-quality and homogeneous spectroscopic samples are crucial for minimizing the scatter in the masses derived from parallaxes and SED fits and yielding distributions of sufficient quality for a meaningful comparison to predictions from different formation scenarios

and population synthesis models (Han et al. 2002, 2003). This is what we aim to do with our samples of hot subdwarf spectra from the Arizona-Montréal spectroscopic program, whose early results were reported in conference proceedings (Green et al. 2004, 2005, 2008; Fontaine et al. 2014). The spectroscopic data consists of two samples with different wavelength coverage and resolution. The larger sample, which we refer to as the Bok sample, comprises spectra for 337 stars obtained at the 2.3m Bok telescope at the Kitt Peak observatory. The second sample consists of spectra for a subset of 116 stars (all from the Bok sample), observed with the MMT telescope. This sample is referred to as the MMT sample. All of these high-quality Bok and MMT spectra were fit with synthetic model spectra to estimate their atmospheric parameters: effective temperature (T_{eff}), surface gravity ($\log g$), and helium abundance ($\log N(\text{He})/N(\text{H})$). The atmospheric parameters were then used, along with the *Gaia* parallaxes and magnitudes from various photometric surveys, to perform SED fits and derive the stellar parameters: radius (R), luminosity (L), and mass (M).

We present the results of our work as follows. Sections 2 and 3 include the description of our observational material and analysis methods. Section 4 gives the results of our spectroscopic and SED fits for the Bok and MMT samples separately. In the discussion (Sect. 5), we focus on the mass distributions (Sects. 5.1 to 5.3) and examine the properties of the pulsating hot subdwarfs included in our sample in Sect. 5.4. Finally, a summary of our work and our main conclusions are presented in Sect. 6.

2. Observational material

2.1. Low-resolution Bok spectra

Low-resolution spectra for 336 hot subluminous star candidates were obtained by one of us (E.M.G) as part of a project aiming to better characterize the hot subdwarf population (Green et al. 2008). The stars were selected as relatively bright ($V \lesssim 14.5$) blue objects visible from Arizona. They were mainly identified from early small-scale surveys of blue objects, such as Palomar-Green (Green et al. 1986), Feige (Feige 1958), and Kitt Peak Downes (Downes 1986). All objects, except for the sdB binary NGC 188 2019 (Sandage 1962; Green et al. 2005), are members of the galactic field. The distances derived from the *Gaia* EDR3 parallaxes and the sky distribution of these 336 stars are shown in Fig. 1.

The spectra were obtained at the Bok 2.3m telescope of the Steward Observatory on Kitt Peak, mainly between 1999 and 2004. The standard setup for the spectroscopic survey was to use the Bollers & Chivens Cassegrain spectrograph with the 400 mm^{-1} first-order grating with a $2.5''$ slit. This results in a typical resolution of 9 \AA over the wavelength interval $3620\text{--}6900 \text{ \AA}$. Before each exposure, the instrument rotator was set to align with the parallactic angle. HeAr comparison spectra were taken immediately following the stellar exposures. The spectra were bias-subtracted, flat-fielded, background-subtracted, optimally extracted, wavelength-calibrated, and flux-calibrated using standard IRAF (Tody 1986, 1993) tasks. The flux calibration was performed using observations of the standard stars Feige 34 or BD+28°4211. All individual spectra were also corrected for heliocentric velocities. The number of observations per object varies from star to star but is typically between one and ten. For stars with more than one observation, the radial velocity (RV) was measured via cross-correlation with the highest S/N spectrum for each given star. The spectra were then aligned in radial

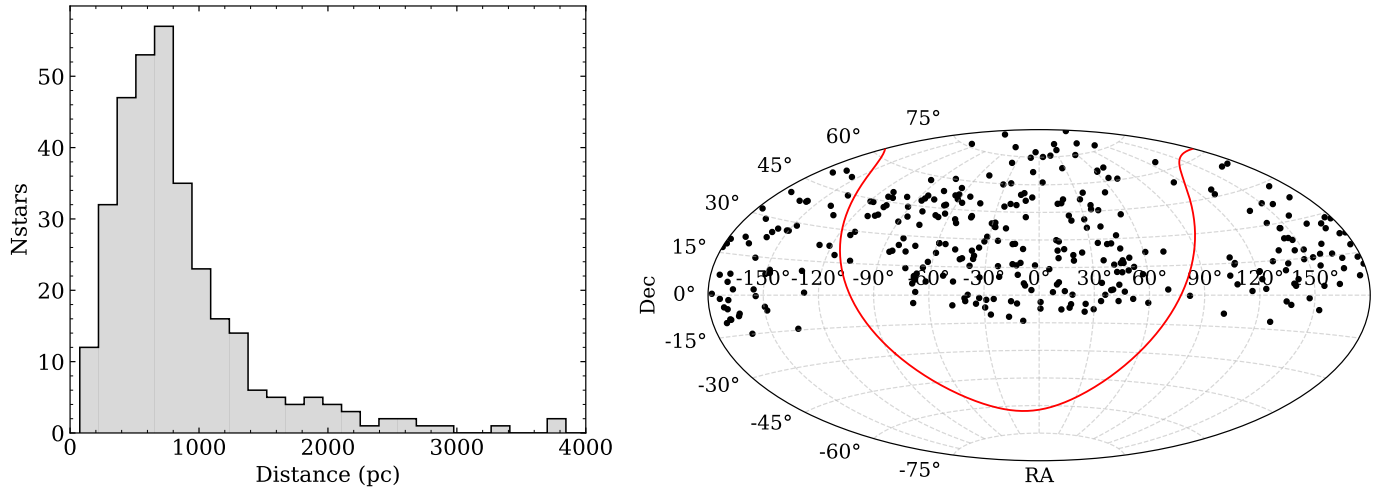


Fig. 1: Distance and sky distribution of the stars in the Bok sample. Six objects are located beyond 4000 pc, but they are all most likely MS B-type stars (see Sect. 4.1.2). The red line indicates the position of the galactic plane on the sky projection.

velocity prior to being combined into a single spectrum. We note that this way of extracting the RV is independent of synthetic spectra but provides only relative, rather than absolute, RVs. Except for a few faint objects, the signal-to-noise ratios (S/N) of the final spectra lie in the range 100–500. The median S/N of the sample is 197.

2.2. Medium-resolution MMT spectra

Additional medium-resolution spectra were obtained for a subset of 116 stars in the Bok sample by one of us (E.M.G.) with the blue spectrograph attached to the 6.5 m MMT telescope, between 1996 and 2003 as part of a radial velocity program (Green et al. 2004, 2005). Throughout the observing seasons, the same experimental setup was consistently used: the 832 mm^{-1} grating in second order and a $1''$ slit that provided a resolution R of ~ 4250 (1.0 \AA) over a wavelength range of $4000\text{--}4950 \text{ \AA}$. The spectra were reduced and combined in the same way as those obtained with the Bok telescope.

The MMT sample consists of hydrogen-rich sdBs and sdOs cooler than 45 kK . Again, a number (between 2 and 8) of individual spectra were combined. The S/N for the combined spectra typically ranges from 100 to 200. Exposure times were mostly kept below 15 min and depended on the brightness of the star. Fig. D.1 shows our MMT spectral atlas: the combined spectrum for each star, ordered by increasing effective temperature.

2.3. Light curves

Most of the stars in the MMT sample were also observed as part of a photometric monitoring campaign (see Green et al. 2003, 2004) by one of us (E.M.G.) at the 1.6m Kuiper Telescope at Mount Bigelow (Steward Observatory) and at the 2.3m Telescope on Kitt Peak with conventional 2K CCDs binned 3×3 ($0.45'' \text{ pixel}^{-1}$). Integration times were kept short, between 10 and 60 s, depending on the brightness of the target. The stars were typically observed for a total duration of 2 to 20 hours. Differential magnitudes were derived from aperture photometry of the sdB relative to reference stars of comparable magnitude within each frame. As a result of these observations, we have information on the pulsation properties for all but six stars in

the MMT sample, and can classify them as rapid (p -mode), slow (g -mode) or hybrid pulsators, or non-pulsating objects.

Given that these ground-based observations date from earlier than 2005, many of the targets have since also been monitored for variability from space. We cross-checked our information from the ground-based data with the light curves obtained from the Transiting Exoplanet Survey Satellite (TESS, Ricker et al. 2014). For all stars in our Bok sample, we retrieved and examined, when available, the Lomb-Scargle Periodograms of the TESS data, using our dedicated software FELIX (Charpinet et al. 2010; Zong et al. 2016), to search for pulsation signals. In addition, we searched for pulsators among the list of sdB pulsators from the Kepler extended K2 mission (W. Zong, priv. comm.) and the literature compilation of pulsators made by Uzundag et al. (2024). In total, we identified 22 p -mode pulsators, 53 g -mode pulsators, and 9 hybrid pulsators in our sample. The light-curves of 201 stars did not show any signal that could be associated with p - or g -modes pulsations and we classified them as non-pulsating. Finally, 44 stars do not have TESS light-curves and their pulsation status remains unknown. The pulsating stars and their properties are further discussed in Sect. 5.4.

3. Analysis Methods

3.1. Atmospheric parameters

Our samples include a large variety of hot subluminous stars, from cool blue horizontal branch (BHB) stars to extremely helium-enhanced sdO stars. In order to cover all the atmospheric parameter ranges of these stars, two different types of model atmospheres were used.

For the spectral fit of the hydrogen-rich hot subdwarfs and BHB stars, we used the grids of hybrid LTE/NLTE models that have been used in similar studies (e.g., Geier et al. 2024, Heber et al., in prep., Dawson et al., in prep.). The model grid extends from 9 kK to 75 kK , from $\log g = 3.0$ to 7.0 , and from $\log N(\text{He})/N(\text{H}) = -5.0$ to 2.5 . The lower limit on the surface gravity gradually increases to $\log g = 5.25$, for models at 75 kK , with increasing effective temperature, following the Eddington limit (see Heber et al., in prep. for a figure showing the grid coverage). The models are constructed using the combination of ATLAS12/DETAIL/SURFACE (ADS) codes. ADS is a hybrid LTE/NLTE

method, which was first developed by [Przybilla et al. \(2006\)](#) and [Nieva & Przybilla \(2007\)](#) and further improved by [Przybilla et al. \(2011\)](#) and [Irrgang et al. \(2014, 2018, 2021, 2022\)](#). The improvements include a proper treatment of level dissolution for hydrogen ([Hubeny et al. 1994](#)) and the implementation of the Stark broadening line profiles of hydrogen and He I ([Tremblay & Bergeron 2009](#); [Beauchamp et al. 1997](#)). The synthetic spectra are obtained by running the three codes mentioned above in succession. First, a LTE line-blanketed, plane-parallel, homogeneous and hydrostatic model atmosphere is calculated using ATLAS12 ([Kurucz 1996](#)). The LTE atmospheric structure is then used by DETAiL ([Giddings 1981](#); [Butler & Giddings 1985](#)) to calculate the population numbers of hydrogen and helium ([Przybilla & Butler 2004](#); [Przybilla 2005](#)) assuming NLTE and appropriate model atoms. The other chemical species are treated in LTE. In this work, we use metal abundances that reflect the typical abundance patterns of hot subdwarfs (see e.g. [Blanchette et al. 2008](#); [Pereira 2011](#); [Naslim et al. 2013](#)). Most notably, iron-peak elements are enhanced by a factor of 10 with respect to solar, except iron itself which is kept at the solar value. The final synthetic spectra are computed with SURFACE ([Giddings 1981](#); [Butler & Giddings 1985](#)) and include only lines of hydrogen and helium.

The second type of model atmospheres we used are tailored to the helium-enhanced objects. These models were used in [Dorsch \(2024\)](#) and are described in their section 2.2. The model atmospheres and synthetic spectra were computed with TLUSTY, version 205, and SYNSPEC, version 51 ([Hubeny & Lanz 2011a,b](#), but see also [Hubeny & Lanz 2017a,b,c](#) for the specificity of the versions used here), respectively. They are NLTE models that include line-blanketing from C, N, O, Ne, Si, P, S, Fe, and Ni. The abundances are set to the solar values ([Asplund et al. 2009](#)) except for C (2× solar), O (0.1× solar), Ne (2× solar), Fe (1.5× solar), and Ni (10× solar), which roughly represents the abundance patterns of most helium-enriched hot subdwarfs. Specific improvements were made in SYNSPEC regarding the treatment of He I, the most important being the consideration of Stark broadening following the line profiles calculated by [Beauchamp et al. \(1997\)](#) and implemented in SYNSPEC by [Bédard et al. \(2020\)](#). For the He I lines at 4472 Å and 4922 Å, the Stark profiles of [Gigosos & González \(2009\)](#) and [Lara et al. \(2012\)](#) were used. The grid extends from $T_{\text{eff}} = 25$ to 65 kK, from $\log g = 3.0$ to 6.5 and from $\log N(\text{He})/N(\text{H}) = -1.75$ to +4.0. However, the lower limit on the surface gravity gradually reaches $\log g = 4.5$ (for models at 65 kK) as the effective temperature increases, following the Eddington limit.

The atmospheric parameters, namely T_{eff} , $\log g$, and $\log N(\text{He})/N(\text{H})$, were derived for each stellar spectrum using a full spectral fit to one of the model grids described above. The fit to a given star is not restricted to one specific grid, instead, the best-fit solution can be found in either of the two grids, as long as the parameters do not lie on the grid's edge. These fits were performed using the *Interactive Spectral Interpretation System* (ISIS, [Houck & Denicola 2000](#)) with a modified version of the χ^2 -minimization method presented by [Irrgang et al. \(2014\)](#). The spectral continuum was modeled using a spline with anchor points spaced every 100 Å, but avoiding the hydrogen and helium lines. This continuum spline was fitted simultaneously with the atmospheric parameters, which is necessary to account for correlations.

3.2. Spectral energy distribution and stellar parameters

To complement the spectral analysis, we also derive the stellar radius, luminosity, and mass for each star by performing a fit of its SED combined with the *Gaia* parallax. The method was first described in [Heber et al. \(2018\)](#) and is explained in more detail in section 2.3 of [Dorsch \(2024\)](#). Here we briefly summarize the main points. For each star, observed magnitudes are queried via Table Access Protocol (TAP) using the Astronomical Data Query Language (ADQL). This way, many photometric surveys can be queried through the VizieR database or other databases like the Astro Data Lab ([Fitzpatrick et al. 2014](#)). Some of the major surveys providing magnitudes for the stars in our sample are the Sloan Digital Sky Survey (SDSS, [Alam et al. 2015](#)), the Two Micron All Sky Survey (2MASS, [Skrutskie et al. 2006](#)), Pan-STARRS DR2 ([Flewelling 2018](#)), GALEX ([Bianchi et al. 2017](#)), and *Gaia* ([Riello et al. 2021](#)). Also relevant here are the *Gaia* DR3 photometric low-resolution spectra ([De Angeli et al. 2023](#)) that were used to construct a sequence of 14 box filters. An exhaustive list of the photometric catalogs queried is presented in [Culpan et al. \(2024\)](#).

During the SED fit procedure, the distance to the star is kept fixed to the value derived from the *Gaia* EDR3 parallax (ϖ). We correct the parallax for its zero-point offset following [Lindegren et al. \(2021\)](#) and inflate the corresponding uncertainty using the function suggested by [El-Badry et al. \(2021\)](#). The effective temperature, $\log g$, and helium abundance of the star are fixed to the value obtained from the spectroscopic fit of the Bok spectra. Thus the only parameters left to optimize are the angular diameter, $\Theta = 2R/D$, or in terms of the parallax, $\Theta = 2\varpi R$, as well as the interstellar colour excess $E(44 - 55)$ ¹. To account for interstellar extinction, we use the functions of [Fitzpatrick et al. \(2019\)](#) and adopt the standard parameter $R(55) = 3.02$. The model atmospheres used to compute the synthetic fluxes in the various photometric passbands are the same as used for the spectroscopic fits, i.e. the emergent flux from ATLAS12 and TLUSTY, including metal lines. From the value of Θ we directly obtain the radius R of the star and we compute the luminosity and the mass via the formulae

$$L = 4\pi R^2 \sigma T_{\text{eff}}^4 \quad \text{and} \quad M = \frac{gR^2}{G}.$$

All uncertainties are propagated using the Monte Carlo method; the resulting best-fit values (for R , L , M) are stated as the median with the 68% (1σ) uncertainties. For these computations, we included systematic uncertainties, alongside the statistical uncertainties, for the spectroscopic T_{eff} and $\log g$ measurements, adding them in quadrature following the prescription detailed in [Dawson et al. \(in prep.\)](#). The authors used their spectroscopic observations of hot subdwarfs within 500 pc to characterize systematic uncertainties arising from three sources: variability in data reduction, offsets between different instruments, and the choice of metallicity in the model atmospheres used to fit the spectra. As a result, they provided third-order polynomial functions to evaluate systematic uncertainties as a function of T_{eff} , for the three atmospheric parameters (T_{eff} , $\log g$, and, $\log N(\text{He})/N(\text{H})$). The systematic uncertainties are about 0.07 dex for $\log g$ and 1.5 % for T_{eff} , although the uncertainty on T_{eff} steadily increases to 5% for stars hotter than 40 kK. The surface

¹ $E(44 - 55)$ is analogous to $E(B - V)$, but with the monochromatic measures of the extinction at 4400 and 5500 Å substituting for measurements with the B and V filters. Conversion factors to the UBV systems are given in table 4 of [Fitzpatrick et al. \(2019\)](#). They are close to 1 for hot stars.

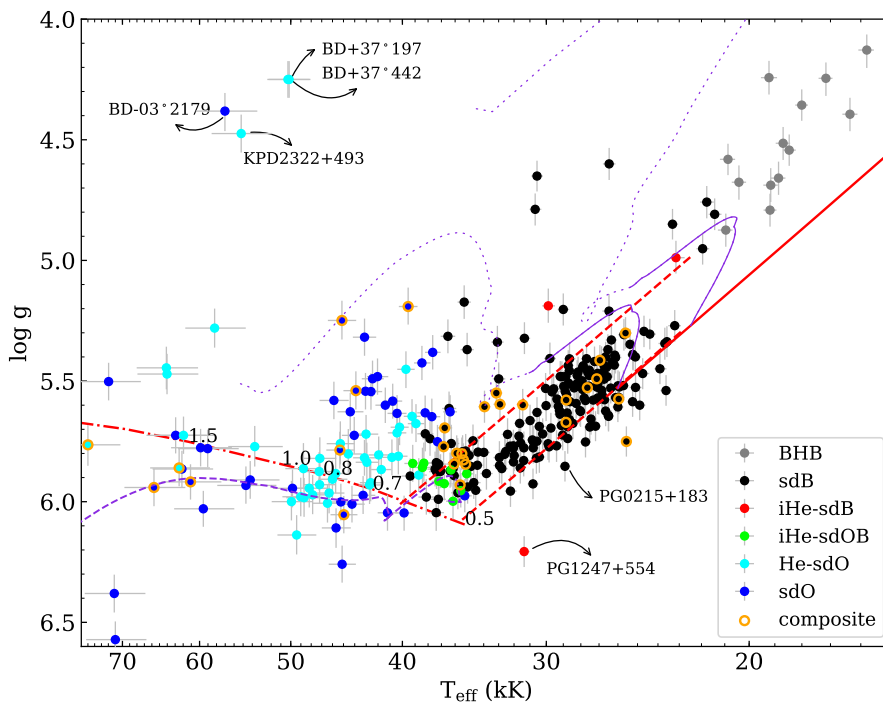


Fig. 2. Surface gravity ($\log g$) as function of T_{eff} (Kiel diagram) for the stars in the Bok sample. The six spectral groups are indicated with symbols of different colors. Stars with IR excess are marked with an additional orange circle (see Sect. 4.1.2). The ZAEHB and TAEHB computed with STELUM for a core mass of $0.47 M_{\odot}$ are shown with red dashed lines. The ZAEHB extension below 20 kK (solid red line) is from BaSTI models. Two BaSTI evolutionary tracks are shown in purple, the solid part represents the core-He burning phase while the dotted part is the post-EHB phase. The dashed purple track is from a late-flasher model. The dashed-dotted red line is the ZAHeMS with the stellar masses indicated along the line. References for theoretical models are listed in Sect. 4.1.1.

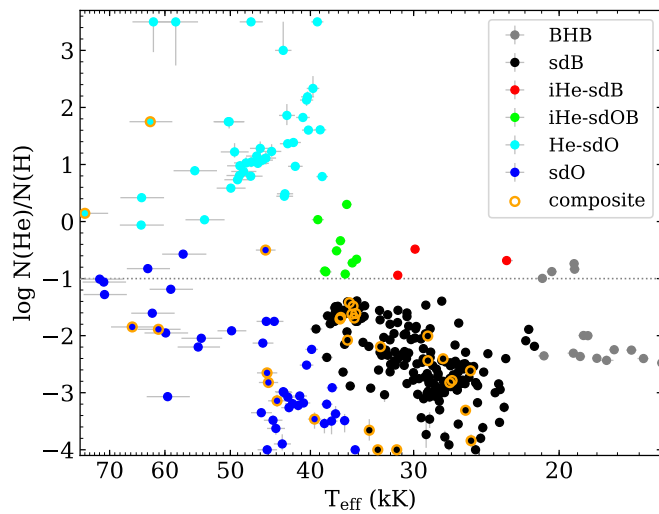


Fig. 3: Helium abundance as a function of T_{eff} for the stars in the Bok sample. The spectral groups are indicated following the same color scheme as in Fig. 2. The solar helium abundance is indicated with the dotted line.

gravity is typically the atmospheric parameter with the largest uncertainty and is also more affected by systematics (e.g., from fitting different spectra of the same star, see Dawson et al. in prep.). Because the stellar parameters R and L do not strongly depend on $\log g$, they can be relatively well constrained, provided that the *Gaia* parallax is well determined. On the other hand, because M depends linearly on the surface gravity, we are typically left with rather large uncertainties on the masses derived from the combination of spectroscopy, SED fits and parallaxes ($\sim 16\text{--}20\%$, see Sect. 5).

For some of our targets, the SED fit indicates an IR excess, attributed to the target being a binary system with a cool companion that is bright enough to emit more IR flux than the hot

subdwarf itself (see App. A). This is typically the case for main sequence companions earlier than spectral type M. In such cases, we fit the flux contribution of the companion with synthetic spectra for main sequence stars from the Göttingen spectral library (Husser et al. 2013) by including two additional parameters: the surface ratio $A_{\text{MS}}/A_{\text{sd}}$ between the MS companion and the hot subdwarf and T_{eff} of the companion. We assume the companion star to have a $\log g$ typical of MS stars ($\log g = 4$) and a metallicity of $[\text{Fe}/\text{H}] = -0.3$, which is a mean value for the F/G/K-type companions (Vos et al. 2018).

4. Results

4.1. The Bok sample

4.1.1. Atmospheric parameters

All of the Bok spectra were fit following the method described in Sect. 3.1. From the inspection of the spectral fits, five peculiar objects stood out and were removed from the sample because their spectra could not be modeled adequately. They are listed in Appendix B and their spectra are shown in Fig. B.1. In Figs. 2 and 3 we show the distribution of the hot subdwarfs from the Bok sample in the $T_{\text{eff}}-\log g$ plane (hereafter Kiel diagram) and in the $T_{\text{eff}}-\text{He}$ plane. Given the low resolution of the Bok spectra, the helium abundance in the most He-poor stars ($\log N(\text{He})/N(\text{H}) \sim -4$) should be considered as an upper limit. Figure 4 shows the Bok spectrum and best-fitting model for four stars of various T_{eff} and helium abundances. The best fit for all stars in the Bok sample are available as supplementary figures online (see Sect. 7). The atmospheric parameters obtained for all stars in the Bok sample are listed in Table D.1. This table also includes the stellar parameters obtained from the parallax and SED fits, as well as additional information on the pulsation and binary properties of each star. An extended version of Table D.1, with additional columns, is only available online at the CDS (see Sect. 7). In Table 1 we present an excerpt of Table D.1 for 15 stars.

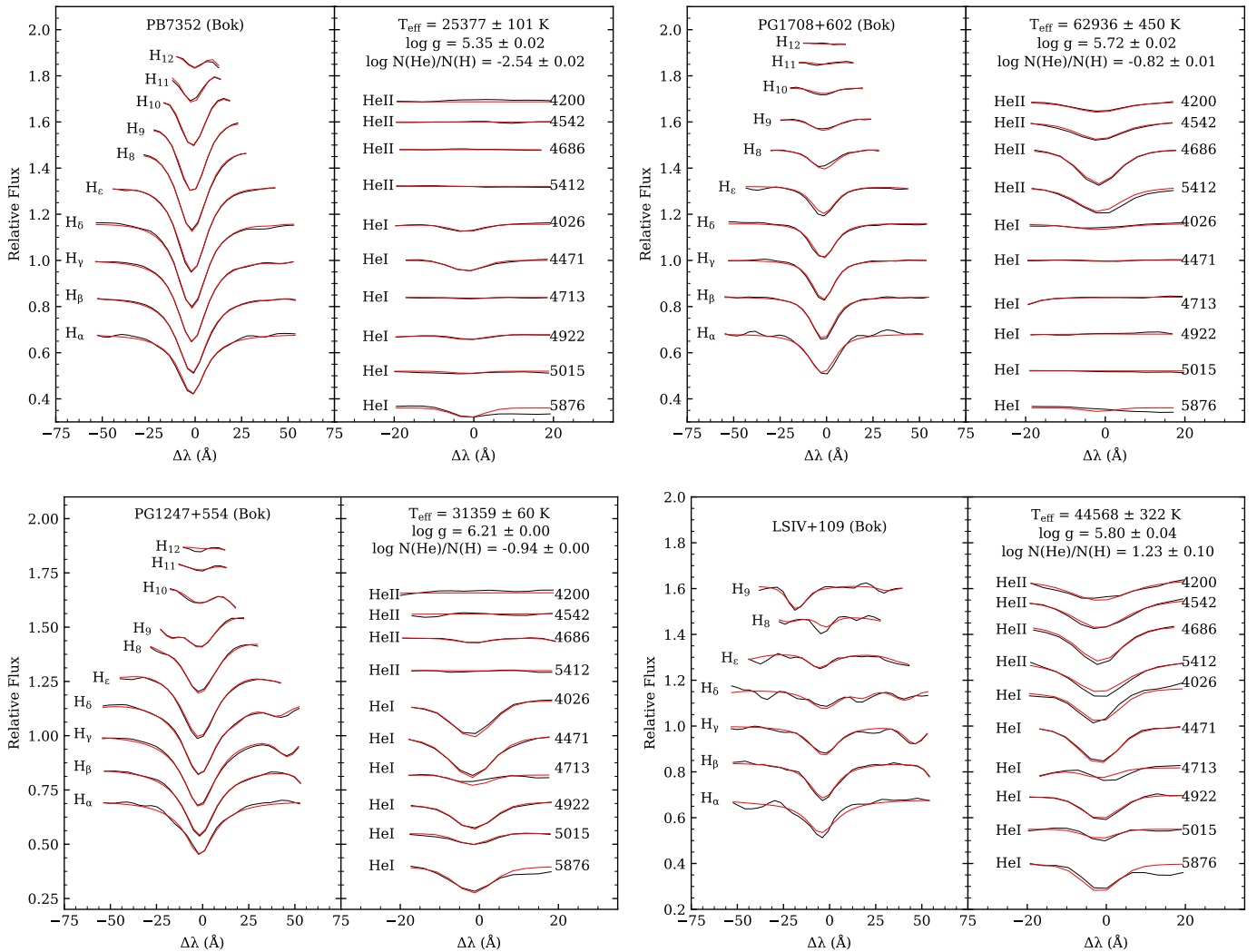


Fig. 4: Bok spectrum (black) and best fit solution (red) for four stars in our sample. PB7352 is a typical hydrogen-rich sdB and PG1708+602 is a hot sdO. PG1247+554 is an iHe-sdB located below the EHB in the Kiel diagram. LSIV+10°4 is a He-sdO where the He II Pickering series blends with the Balmer lines.

Evolutionary models. On the Kiel diagram (Fig. 2) and some other figures in this work, we include evolutionary tracks that we describe here. The zero-age and terminal-age extreme horizontal branches (respectively ZAEHB and TAEHB) shown in Figs. 2, 5, and 6 are those predicted from static stellar models computed with STELUM for a fixed core mass of $0.47 M_{\odot}$ and various hydrogen envelope thicknesses (see Baran et al. 2024 and Sect. 5.2 for a detailed description of the models). We extended the ZAEHB to the cooler HB region with a model taken from the BaSTI database (Hidalgo et al. 2018)² for solar metallicity. Two EHB evolutionary tracks from BaSTI and one late flasher model track (Miller Bertolami et al. 2008) are also included. The two BaSTI tracks show that the cooler sdBs, having a thicker hydrogen envelope, decrease in $\log g$ during their post-EHB evolution. In contrast, sdBs at the hot end of the EHB, modeled as the products of a delayed helium flash, have very little hydrogen envelope left and evolve towards hotter temperatures at almost constant $\log g$ (see also Xiong et al. 2017). Finally, we also indicate the zero age helium main sequence (HeZAMS, Paczyński 1971) that is located at the hot end of the EHB.

Spectral classification. We divided the stars into different groups based on their helium abundance and effective temperature, following the classification presented in Fig. 4.1.4 of Dorsch (2024). Besides bona fide hot subdwarf stars, our sample also includes some cooler objects that are mostly BHB stars, with ten potential main sequence (MS) B stars³ (see Sect. 4.1.2). Our classification uses the following categories (see also Fig. 3): BHB for the cooler HB objects ($T_{\text{eff}} < 21$ kK), sdB and sdO for the objects that have an hydrogen-rich atmosphere, iHe-sdB and iHe-sdB for the few intermediate-helium objects with $\log N(\text{He})/N(\text{H})$ between about -1.0 and 0.6 , and, finally, He-sdBs for the hot stars ($T_{\text{eff}} \gtrsim 38$ kK) with a helium dominated atmosphere.

The solar helium abundance has been traditionally used as a divide between helium-poor and helium-rich sdBs, however from our distribution we see that the helium abundances in none of our sdBs reach the solar value. Instead, the abundances clearly plateau at about $\log N(\text{He})/N(\text{H}) = -1.4$. This plateau of the sdB helium abundances is also conspicuous among the 500 pc sample (Dawson et al., in prep.) and consistent with the early results

² <http://basti-iac.iaa-teramo.inaf.it/>

³ These are not included in the figures.

Table 1: Excerpt from the table of results for 15 stars

Star	Type	T_{eff} (K)	$\log g$ (cm s^{-2})	$\log N(\text{He})/N(\text{H})$	R (R_{\odot})	L (L_{\odot})	M (M_{\odot})	IR-excess	<i>Gaia</i> ruwe	Pulsation	Binarity
PG0001+275	sdB	27019^{+42}_{-44}	$5.58^{+0.01}_{-0.01}$	$-2.85^{+0.03}_{-0.03}$	$0.187^{+0.005}_{-0.004}$	$16.9^{+1.1}_{-1.0}$	$0.48^{+0.08}_{-0.07}$	no	1.01	g	binary
PG0004+133	sdB	28650^{+71}_{-149}	$5.46^{+0.01}_{-0.01}$	$-1.88^{+0.02}_{-0.02}$	$0.204^{+0.004}_{-0.004}$	$25.2^{+1.5}_{-1.5}$	$0.43^{+0.07}_{-0.06}$	no	0.93	no	binary
PG0009+036	MS-B	18698^{+188}_{-221}	$4.55^{+0.03}_{-0.03}$	$-1.90^{+0.04}_{-0.03}$	$1.884^{+0.283}_{-0.283}$	$390.3^{+182.4}_{-110.5}$	$4.66^{+2.37}_{-1.43}$	no	1.01
PG0011+221	sdO	42039^{+179}_{-176}	$5.48^{+0.02}_{-0.02}$	$-3.19^{+0.05}_{-0.05}$	$0.191^{+0.007}_{-0.007}$	$103.1^{+12.1}_{-10.8}$	$0.41^{+0.08}_{-0.07}$	no	0.97	no	binary
PG0011+283	sdB	24742^{+152}_{-176}	$5.47^{+0.02}_{-0.01}$	$-3.61^{+0.08}_{-0.09}$	$0.176^{+0.004}_{-0.004}$	$10.5^{+0.8}_{-0.7}$	$0.33^{+0.06}_{-0.05}$	no	0.68	g	single
PG0014+068	sdB	35638^{+102}_{-178}	$5.93^{+0.01}_{-0.02}$	$-1.62^{+0.02}_{-0.02}$	$0.116^{+0.018}_{-0.014}$	$19.5^{+6.6}_{-4.5}$	$0.42^{+0.16}_{-0.11}$	yes	1.15	p	...
PG0032+247	sdO	38221^{+159}_{-159}	$5.63^{+0.02}_{-0.02}$	$-3.20^{+0.07}_{-0.07}$	$0.172^{+0.008}_{-0.008}$	$56.7^{+6.9}_{-6.0}$	$0.46^{+0.10}_{-0.08}$	no	0.99	...	single
PG0033+266	sdB	26706^{+108}_{-108}	$5.58^{+0.02}_{-0.02}$	$-2.45^{+0.03}_{-0.03}$	$0.182^{+0.007}_{-0.007}$	$15.2^{+1.4}_{-1.3}$	$0.46^{+0.08}_{-0.07}$	no	1.11	no	single
PG0039+135	He-sdO	47860^{+145}_{-156}	$5.97^{+0.03}_{-0.03}$	$1.03^{+0.08}_{-0.06}$	$0.195^{+0.008}_{-0.007}$	$180.6^{+30.2}_{-26.3}$	$1.31^{+0.29}_{-0.24}$	no	0.95	no	...
PG0057+155	sdB	34736^{+91}_{-91}	$5.75^{+0.01}_{-0.01}$	$-1.68^{+0.01}_{-0.01}$	$0.143^{+0.003}_{-0.003}$	$26.9^{+1.9}_{-1.7}$	$0.42^{+0.07}_{-0.06}$	no	1.03	no	single
PG0101+039	sdB	27108^{+51}_{-72}	$5.53^{+0.01}_{-0.01}$	$-2.75^{+0.03}_{-0.03}$	$0.187^{+0.004}_{-0.004}$	$17.0^{+1.0}_{-1.0}$	$0.43^{+0.06}_{-0.06}$	no	0.85	g	sd+WD
PG0105+276	He-sdO	64031^{+800}_{-710}	$5.47^{+0.04}_{-0.04}$	$0.42^{+0.03}_{-0.00}$	$0.275^{+0.046}_{-0.035}$	$1150.5^{+546.4}_{-357.0}$	$0.82^{+0.36}_{-0.23}$	no	0.94
PG0108+195	sdO	45672^{+284}_{-326}	$6.11^{+0.03}_{-0.03}$	$-2.13^{+0.05}_{-0.05}$	$0.122^{+0.006}_{-0.005}$	$58.0^{+9.4}_{-8.1}$	$0.69^{+0.16}_{-0.13}$	no	0.93	no	single
PG0123+159	sdB	29215^{+104}_{-133}	$5.62^{+0.02}_{-0.02}$	$-2.41^{+0.03}_{-0.04}$	$0.185^{+0.008}_{-0.007}$	$22.4^{+2.2}_{-1.9}$	$0.52^{+0.10}_{-0.08}$	no	1.09	no	single
PG0133+114	sdB	29112^{+104}_{-145}	$5.68^{+0.02}_{-0.02}$	$-2.43^{+0.02}_{-0.02}$	$0.155^{+0.005}_{-0.005}$	$15.5^{+1.3}_{-1.2}$	$0.42^{+0.07}_{-0.06}$	no	0.83	no	sd+WD

Notes. Uncertainties on the atmospheric parameters (T_{eff} , $\log g$, and, $\log N(\text{He})/N(\text{H})$) are only statistical.

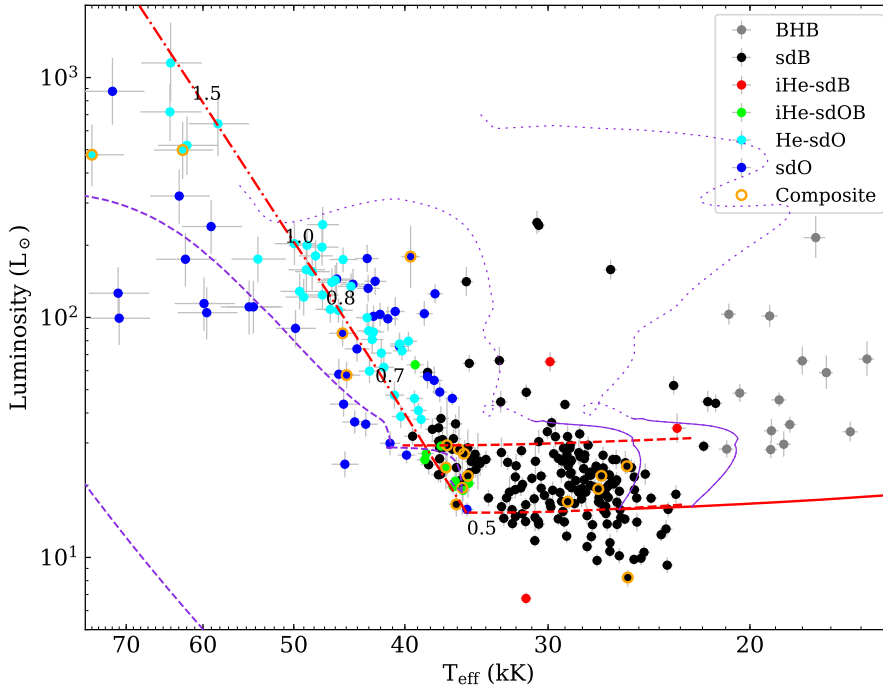


Fig. 5. Luminosity of our stars versus their T_{eff} (i.e., HRD). The different spectral types are color-coded as in the previous figures. We indicate the composite objects with an additional orange circle around the symbols. The evolutionary tracks are the same as in the Kiel diagram (Fig. 2). The four luminous post-AGB stars mentioned in Sect. 4.1.1 are outside the luminosity range shown here.

of Edelmann et al. (2003). Thus, we believe that the separation between the H-rich sdBs and the intermediate-helium subdwarfs should be made at a value of $\log N(\text{He})/N(\text{H}) = -1.2$, rather than -1.0 .

We note that our classification is intended to examine and compare mass distributions by class. Thus the separation between the sdBs and sdOs mainly aims at separating the typical hydrogen-rich subdwarfs on the EHB (sdBs) from their hotter evolved post-EHB counterparts (sdOs) and is not strictly based on effective temperature or strength of the He II lines. The transition from sdB to sdO is gradual, and both classes are connected from an evolutionary perspective (Heber 2009). The separation between the cool sdBs and the BHB is also ambiguous. The position of the Momany jump separating the BHB stars from the EHB is known to be around 18–20 kK (Newell & Graham 1976; Momany et al. 2002; Brown et al. 2016). When looking at

our stars in Figs. 2 and 3 we see instead a discontinuity around 23 kK, with the cooler stars being found at lower $\log g$, close to the TAEHB in Fig. 2, and clustering at a helium abundance close to $\log N(\text{He})/N(\text{H}) = -2$ (Fig. 3). Whether the few stars between 20 and 23 kK are sdBs or BHBs remains uncertain.

Peculiar objects. Our sample contains four luminous hot stars (50–60 kK) with $\log g \leq 4.5$ (indicated in Fig. 2). These are the two very similar extreme-He stars BD+37°1977 and BD+37°442, which likely have surface gravities slightly below the limit of our model grid at 50 kK (i.e., $\log g < 4.25$, see Jeffery 2020 and references therein), the He-sdO KPD2322+4933 ($\log N(\text{He})/N(\text{H}) = 0.9$), and the sdO BD-3°2179 ($\log N(\text{He})/N(\text{H}) = -0.6$). These luminous objects are likely associated with the post-AGB phase. Another in-

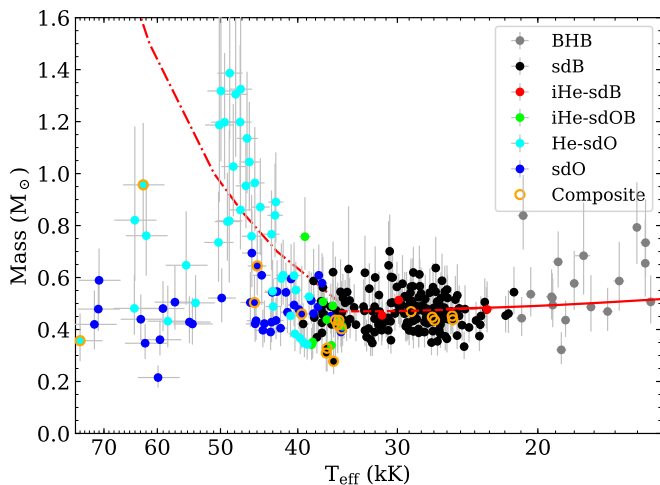


Fig. 6: Mass as a function of T_{eff} for the stars in the Bok sample. The spectral types are indicated following the same color scheme as in Fig. 5. The masses expected from the STELUM and BaSTI models for the ZAEHB are indicated by dashed and solid red lines respectively. Masses expected from the ZAHeMS are indicated with the dashed-dotted line.

teresting object is the He-sdO GSC03214-02615 ($T_{\text{eff}}=43$ kK, $\log g=5.7$, $\log N(\text{He})/N(\text{H})=0.44$) that is a candidate magnetic sdO. Its spectrum, displayed in Fig. B.1, shows the strong absorption feature around 4620 Å, which is still of unidentified origin. This feature is present in other stars with similar atmospheric parameters, whether they show the Zeeman splitting indicative of magnetic field or not (Dorsch et al. 2024).

4.1.2. Stellar parameters

Having determined the atmospheric parameters of our stars, we proceed with the fit of the SEDs as described in Sect. 3.2. The main goal of the SED fits is to derive reliable stellar parameters for the stars in our sample. This requires the *Gaia* parallax to be well measured. Thus, in the figures and the analyses involving R , L , and M , we always exclude stars with a parallax error larger than 20% and those with $\text{ruwe}^4 > 1.4$ (El-Badry et al. 2021). We also inspected the SED fit result for each star and removed stars that could not be properly reproduced. For example, the SED of PB5450 (also known as EQ Psc) is strongly affected by the irradiation of its companion (see Baran et al. 2019). We show in Fig. 5 the distribution of the 300 remaining stars in terms of luminosity versus T_{eff} (the HRD). From the masses derived with the parallaxes and SED fits, we identified ten stars among the BHB sample that have masses above $3 M_{\odot}$, indicating that they are more likely to be MS objects although the less massive ones might be intermediate-mass stripped stars (Irrgang et al. 2022; Villaseñor et al. 2023). From the SED fits, we identified 29 stars with an IR excess consistent with MS companions of T_{eff} between 3000 and 5900 K (see Fig. A.1), which are marked with an additional orange circle⁵ in Figs. 2 to 6. The properties of these systems are listed in Table A.1 and several are discussed in Appendix A. The composite systems include a few known

⁴ the re-normalized unit-weight error is a measure of the astrometric goodness of fit.

⁵ We note that many of the stars with an IR-excess have $\text{ruwe} > 1.4$ and thus do not appear in the Figs. 5 and 6. However they are all listed in Table A.1.

short and long period binaries (e.g. Maxted et al. 2000; Saffer et al. 1998; Vos et al. 2019). We note that the spectra of these composite systems were fitted in the same way as all stars, only with a model atmosphere for the hot subdwarf component. For most of them, we do not see contamination from the companion in the Bok spectrum. This is the case for PG0014+068, among others (see Appendix E). Only in stars with more luminous G-type companions, such as PG1701+359 we do see spectral features from the companion, like the Mg triplet lines (~ 5170 Å). The wavelength regions contaminated by features from the companion are ignored during the spectral fit. Nevertheless, the atmospheric parameters obtained for the stars with the strongest IR-excess might be less accurate than for the other stars.

On the HRD, most of the sdBs are found on the theoretical HB, but a noticeable fraction are located below the ZAEHB. These “underluminous” stars are further discussed in Sect. 5.3. The luminous sdBs and the sdOs are consistent with a post-EHB phase as suggested by the evolutionary tracks. Interestingly, the hydrogen-rich sdOs are mainly divided into two groups, found on each side of the ZAHeMS. The group on the hot side of the ZAHeMS (the hottest sdOs) is consistent with the evolutionary track starting at the hot end of the EHB, meaning they probably evolved from the hottest sdBs (those with the smallest hydrogen envelope, often called sdOBs), while the cooler post-EHB stars may be the progeny of cooler sdBs. This division of the sdOs into two regions is also visible in the Kiel diagram (Fig. 2). Another noteworthy feature visible in both the HR and Kiel diagrams is a gap in the T_{eff} distribution of sdB stars around 33–34 kK, corresponding to a luminosity of about $20 L_{\odot}$. Such a drop in the density of sdBs along the EHB was also reported in Geier et al. (2022) who noticed a void of stars around 33 kK and $\log g = 5.7$ in the Kiel diagram of their hot subdwarfs sample. This separation of the sdBs into two regions, with one populating the very hot end of the EHB is reminiscent of the dichotomy found by Xiong et al. (2017) in their evolutionary models. In their models, the hotter sdBs are those with almost no H-rich envelope left because they experienced flash-mixing in their atmosphere due to a delayed He-flash. This is essentially the late-flasher scenario, first presented in D’Cruz et al. (1996) to explain the population of blue hook stars in some massive globular clusters. As for the cooler sdBs, they follow the canonical formation scenario where the He-flash happens at the tip of the RGB. We note that the presence of a gap between the canonical EHB stars and the hotter He-enriched blue-hook stars is also observed in ω Cen and NGC 2808 (Brown et al. 2016) and happens around 32–33 kK (Latour et al. 2018). Finally, the position of the majority of He-sdOs is remarkably consistent with that of the helium main sequence of Paczyński (1971). Following the theoretical masses along this sequence, our He-sdOs would have masses that increase with T_{eff} , mainly from 0.6 to $1.0 M_{\odot}$.

Figure 6 shows that our masses do not have a trend with T_{eff} ⁶, with the exception of the He-sdOs. This is the expected behavior because the effective temperatures of EHB stars are determined by the extent of their hydrogen envelopes, which are always negligible in mass ($\lesssim 0.02 M_{\odot}$) compared to the core. Even for the BHB stars, the increase in mass is very small as shown by the BaSTI track.

For the He-sdOs, we observe the expected mass increase for stars between 40 and 50 kK. However, compared to the masses inferred from their positions near the ZAHeMS on the HRD, the masses obtained from the SEDs appear underestimated at the cool end and overestimated at the hot end. This discrepancy

⁶ This could not be achieved for the MMT sample, see Sect. 4.2.1.

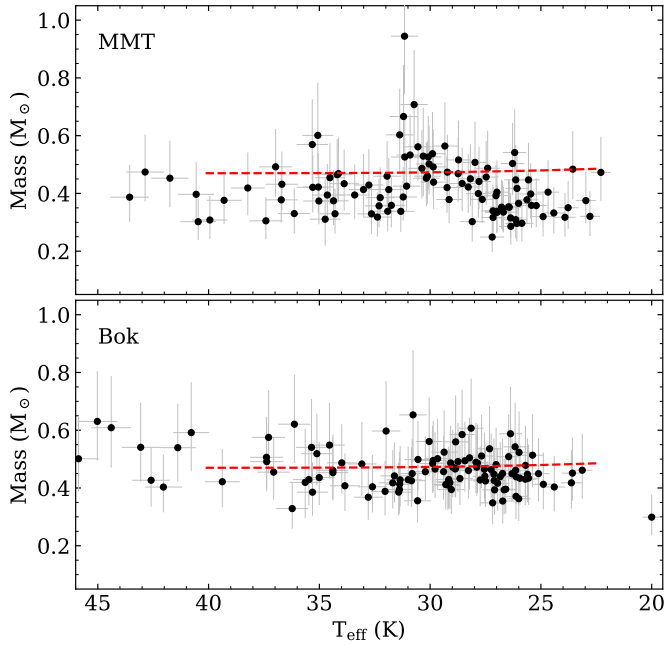


Fig. 7: Mass versus T_{eff} for the stars in the MMT sample. The masses obtained when using the atmospheric parameters from the MMT spectra (top) and the Bok spectra (bottom). The dashed line shows the canonical, $0.47 M_{\odot}$, expected for EHB stars.

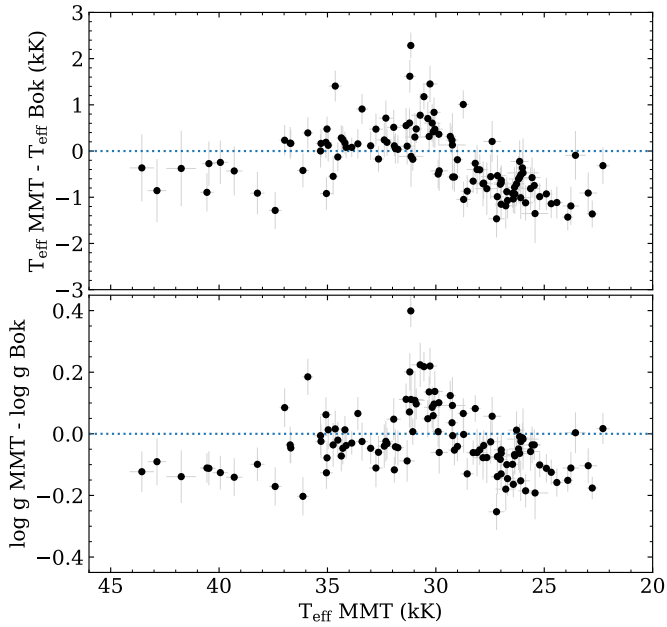


Fig. 8: Comparison between the atmospheric parameters, T_{eff} and $\log g$, obtained from the MMT and Bok spectra.

likely arises from a T_{eff} -dependent bias in our $\log g$ measurements. Indeed, in the Kiel diagram, the cool He-sdOs are found above the ZAHeMS while the hot He-sdOs are slightly below it (Fig. 2), which is somewhat inconsistent with their more precise location on the HRD. The spectra of the He-sdOs remain challenging to model, and it is possible that their atmospheric parameters, especially $\log g$, still suffer from some systematics.

4.2. The MMT Sample

4.2.1. Atmospheric and stellar parameters

The MMT spectra were fit in the same way as described earlier, and from their atmospheric parameters we also derived the stellar parameters via the SED fitting method. Although these spectra have a higher resolution than the Bok spectra, they cover a smaller wavelength range (4000–4950 Å) that includes only three Balmer lines (H_{β} , H_{γ} , and H_{δ}). All stars in the MMT sample are shown in the MMT spectral atlas included in Fig. D.1. When inspecting the resulting masses, we noticed an obvious mass trend as seen in the top panel of Fig. 7. There is a significant increase in masses for the stars around 30 kK. The MMT sample consists of hydrogen-rich sdBs and sdOs only, thus no visible mass dependency over T_{eff} is expected, as seen for the masses derived with the atmospheric parameters obtained from the Bok spectra of these same stars (Fig. 7, bottom panel).

We then inspected the differences in atmospheric parameters obtained from the MMT and the Bok spectra for the 116 stars present in both samples. From the results shown in Fig. 8, we observe a trend in T_{eff} and $\log g$ for stars between 25 and 30 kK. Generally speaking, the MMT spectra of the “cool” sdBs are fit with lower T_{eff} and lower $\log g$ compared to the Bok spectra. The opposite happens for the sdBs hotter than ~ 35 kK; their MMT spectra result in higher T_{eff} and higher $\log g$ than their Bok spectra. We thus conclude that the restricted wavelength range of the MMT spectra does not allow us to derive atmospheric parameters that are accurate enough to obtain reliable masses from the SED fits, even if the spectra are of excellent quality. This highlights the importance of the high Balmer lines in the determination of the atmospheric parameters, especially that of the surface gravity (Hubeny et al. 1994). Nevertheless, there are things to be learned from the MMT spectra. We discuss the presence of helium stratification in the following subsection and the particular case of PG0215+183 is presented in App. C.

4.2.2. Helium stratification

While examining the best-fit solutions of the MMT spectra, we noticed that the helium lines in a few stars were poorly reproduced (see Fig. 9 for two examples). One of these stars is BD+48°2721, which is a cool sdB, or possibly a BHB, known to show the ${}^3\text{He}$ anomaly (Edelmann et al. 2001). The ${}^3\text{He}$ anomaly implies that neutral He absorption lines feature contributions from both the ${}^3\text{He}$ and ${}^4\text{He}$ isotopes. In addition, Schneider et al. (2018) found that the strongest He I lines in BD+48°2721 could not be properly reproduced by the model spectra: the line cores are shallower in the observations. This phenomenon is attributed to a vertical stratification of He in the stellar atmosphere. In fact, the vertical stratification and the presence of ${}^3\text{He}$ are both a manifestation of atomic diffusion taking place in the atmosphere. Besides this object, Schneider et al. (2018) also detected He stratification in three ${}^3\text{He}$ sdB stars with T_{eff} between 26.5 and 29 kK.

The mismatch between the observed and modeled He lines in the spectrum of BD+48°2721 is caused by He stratification. Similar mismatches are seen in BD+42°3250, PG0004+133 (see Fig. 9), PG1738+505, PG0242+132, and possibly PG1512+244 and PG1519+640, indicating that they also have He stratification. Figure 10 shows the position of these stars in the T_{eff} -helium plane. The T_{eff} of these six objects are between 28 and 31 kK, which is consistent with the T_{eff} range of the known ${}^3\text{He}$ and stratified stars (Schneider et al. 2018; Geier et al. 2013).

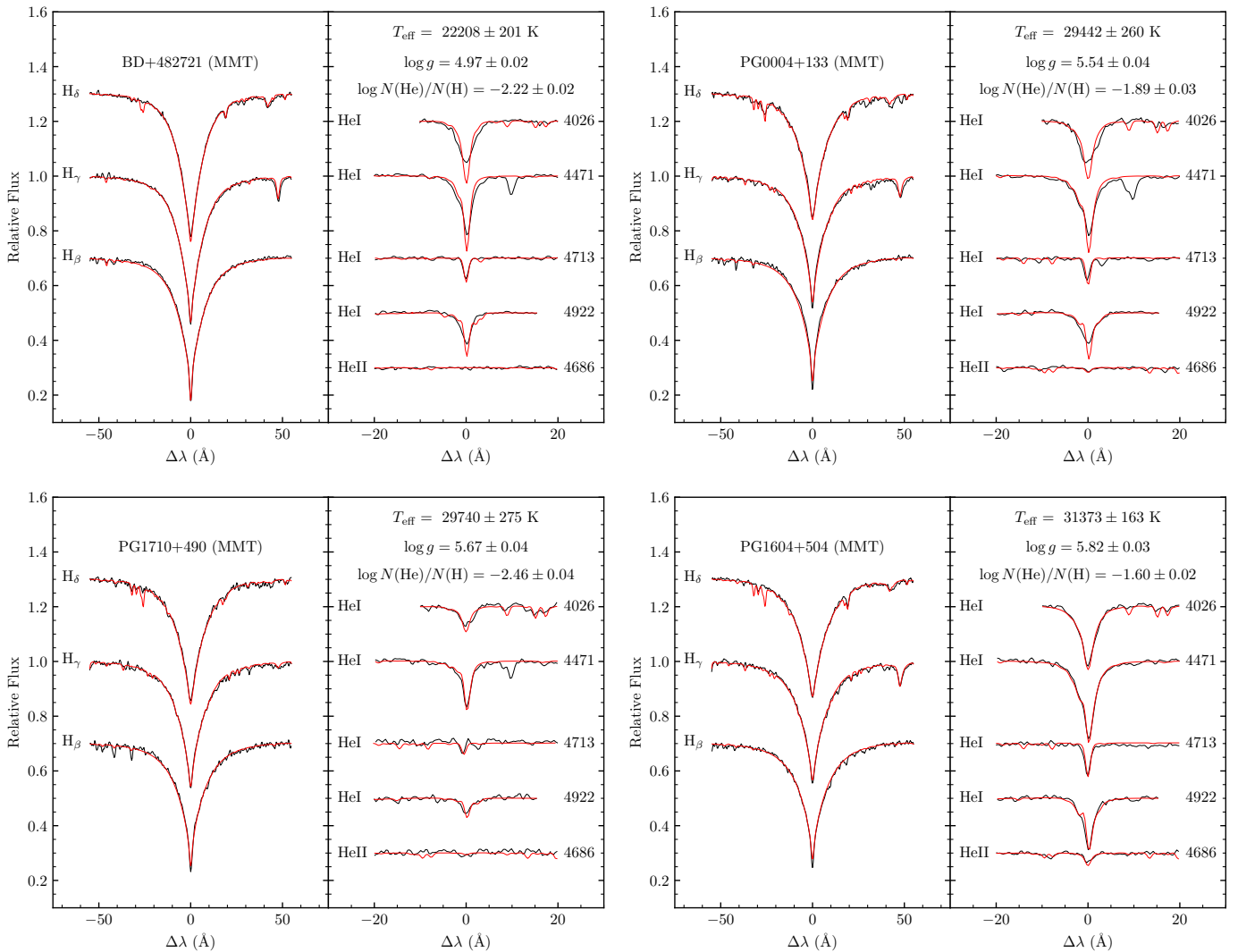


Fig. 9: Upper panel: Best fit of the Balmer and helium lines in selected stars from the MMT sample. Top: BD+48°2721, a known ^3He star, and PG0004+133. The mismatch between the predicted and observed He lines is due to the stratification of helium in the atmosphere. Bottom: PG1710+490, a known ^3He star with no indication of stratification (also according to Schneider et al. 2018) and PG1604+504, that shows no indication of stratification.

It is likely that the six new He-stratified objects are also enriched in ^3He , but the isotopic shift of the He lines in the MMT spectral range is too small (0.2–0.3 Å) to be detectable at a resolution of 1 Å. Up until now, He stratification has only been reported in ^3He stars. However, not all ^3He stars show evidence of stratification. Our sample also includes two known ^3He stars that do not show evidence of He stratification: PG0133+114, and PG1710+490 (see Fig. 9). The latter was included in the analysis of Schneider et al. (2018) while the former was only reported by Edelmann et al. (2001). In light of these results, it appears that the stratification of helium, and possibly of other elements (Geier 2013), and also the presence of ^3He , is more common than previously thought in sdBs with T_{eff} around 28–31 kK.

5. Discussion

5.1. Mass distributions

Using the masses presented in Sect. 4.1.2, we now examine the mass distribution of our hot subdwarfs. For this discussion, we

always exclude the stars that were fitted with an IR excess, unless stated otherwise. We first concentrate on the three most populated spectral types: sdB, sdO and He-sdO. We show in Fig. 11 the mass distributions for these three spectral types. Along with the mass distributions, we also calculated the average mass (\bar{M}) as a weighted mean for each spectral type. Because the uncertainties (ϵ) are proportional to the mass itself, we used the relative uncertainty as weight, leading to:

$$\bar{M} = \frac{\sum w_i M_i}{\sum w_i}, \text{ where } w_i = \frac{M_i^2}{\epsilon_i^2}.$$

We also computed the median mass (\tilde{M}) of the distributions. Both of these values are reported in Fig. 11 and in Table 2. In the table, we include three additional diagnostics: the median value of the uncertainties (M_{err}), the standard deviation (σ) of the mass distribution, and its 68% interquartile range ($Q_{16}-Q_{84}$). Both M_{err} and σ are expressed as a percentage to remove the correlation between the masses and their absolute uncertainties.

As shown in Fig. 11, the sdB and sdO distributions are very similar and peak around $0.47 M_{\odot}$. This agrees with theoretical

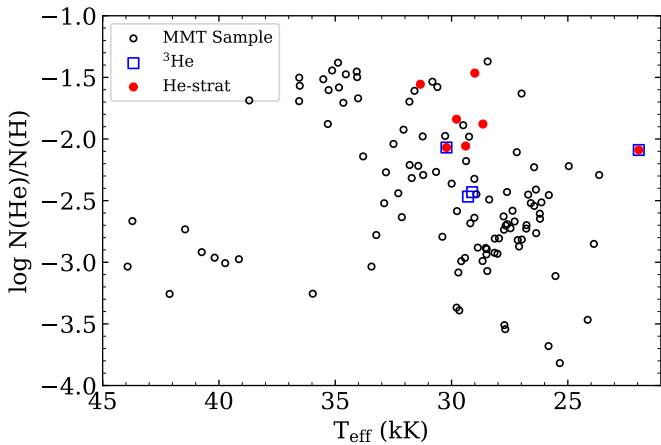


Fig. 10: Position of the stars from the MMT sample in the T_{eff} –He plane. Stars showing indication of He-stratification in their MMT spectrum are indicated with filled red circles. Stars having ${}^3\text{He}$ in their atmosphere are indicated with blue squares (from Schneider et al. 2018 and Geier et al. 2013).

expectations, since the two types are thought to be evolutionarily linked and have comparable average masses close to this (canonical) value. Our mean and median values for the sdBs are also consistent with the 0.47 M_\odot obtained by Fontaine et al. (2012) from 22 sdBs with masses derived from asteroseismology and the light curve analysis of binary systems. Our distribution is wider than that of Fontaine et al. (2012), but masses obtained from asteroseismology and light curve modeling typically have smaller uncertainties than those derived from SED fits and parallaxes. The typical uncertainty on the individual masses (M_{err}) and the standard deviation (σ) of the sdO distribution are similar, while for the sdBs we found σ to be smaller than the typical error. This means that the broadening of our sdB and sdO distributions can be fully explained by the uncertainties. The consistency between our sdB and sdO mass distribution is a significant improvement compared to the results of Lei et al. (2023), who obtained a relatively flat mass distribution for their sdO stars. Their unrealistic sdO masses are most likely caused by the lack of metallic opacities in the model atmospheres they used to derive the atmospheric parameters and compute the SEDs of their hot sdOs. It is especially important to take into account both NLTE effects and line-blanketing when modeling the spectra of hot sdO stars (Werner 1996; Latour et al. 2013, 2015).

Intriguingly, the mass distribution of the He-sdOs is very different from that of the H-rich hot subdwarfs: it is much broader, with 68% of the stellar masses falling between 0.48 and 1.18 M_\odot , and it does not show a distinct peak. The dispersion is significantly larger than the typical uncertainties, suggesting the presence of an intrinsic dispersion. The weighted mean and median mass of the He-sdOs are around 0.77 M_\odot , which is significantly larger than the canonical core-helium burning mass. However, caution is advised when assessing the masses derived for the He-sdOs. As mentioned in Sect. 4.1.2, the masses obtained from SED fits and parallaxes of the He-sdOs are somewhat different from those expected from the position of the stars in the HRD. We also calculated masses for the He-sdOs from their position on the HRD, meaning that we projected each star onto the nearest point along the ZAHeMS. Uncertainties in T_{eff} and L were taken into account to estimate the corresponding uncertainties on the masses, which are notably lower than those obtained from

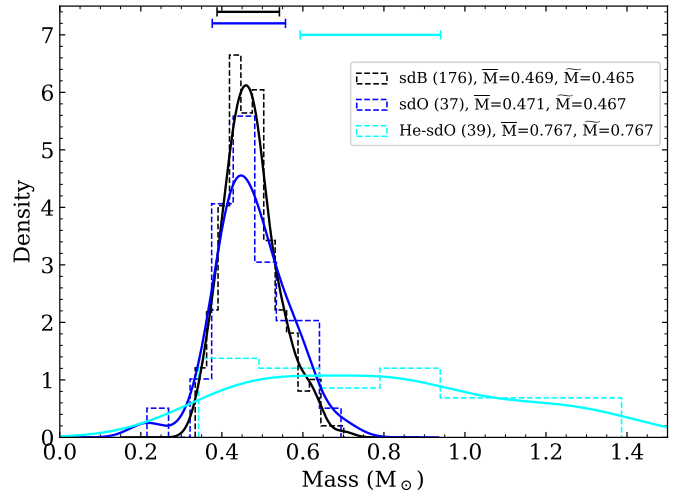


Fig. 11: Mass distribution obtained from parallaxes and SED fits for the sdBs, sdOs, and He-sdOs in our sample. The dashed lines show the normalized histograms for each spectral group and the solid curves are the associated kernel density function. The stars with a composite SED were excluded. In the legend, we indicated the number of stars in parenthesis as well as the average (\bar{M}) and median (\tilde{M}) mass for each spectral type. The error bars on top are indicative of the mass uncertainty for each spectral type (see M_{err} in Table 2).

the SED fits. The HRD masses are included in Table 1 and we also include their statistics in Table 2. Masses from the HRD were not computed for the 3 He-sdOs that are post-AGB objects (see Sect. 4.1.1). The He-sdO masses obtained from the HRD are mostly distributed between 0.6 and 1 M_\odot without any distinct peak. The four He-sdOs hotter than 58 kK have masses around 1.4 M_\odot . Analyses of He-sdO samples including mass estimates are still scarce in the literature, but the mass distribution of He-sdOs shown in Dorsch (2024, Fig. 4.1.7) also has an extended high-mass tail with values above 1 M_\odot . On the other hand, the position of He-sdOs from the SALT spectroscopic survey (Jeffery et al. 2021) in the HRD shown in Dorsch et al. (2024) suggests that they have masses between 0.6 and 1.0 M_\odot according to the helium main sequence of Paczyński (1971). This is very similar to what is seen in our sample, although this might not be surprising given that the model atmospheres and analysis method used in Dorsch et al. (2024) are the same as in this work. Given the systematic uncertainties on the $\log g$ values of the He-sdOs, it is likely that the masses derived from the HRD positions are more accurate. In any case, both the masses obtained from the SED fits and the position of He-sdO stars in the HRD indicate that they are, on average, more massive and span a wider mass range than the hydrogen-rich sdBs and sdOs. The higher masses of the He-sdOs and their broader distribution are fully consistent with a stellar merger origin (see, e.g. Han et al. 2003; Justham et al. 2011; Saio & Jeffery 2000; Zhang & Jeffery 2012). This hypothesis, although long suspected, was recently further supported by the discovery of several magnetic He-sdOs (Dorsch et al. 2024, 2022; Pelisoli et al. 2022) and the low fraction of short-period binaries among He-sdOs (Geier et al. 2022; Snowden et al. 2025).

As for the BHB stars, they are expected to be slightly more massive than canonical H-rich subdwarfs, with masses between 0.50 and 0.55 M_\odot , depending on the metallicity. From our observations, we derive a median mass of about 0.54 M_\odot , which is

Table 2: Mass properties by spectral group and binary type in our sample.

Type	N_{star}	\bar{M} [M_{\odot}] (1)	\tilde{M} [M_{\odot}] (2)	M_{err} [%] (3)	σ [%] (4)	$Q_{16\text{-}84}$ [M_{\odot}] (5)
Spectral groups						
sdB	176	0.469	0.465	16.2	14.4	0.408-0.542
sdO	37	0.471	0.467	19.3	18.8	0.403-0.554
He-sdO (SED)	39	0.767	0.767	20.4	39.4	0.482-1.183
He-sdO (HRD)	36	0.753	0.845	4.2	24.9	0.696-0.964
iHe-sdOB	9	0.449	0.432	18.2	28.4	0.344-0.502
BHB	19	0.565	0.536	19.0	23.7	0.466-0.690
Binary types						
sd+WD	38	0.452	0.442	16.2	12.8	0.399-0.522
sd+dM	15	0.499	0.504	15.9	14.9	0.411-0.573
single	133	0.468	0.470	17.1	15.8	0.413-0.524
binary	92	0.469	0.460	16.2	15.7	0.400-0.551

Notes. (1) Weighted average. (2) Median. (3) Median of the individual mass uncertainties. (4) Standard deviation. (5) Interquartile range, 16th-84th percentile

in good agreement with the expectation. Finally considering the iHe-sdOBs and iHe-sdBs, our samples are too small, with nine and three stars respectively, to derive a statistically significant mass distribution. Saying that, the average mass of these stars appears to be consistent with the canonical hot subdwarf mass of around $0.5 M_{\odot}$. While the three iHe-sdBs are rather scattered on the Kiel and HR diagrams, their masses are all fairly close to the canonical values (see Fig. 6). The iHe-sdB that is significantly below the ZAEHB in both the Kiel and HR diagrams is PG1247+554 (also known as GD 319), whose best-fit is shown in Fig. 4. This is a particular system comprising an iHe-sdB in a 0.6 day period binary and cool MS star located about $1''$ away (Maxted et al. 2000; Mason et al. 2001), however the MS star is most likely a background star (S. Geier, priv. comm. 2025). The hot subdwarf and the MS star are resolved by *Gaia* and our SED fit is solely based on the *Gaia* XP spectra of the hot subdwarf. Although this star was a promising low-mass hot subdwarf candidate from its location on the HRD, the normal mass that we obtained from the SED fit does not match this interpretation.

5.2. Mass distribution and binarity

To investigate a possible dependence of mass on binarity in the stars of our Bok sample, we divided them into binary groups based on information available from the literature. Notably, Schaffenroth et al. (2022) classified many hot subdwarf binaries, mostly sdBs but also a few sdOs with $T_{\text{eff}} \sim 40$ kK, into two different categories based on their TESS light-curve properties: sdB/O+dM (HW Vir systems and reflection effects) and sdB/O+WD (ellipsoidal and beaming effects). For some of these systems, the authors estimated masses from parallaxes and SED fits and found that the mass distribution of hot subdwarfs in sdB/O+WD systems peaks at a lower mass than those having a M-dwarf (dM) companion.

To investigate this topic further, we cross-matched the stars in our sample with the stars listed in Table A.3 and A.4 of Schaffenroth et al. (2022) and extracted binary information for a few additional targets of ours from other sources: PG0101+039 (Maxted et al. 2002; Geier et al. 2008),

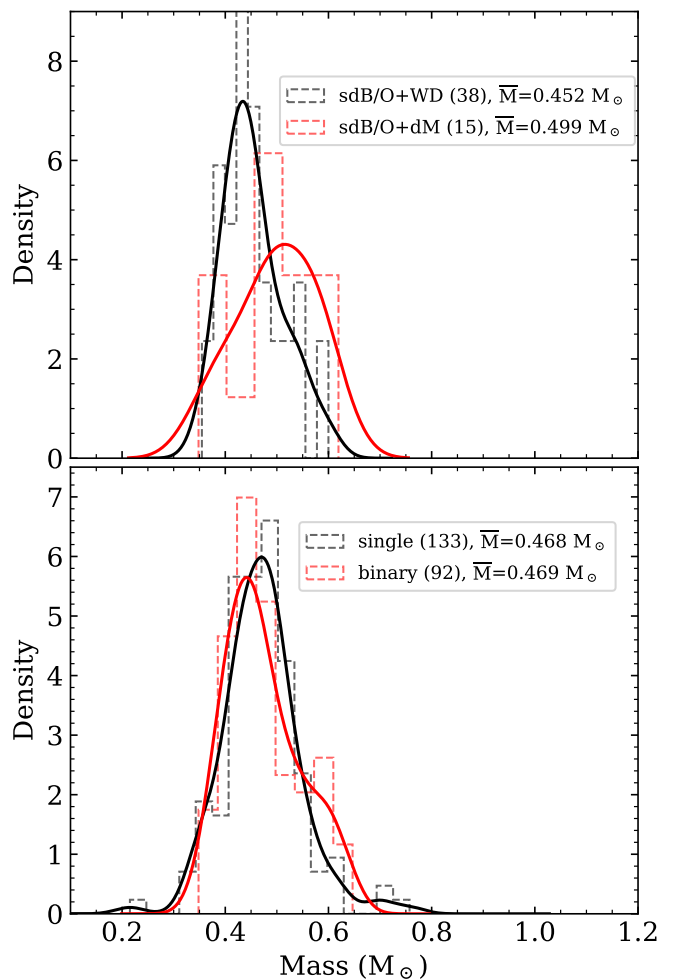


Fig. 12: Top: mass distributions of the hot subdwarf components in close binary systems with WD and dM companions. For most of the systems, the type of binarity was classified by Schaffenroth et al. (2022). The weighted average mass of both categories is also indicated. Bottom: mass distribution for hot subdwarfs that are candidate single stars compared to those found in close binary systems.

PG2345+318 (Green et al. 2004), KIC007668647 (Telting et al. 2014), and KIC011558725 (Telting et al. 2012) as sdB+WD systems and PG1438-029 (Green et al. 2004), HS2231+2441 (Østensen et al. 2008), FBS1531+381 (For et al. 2010), and UV01758+36 (Schaffenroth priv. comm. 2025) as sdB+dM systems. This yielded a subsample of 38 sdB/O+WD and 15 sdB/O+dM systems⁷. We show the resulting mass distributions in the top panel of Fig. 12. Interestingly, there is a distinct difference between the mean mass and the mass distribution of the two types of binaries (see also Table 2). The sdB/O+WD systems have an average mass close to $0.45 M_{\odot}$, while the sdB/O+dM have a slightly larger average mass of $0.5 M_{\odot}$. This is in line with the finding of Schaffenroth et al. (2022) that the hot subdwarfs with dM companions appear to be, on average, slightly more massive than those with WD companions. To verify whether the difference is significant, we ran 1000 iterations of the Kolmogorov-Smirnov test (KS-test) using masses drawn from a normal distribution based on the individual errors and we

⁷ Those are 15 systems that do not show IR-excess in their SED.

obtained an average p -value (p_{KS}) of 0.30. This means that if the two underlying distributions were the same, we would get the observed difference at least 30% of the time. Thus we cannot conclude that the difference between the two mass distributions are significant. In this case, we are likely limited by the small number of sdB/O+dM, only 15, identified in our sample. It is also worth noting that in sdB/O+dM systems, the atmospheric parameters of the hot subdwarf vary with the phase when the reflection effect is sufficiently strong, adding additional uncertainties on the atmospheric parameters derived from a single spectrum (see, e.g. Heber et al. 2004; For et al. 2010).

We also looked at the mass distribution of non-composite binaries, essentially meaning close binaries with companions that are detected only from radial velocity or light-curve variations (without producing IR-excess), to compare it with that of the apparently single stars. For this comparison, we only considered the He-poor and intermediate-He hot subdwarfs, thus excluding the He-sdOs and BHBs. To build our list of close binary stars, we started with the 53 systems identified previously (the sdB/O+WD and sdB/O+dM), to which we added known binaries from radial velocity surveys in the literature (e.g. Saffer et al. 1998; Maxted et al. 2001; Copperwheat et al. 2011; Morales-Rueda et al. 2003; Geier et al. 2022; He et al. 2025) and suspected binaries from the RV measurements of the MMT spectra and from on-going RV monitoring (F. Mattig, priv. comm. 2025). This way, we increased our number of binary stars to 92 objects. The 133 remaining stars, for which we have no evidence of binarity, or no information about their RVs, are considered as single star candidates. The resulting mass distributions for binaries and single hot subdwarfs are shown in the bottom panel of Fig. 12 and their characteristics are listed in Table 2. Both distributions appear very similar and our series of KS-tests did not find a statistically significant difference between the two distributions ($p_{KS} = 0.57$); however, this does not necessarily imply that the underlying distributions are identical.

The formation of single hot subdwarfs remains challenging to explain from a theoretical point of view. One potential formation channel is via the merger of two low-mass stars (e.g. two He-core WDs, CO-core and He-core WDs, or low-mass MS + He-core WD; Han et al. 2003; Politano et al. 2008; Hall & Jeffery 2016). According to Han et al. (2003, see their Fig. 12), the predicted mass distribution for sdBs originating from the merger channel is broader and shifted to higher masses ($0.5\text{--}0.55 M_{\odot}$) compared to those formed via common-envelope ejection. If a majority of our candidate single He-poor sdB/Os were merger products, we would expect their mass distribution to be different to that of He-poor sdB/Os in close binary systems, formed via the common envelope channel. However, given the similarity of the two mass distributions, we find no evidence that a substantial fraction of the He-poor single star candidates are formed via the merger channel.

The close binary fraction of our hot subdwarf sample is 41%⁸ (92/225). Close binary fractions from the literature ranges from 30% (Geier et al. 2022; He et al. 2025) to 48% (Maxted et al. 2001; Copperwheat et al. 2011), with the SPY sample giving an intermediate value of 39% for sdBs (Napiwotzki et al. 2004). The number of close binaries identified in our sample thus seems reasonable and although there is certainly some binaries remain-

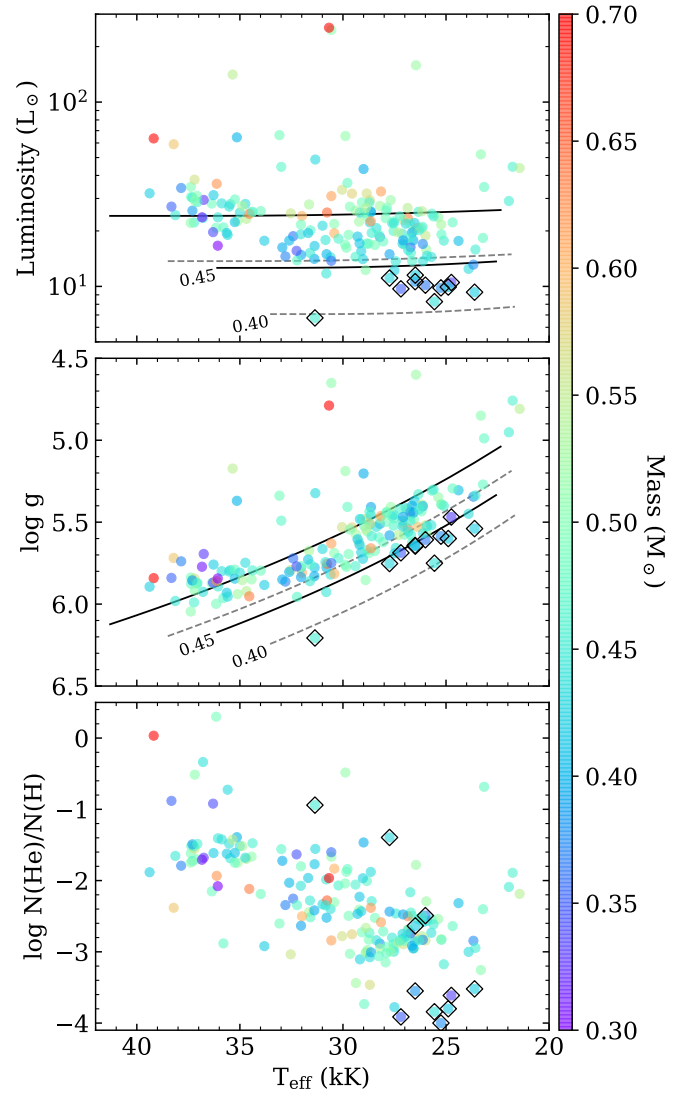


Fig. 13: Position of the underluminous sdBs (black diamonds) in the HRD (top), Kiel diagram (middle), and $T_{\text{eff}} - \log N(\text{He})/N(\text{H})$ plane. The underluminous sdBs were selected from their position below the ZAEHB for a core mass of $0.45 M_{\odot}$. The ZAEHB and TAEHB computed with STELUM for core masses of $0.45 M_{\odot}$ (solid lines) and $0.40 M_{\odot}$ (dashed lines) are indicated. All stars are color-coded with the mass obtained from the SED fits. We only show the stars with spectral types that can be associated with the EHB region: sdB, iHe-sdB, and iHe-sdOB.

ing in our single star sample, for example due to low inclination, or because the companion could be too faint or distant to be detectable. However, they are unlikely to be numerous enough to change our conclusion concerning their mass distributions. It is also worth mentioning that there are hints that the iHe-sdBs and iHe-sdOBs have different binary properties than the rest of the hydrogen-rich hot subdwarfs (see the discussions in Geier et al. 2022 and Dorsch 2024), but we decided to keep them in our hydrogen-rich sample as they are only 12 stars and they represent less than 5% of our sample.

⁸ This is when excluding the composite systems, some of which also are close-binary systems, such as PG0940+068 and PG1101+249 (see App. A). When including all 27 composite systems (the two He-sdOs composites being excluded) it reaches 48%. Our binary fraction is not corrected for inclination effects

5.3. Low-mass hot subdwarfs

Most hot subdwarfs are the progeny of low-mass MS stars ($\sim 0.8\text{--}2 M_{\odot}$) that experienced a helium flash, meaning that helium ignition happened under degenerate conditions. This occurs when the helium core reaches a mass in the range of $0.46\text{--}0.51 M_{\odot}$, almost regardless of the progenitor mass for MS stars below $\sim 1.6 M_{\odot}$ (see Fig. 1 of Montalbán & Noels 2013 and chapter 6 of Noels-Grotsch & Miglio 2025). Instead, the exact mass of the He-core at the onset of the He-flash depends on the metallicity (and helium content) of the progenitor, higher metallicity stars experiencing the He-flash at a lower core mass (Iben 1967; Dorman et al. 1993; Salaris & Cassisi 2005). The He-flash may occur at a slightly lower (by about $0.01 M_{\odot}$) core mass if it is delayed until after the progenitor has left the RGB (Brown et al. 2001; Miller Bertolami et al. 2008). Hot subdwarfs less massive than $0.45 M_{\odot}$ are unlikely to have undergone a He-flash. For an sdB with $M \lesssim 0.45 M_{\odot}$ to be burning helium in its core, it must have evolved from a higher mass progenitor ($\sim 2.3\text{--}3.5 M_{\odot}$) that ignited helium quiescently under non-degenerate or semi-degenerate conditions. In such cases, helium ignition can happen at core masses that are as low as $\sim 0.33 M_{\odot}$ (Salaris & Cassisi 2005; Han et al. 2002; Hu et al. 2008; Arancibia-Rojas et al. 2024; Rodríguez-Segovia & Ruiter 2025).

Any such low-mass sdBs should be mostly found below the ZAEHB in the Kiel and HR diagrams. Because the luminosity is less affected by systematic uncertainties than the surface gravity, as explained in Sect. 3.2, we selected our candidate low-mass sdBs from the HRD. We found 11 stars with a luminosity lower than the STELUM ZAEHB track for a $0.45 M_{\odot}$ core (see Fig. 13, top panel). We refer to these as "underluminous" sdBs. Their positions in the HRD are consistent with masses between 0.40 and $0.45 M_{\odot}$. The luminosity of the theoretical EHB band increases with increasing core mass and this effect is visible when color-coding the stars according to their mass (Fig. 13): we see a general increase of the masses with luminosity. On the Kiel diagram (Fig. 13, middle panel), the 11 underluminous sdBs are located below or very close to the ZAEHB.

To verify whether the masses of the underluminous sdBs are indeed lower than the canonical mass, we computed the weighted average and median mass for the 10 underluminous sdBs that have no IR excess⁹. We obtained a weighted average and median mass of $0.40 M_{\odot}$. As a comparison sample, we used the remaining 178 non-composite stars classified as sdBs, iHe-sdBs, and iHe-sdOBs (shown as coloured circles in Fig. 13). We restrict our comparison sample to these spectral types, because the sdOs and He-sdOs are not positioned on the EHB, thus they cannot be found in the region below the ZAEHB. For this comparison sample, we obtained a weighted average and median mass of $0.47 M_{\odot}$. This confirms that the underluminous sdBs are, on average, less massive than stars on the canonical EHB. With the exception of PG1247+554 (see Sect. 5.1), these underluminous sdBs are good candidates for originating from massive progenitors ($\sim 2\text{--}3.5 M_{\odot}$). Our fraction of underluminous sdBs is 5.7% (11/190). This fraction is lower than that obtained by Dawson et al. (in prep.) in their 500 pc sample, which is around 11%¹⁰.

An interesting feature of the underluminous sdBs is that more than half of them are found to be at the "low-helium" end of the T_{eff} -He sequence (see Fig. 13, bottom panel). A simi-

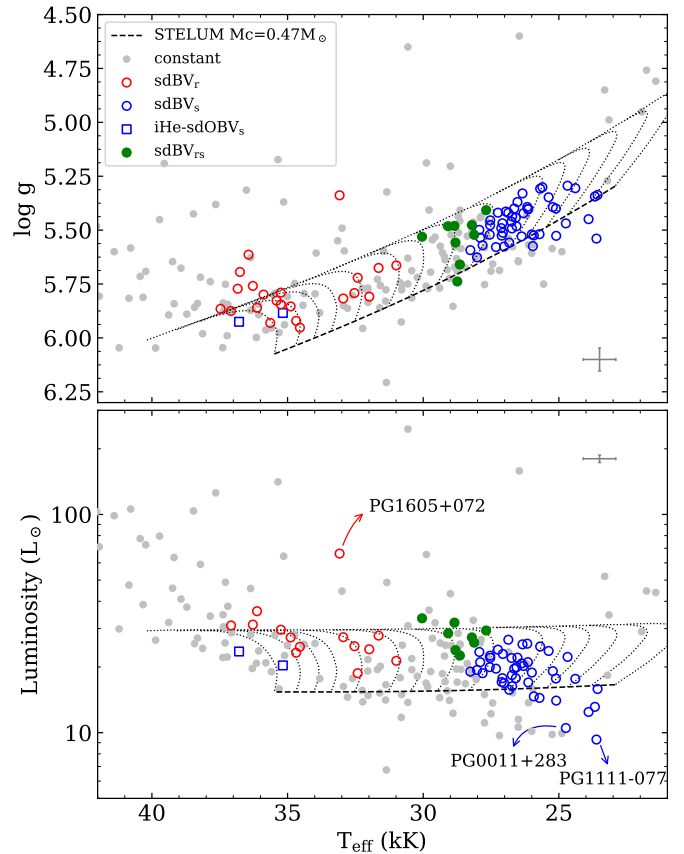


Fig. 14: Position of the pulsating stars in the Kiel (top) and HRD (bottom) diagram. The different types of pulsators are indicated with various symbols: rapid pulsators sdBV_r (open red circles), slow pulsators sdBV_s (open blue circles), and hybrid pulsators sdBV_{rs} (green filled circles). Stars found to be constant are indicated with grey filled circles. Feige 46 and LS IV -14°116 (blue open squares) are peculiar slow pulsators belonging to the small class of iHe-sdOBV (V366 Aqr). The ZAEHB (dashed line) is indicated for a core mass of $0.47 M_{\odot}$ and corresponding evolutionary sequences of the core-helium burning phase are shown for different H-envelope masses (dotted lines). Stars with a poor parallax measurement are excluded in the bottom panel. Representative errors are shown in each panel.

lar behavior is also seen in the 500 pc sample of Dawson et al. (in prep.). Another remarkable peculiarity of the most helium-poor sdBs is the weakness of their metal lines. This is most noticeable when looking at the MMT spectral atlas in Fig. E.1: the spectra with weak or absent He I lines also have very weak metallic lines compared to other spectra of stars at similar T_{eff} . Three underluminous stars with especially low helium are seen on the first panel of Fig. E.1: PG1111-077, PG0856+121, and, PG0250+189. The low-helium sdBs are mainly found below the ZAEHB, consequently they have higher surface gravity than other sdBs at the same temperature. This likely affects the diffusion processes in the atmosphere, because a higher surface gravity means a stronger gravitational pull on the individual atoms. This could explain why low helium and low metal abundances appear to be correlated.

⁹ PG0250+186 is the only underluminous sdB with IR excess.

¹⁰ Note that if we use the same criteria as Dawson et al. to select our underluminous sdBs (i.e. $\log L/L_{\odot} \leq 1.05$), we are left with six stars only, leading to an even lower fraction of 3%.

5.4. Pulsators

Figure 14 shows the hot subdwarfs in the Bok sample for which we have information on the pulsation status, obtained according to the methodology described in Sect. 2.3. We plot them in the Kiel diagram (top panel) and in the HRD (bottom panel). The different types of pulsators are indicated with various symbols, with the sdBV_r being the rapid p -mode pulsators, sdBV_s the slow g -mode pulsators, and sdBV_{rs} the hybrid pulsators showing both p - and g -modes (Kilkenny et al. 2010). As in the Kiel and HR diagrams (Figs. 2 and 5), we observe a lack of sdBV_r pulsators around 33 kK (see Sect. 4.1.2 for more details about this feature). Feige 46 and LS IV -14°116 are two known slow pulsators belonging to the very small group of iHe-sdOBV (or V366 Aqr). This class of pulsator only includes three members so far, which all share very similar pulsation and atmospheric properties (Green et al. 2011; Latour et al. 2019; Østensen et al. 2020), including the extreme heavy-metal abundances characteristic of iHe-sdOBs.

The observational instability regions for the different types of pulsations are well defined, and separated, in both diagrams shown in Fig. 14. The gravity modes are excited from ~ 23.5 kK to about ~ 30 kK in the hottest hybrid pulsators, while pressure modes are found in the 27.5–38 kK range. Our distribution of rapid pulsators is similar to that presented in Baran et al. (2024), with the difference that we do not see any pure p -mode pulsators below 31 kK. However, the number of rapid pulsators in the sample of Baran et al. (2024) is about two times larger than ours, so this could be a selection effect. The constant and pulsating stars are similarly distributed in the Kiel diagram, but in the HRD we noticed that at a given effective temperature, the pulsators are preferentially located at higher luminosities compared to the non-pulsating stars. This trend may be related to the time it takes to build-up the iron/nickel reservoir in the Z-bump region (responsible for the driving of the modes; Charpinet et al. 1997; Fontaine et al. 2003; Jeffery & Saio 2006, 2007) through competing radiative levitation, gravitational settling and other processes (Fontaine & Chayer 1997; Fontaine et al. 2006; Théado et al. 2009; Hu et al. 2011). Stars too close to the ZAEHB may not yet have had time to accumulate enough metals and trigger pulsations.

We also find that within their instability strip, the slow pulsators are very common, and only a few sdB stars colder than 28 kK are found to be non-pulsating from our ground-based and TESS light curves. This is in line with the early estimate of 75% for the fraction of g -mode pulsators (Green et al. 2011), which was further supported by results from the Kepler survey of compact pulsators (Østensen et al. 2011), although based on a smaller number of stars (12 pulsators out of 16 sdBs). In comparison, the rapid pulsators are much less common among the hotter sdB stars. This is especially remarkable taking into account the generally much lower amplitude of g -modes ($\lesssim 0.1\%$) compared to p -modes ($\lesssim 1\%$) and the fact that the latter should be easier to find. The fraction of p -mode pulsators is estimated to be around 10% (Østensen et al. 2010).

The distribution of pulsators on Fig. 14 is compatible with the canonical $0.47 M_{\odot}$ EHB. However, three pulsators stand out as being farther away from the canonical mass EHB. Two of them are found below the ZAEHB and are among the low-mass sdB candidates discussed in Sect. 5.3: PG0011+283 and PG1111–077. Both of these stars also have a very low helium abundance ($\log N(\text{He})/N(\text{H}) \lesssim -3.5$) and their SED masses are smaller than $0.45 M_{\odot}$. We believe they are good candidates for having evolved from a higher-mass progenitor and, as such, are

interesting objects for future asteroseismic analyses. The third outlier is PG1605+075, which is located well above the TAEHB (Heber et al. 1999), indicating that the star is in the post-EHB evolutionary phase, which is supported by the canonical mass derived from the SED fit ($0.49 \pm 0.1 M_{\odot}$). It has unusually high-amplitudes pulsations with five modes above 1%, and a very rich pulsation spectrum (Kilkenny et al. 1999). Several hypotheses have been proposed to explain its unusual pulsation properties, without a convincing picture emerging (richness of the pulsation spectrum explained by fast rotation or by linear combinations between a few high-amplitude pulsation modes; Van Grootel 2008; Van Grootel et al. 2010). Nine sdB pulsators in our Bok sample have masses and radii derived by asteroseismic modeling (PG0014+068, PG1047+003, PG1219+534, Feige 48, PG1325+102, PG0911+456, Balloon090100001, PG1336-018, and KPD0629-0016; Fontaine et al. 2012). We compared the masses and radii from our SED fits to those seismically derived. All measurements agree quite well, within or close to 1-sigma of the SED errors. The only exception is PG0911+456 (Randall et al. 2007), for which radius and mass estimates are a bit different from asteroseismology, but still within 2-sigma of the SED errors.

In Fig. 14 we noticed that the sdBV_r stars are mainly located above the ZAEHB, and are instead found closer to the TAEHB for a core-mass of $0.47 M_{\odot}$. This is especially notable for those hotter than 33 kK and was also reported in Baran et al. (2024) from their sample of TESS p -mode pulsators. However, it is not a property unique to the pulsators, but common to all stars located at the very hot end of the EHB: they sit at higher luminosities than their cooler counterparts. Such a shift could be explained if these stars have slightly higher than canonical masses ($\sim 0.50 M_{\odot}$), but this requires further investigation.

6. Summary and conclusions

We analyzed the spectra of more than 326 relatively bright hot subluminous stars observed with the 2.3m Bok telescope at the Kitt Peak observatory. The combination of size, quality, and homogeneity of this spectroscopic sample is unprecedented. We performed the analysis of the stars in two steps. First, we fit the observed spectra with state-of-the-art model atmospheres, synthetic spectra, and fitting techniques, to derive the atmospheric parameters of the stars, i.e. their T_{eff} , $\log g$, and helium abundance. Secondly, we performed SED fits using parallaxes from *Gaia* DR3 and magnitudes retrieved from various photometric catalogs to derive the stellar parameters radius R , luminosity L , and mass M . The sample includes a wide variety of hot subdwarfs that we separate into different categories based on their atmospheric parameters: sdBs, sdOs, iHe-sdBs, iHe-sdOBs, He-sdBs, and BHBs. From our SED fits we also identified 29 composite systems with an IR-excess indicative of a MS companion. For a subset of 116 stars from the Bok sample, we analyzed additional spectra taken with the MMT telescope. Compared to the Bok spectra, the MMT spectra have a higher resolution but a shorter wavelength coverage.

We summarize below the conclusions drawn from the various aspects of our analysis:

- Spectra must cover the high Balmer lines to constrain the atmospheric parameters with enough accuracy to derive meaningful spectroscopic masses from parallaxes and SED fits. This is the case for our Bok spectra but not for the MMT spectra, which only cover H_{β} , H_{γ} , and H_{δ} . As a result, the atmospheric parameters derived from the MMT spectra lead

to mass estimates that show unrealistic trends with T_{eff} . In contrast, the masses obtained from the atmospheric parameters of the Bok spectra yield nearly constant masses across the T_{eff} range of the sdBs and sdOs (Sect. 4.2.1), which constitutes an important reliability check.

- The distribution of sdBs along the EHB is not continuous. There is a paucity of stars around 33 kK that is clearly visible in both the Kiel and the HR diagrams (Figs. 2, 5). This is also observed among pulsators, with a void of sdBV_r pulsators around 33 kK (Fig. 14). Such a discontinuity was also noticed in the sdB sample of Geier et al. (2022) and is recovered from the evolutionary sequences computed by Xiong et al. (2017). According to these sequences, the stars on opposite sides of the gap experienced the He-flash at different times during their evolution: the hotter ones when they were already contracting on the WD cooling track (the hot- or late-flasher scenario), the cooler ones already at the tip of the RGB. A late-flasher origin for the sdB hotter than ~ 33 kK is consistent with the fact that we derive, on average, canonical masses for these sdBs.
- The helium abundances in our sdBs follow the well-documented trend of helium increasing with T_{eff} , first noticed by Edelmann et al. (2003). In the hottest sdBs, the helium abundances plateau around $\log N(\text{He})/N(\text{H}) = -1.4$ (Fig. 3), not quite reaching the solar value of $\log N(\text{He})/N(\text{H}) = -1.0$, which is commonly used to distinguish between H-rich and He-rich (or intermediate-He) subdwarfs. Based on this observation, we believe that a helium abundance of $\log N(\text{He})/N(\text{H}) = -1.2$ constitutes a more appropriate separator between the H-rich and intermediate-He classes (Sect. 4.1.1). We find that the low T_{eff} and low helium ($\log N(\text{He})/N(\text{H}) \lesssim -3$) tail of the He– T_{eff} relation is sparsely populated and the most He-poor sdBs show very weak metal lines in their MMT spectra (Fig. E.1), if any. In addition, many of the most He-poor sdBs are also located below the ZAEHB for a core-mass of $0.45 M_{\odot}$.
- Our sample includes more than 80 pulsating hot subdwarfs and we found the different types of pulsators (*g*-mode, *p*-mode, and hybrid) to be well separated in both the Kiel and the HR diagrams. We noted that at a given T_{eff} the pulsating sdBs are preferentially found at higher luminosity than their constant counterparts. This trend is possibly related to the time it takes for the iron/nickel reservoir to build-up in the Z-bump region at a sufficient level, through the action of radiative levitation (in competition with other processes), to start driving effectively pulsations.
- Among the stars with MMT spectra, we identified seven objects that show hints of helium stratification from the inspection of the fit of their helium lines, six of which were not known to exhibit such features. They have T_{eff} in a narrow range between 28 and 31 kK, in line with the few stars already known to display helium stratification (Schneider et al. 2018; Geier et al. 2013). Unfortunately, the resolution of our MMT spectra is too low to detect the presence of ${}^3\text{He}$. We believe that stratification, and the presence of ${}^3\text{He}$, is more common than suspected in this temperature range, but detecting it requires at least medium spectral resolution, sufficiently high S/N , and a detailed inspection of the spectral fits (Sect. 4.2.2).
- The H-rich sdBs and sdOs have a similar mass distribution, with a median value around $0.47 M_{\odot}$ (Table 2), in good agreement with the theoretical expectation for the canonical mass at the He-core flash. The dispersions of the sdB and sdO mass distributions are consistent with the uncertainties

of the individual mass measurements, which are around 18% ($\sim 0.08 M_{\odot}$), suggesting no significant intrinsic scatter in the masses of these stars. We see no significant low-mass or high-mass tail in their mass distributions (Sect. 5.1, Fig. 11). Combined with the fact that there is no significant difference between the mass distribution of the close binaries (identified from RV variations) and the single hot subdwarfs, we believe that the merger channels do not significantly contribute to the formation of hydrogen-rich hot subdwarfs (Sect. 5.2).

- Candidates low-mass sdBs ($M < 0.45 M_{\odot}$) selected from their position in the HRD only represent a small fraction ($< 6\%$) of our EHB population (Sect. 5.3). Their masses from parallax and SED fits are, on average, lower than canonical and they are likely the progeny of intermediate-mass MS stars ($2\text{--}3.5 M_{\odot}$) that ignited helium in a non-degenerate core.
- The positions of the He-sdOs in the HRD follow the theoretical helium main sequence remarkably well (Fig. 5). According to their position along this sequence, the majority of them have masses between 0.6 and $1.0 M_{\odot}$, indicating a wider mass range than derived for their H-rich counterparts. The masses obtained from the parallax and SED fits also span a wide range, with 68% of them ($Q_{16}\text{--}Q_{84}$) falling within $0.48\text{--}1.14 M_{\odot}$ and a median mass of $0.78 M_{\odot}$. Their mass dispersion is larger than expected from the individual uncertainties alone (Table 2). A dominant contribution by merger channels is the most likely explanation for this wide mass distribution and relatively large average mass (Sect. 5.1).

7. Data availability

An extended version of Table D.1 including additional information (i.e. columns) for each star is only available online at the CDS via anonymous ftp to [cdsarc.u-strasbg.fr\(XXXX\)](http://cdsarc.u-strasbg.fr/ftp/XXXX) or via <http://cdsarc.u-strasbg.fr/viz-bin/cat/J/A+XXXX/zzz>. All of the Bok spectra analyzed here are available as ascii files at the CDS. Additional figures in Appendix E can be found online (on Zenodo, include link). This includes the MMT spectral atlas, and figures showing the best-fit solutions for the Bok spectra and SED fits of the stars in our sample.

Acknowledgements. We are forever grateful to Gilles Fontaine, who started this project with Betsy Green two decades ago. Thanks to the data and records that he kept, we were able to bring his work to completion and achieve much more than would have been possible in 2005. G.F. would have thanked Pierre Bergeron for his help in the very early phase of this project. We are thankful for those who shared with us their unpublished data to help us track down pulsators and RV variable stars: W. Zong, S. Geier, F. Mattig, H. Dawson, and V. Schaffenroth. M.L. acknowledges funding from the Deutsche Forschungsgemeinschaft (grant LA 4383/4-1). M.D. was supported by the Deutsches Zentrum für Luft- und Raumfahrt (DLR) through grant 50-OR-2304. V.V.G. is a F.R.S.-FNRS Research Associate. S.C. acknowledge support from the Centre National d’Études Spatiales (CNES, France), focused on the mission TESS. This work has made use of data from the European Space Agency (ESA) mission *Gaia* (<https://www.cosmos.esa.int/gaia>), processed by the *Gaia* Data Processing and Analysis Consortium (DPAC, <https://www.cosmos.esa.int/web/gaia/dpac/consortium>). Funding for the DPAC has been provided by national institutions, in particular the institutions participating in the *Gaia* Multilateral Agreement. This work has made use of IRAF, which was distributed by the National Optical Astronomy Observatory, USA, which is operated by the Association of Universities for Research in Astronomy, Inc., under a cooperative agreement with the National Science Foundation. This research has made use of NASA’s Astrophysics Data System Bibliographic Services, of the SIMBAD database (Wenger et al. 2000), operated at CDS, Strasbourg, France, and of the VizieR catalogue access tool (Ochsenbein et al. 2000), CDS, Strasbourg Astronomical Observatory, France (DOI : 10.26093/cds/vizier). This research has made use of TOPCAT (Taylor 2005) and the PYTHON packages pandas (pandas development team 2020) and MATPLOTLIB (Hunter 2007).

References

Ahmad, A., Jeffery, C. S., & Fullerton, A. W. 2004, *A&A*, 418, 275

Alam, S., Albareti, F. D., Allende Prieto, C., et al. 2015, *ApJS*, 219, 12

Arancibia-Rojas, E., Zorotovic, M., Vučković, M., et al. 2024, *MNRAS*, 527, 11184

Asplund, M., Grevesse, N., Sauval, A. J., & Scott, P. 2009, *ARA&A*, 47, 481

Baran, A. S., Charpinet, S., Østensen, R. H., et al. 2024, *A&A*, 686, A65

Baran, A. S., Telting, J. H., Jeffery, C. S., et al. 2019, *MNRAS*, 489, 1556

Barlow, B. N., Corcoran, K. A., Parker, I. M., et al. 2022, *ApJ*, 928, 20

Beauchamp, A., Wesemael, F., & Bergeron, P. 1997, *ApJS*, 108, 559

Bédard, A., Bergeron, P., Brassard, P., & Fontaine, G. 2020, *ApJ*, 901, 93

Bianchi, L., Shiao, B., & Thilker, D. 2017, *ApJS*, 230, 24

Blanchette, J. P., Chayer, P., Wesemael, F., et al. 2008, *ApJ*, 678, 1329

Brassard, P., Fontaine, G., Billères, M., et al. 2001, *ApJ*, 563, 1013

Brown, T. M., Cassisi, S., D'Antona, F., et al. 2016, *ApJ*, 822, 44

Brown, T. M., Sweigart, A. V., Lanz, T., Landsman, W. B., & Hubeny, I. 2001, *ApJ*, 562, 368

Butler, K. & Giddings, J. 1985, College London

Charpinet, S., Fontaine, G., Brassard, P., et al. 2005a, in *Astronomical Society of the Pacific Conference Series*, Vol. 334, 14th European Workshop on White Dwarfs, ed. D. Koester & S. Moehler, 619

Charpinet, S., Fontaine, G., Brassard, P., et al. 1997, *ApJ*, 483, L123

Charpinet, S., Fontaine, G., Brassard, P., & Dorman, B. 2002, *ApJS*, 139, 487

Charpinet, S., Fontaine, G., Brassard, P., Green, E. M., & Chayer, P. 2005b, *A&A*, 437, 575

Charpinet, S., Green, E. M., Baglin, A., et al. 2010, *A&A*, 516, L6

Copperwheat, C. M., Morales-Rueda, L., Marsh, T. R., Maxted, P. F. L., & Heber, U. 2011, *MNRAS*, 415, 1381

Sener, H. T. & Jeffery, C. S. 2014, *MNRAS*, 440, 2676

Culpan, R., Dorsch, M., Geier, S., et al. 2024, *A&A*, 685, A134

D'Cruz, N. L., Dorman, B., Rood, R. T., & O'Connell, R. W. 1996, *ApJ*, 466, 359

De Angelis, F., Weiler, M., Montegriffo, P., et al. 2023, *A&A*, 674, A2

Dorman, B., Rood, R. T., & O'Connell, R. W. 1993, *ApJ*, 419, 596

Dorsch, M. 2024, PhD thesis, Friedrich Alexander University of Erlangen-Nuremberg, Germany

Dorsch, M., Jeffery, C. S., Philip Monai, A., et al. 2024, *A&A*, 691, A165

Dorsch, M., Reindl, N., Pelisoli, I., et al. 2022, *A&A*, 658, L9

Downes, R. A. 1986, *ApJS*, 61, 569

Driebe, T., Schoenberner, D., Bloecker, T., & Herwig, F. 1998, *A&A*, 339, 123

Edelmann, H. 2003, PhD thesis, Friedrich Alexander University of Erlangen-Nuremberg, Germany

Edelmann, H., Heber, U., Hagen, H. J., et al. 2003, *A&A*, 400, 939

Edelmann, H., Heber, U., Lisker, T., & Green, E. M. 2004, *Ap&SS*, 291, 315

Edelmann, H., Heber, U., & Napiwotzki, R. 2001, *Astronomische Nachrichten*, 322, 401

El-Badry, K., Rix, H.-W., & Heintz, T. M. 2021, *MNRAS*, 506, 2269

Feige, J. 1958, *ApJ*, 128, 267

Filiz, S., Werner, K., Rauch, T., & Reindl, N. 2024, *A&A*, 691, A290

Fitzpatrick, E. L., Massa, D., Gordon, K. D., Bohlin, R., & Clayton, G. C. 2019, *ApJ*, 886, 108

Fitzpatrick, M. J., Olsen, K., Economou, F., et al. 2014, in *Society of Photo-Optical Instrumentation Engineers (SPIE) Conference Series*, Vol. 9149, Observatory Operations: Strategies, Processes, and Systems V, ed. A. B. Peck, C. R. Benn, & R. L. Seaman, 91491T

Flewelling, H. 2018, in *American Astronomical Society Meeting Abstracts*, Vol. 231, American Astronomical Society Meeting Abstracts #231, 436.01

Fontaine, G., Bergeron, P., Brassard, P., et al. 2019, *ApJ*, 880, 79

Fontaine, G., Brassard, P., Charpinet, S., & Chayer, P. 2006, *Mem. Soc. Astron. Italiana*, 77, 49

Fontaine, G., Brassard, P., Charpinet, S., et al. 2003, *ApJ*, 597, 518

Fontaine, G., Brassard, P., Charpinet, S., et al. 2012, *A&A*, 539, A12

Fontaine, G. & Chayer, P. 1997, in *The Third Conference on Faint Blue Stars*, ed. A. G. D. Philip, J. Liebert, R. Saffer, & D. S. Hayes, 169

Fontaine, G., Green, E., Brassard, P., Latour, M., & Chayer, P. 2014, in *Astronomical Society of the Pacific Conference Series*, Vol. 481, 6th Meeting on Hot Subdwarf Stars and Related Objects, ed. V. van Grootel, E. Green, G. Fontaine, & S. Charpinet, 83

For, B. Q., Green, E. M., Fontaine, G., et al. 2010, *ApJ*, 708, 253

Geier, S. 2013, *A&A*, 549, A110

Geier, S., Dorsch, M., Pelisoli, I., et al. 2022, *A&A*, 661, A113

Geier, S., Heber, U., Edelmann, H., et al. 2013, *A&A*, 557, A122

Geier, S., Heber, U., Irrgang, A., et al. 2024, *A&A*, 690, A368

Geier, S., Nesslinger, S., Heber, U., et al. 2008, *A&A*, 477, L13

Giddings, J. R. 1981, PhD thesis, -

Gigosos, M. A. & González, M. Á. 2009, *A&A*, 503, 293

Green, E. M., Fontaine, G., Hyde, E. A., For, B. Q., & Chayer, P. 2008, in *Astronomical Society of the Pacific Conference Series*, Vol. 392, Hot Subdwarf Stars and Related Objects, ed. U. Heber, C. S. Jeffery, & R. Napiwotzki, 75

Green, E. M., Fontaine, G., Reed, M. D., et al. 2003, *ApJ*, 583, L31

Green, E. M., For, B., Hyde, E. A., et al. 2004, *Ap&SS*, 291, 267

Green, E. M., For, B. Q., & Hyde, E. A. 2005, in *Astronomical Society of the Pacific Conference Series*, Vol. 334, 14th European Workshop on White Dwarfs, ed. D. Koester & S. Moehler, 363

Green, E. M., Guvenen, B., O'Malley, C. J., et al. 2011, *ApJ*, 734, 59

Green, R. F., Schmidt, M., & Liebert, J. 1986, *ApJS*, 61, 305

Hall, P. D. & Jeffery, C. S. 2016, *MNRAS*, 463, 2756

Han, Z., Podsiadlowski, P., Maxted, P. F. L., & Marsh, T. R. 2003, *MNRAS*, 341, 669

Han, Z., Podsiadlowski, P., Maxted, P. F. L., Marsh, T. R., & Ivanova, N. 2002, *MNRAS*, 336, 449

He, R., Meng, X., Lei, Z., Yan, H., & Lan, S. 2025, *A&A*, 693, A121

Heber, U. 1991, in *IAU Symposium*, Vol. 145, Evolution of Stars: the Photospheric Abundance Connection, ed. G. Michaud & A. V. Tutukov, 363

Heber, U. 2009, *ARA&A*, 47, 211

Heber, U. 2016, *PASP*, 128, 082001

Heber, U. 2024, arXiv e-prints, arXiv:2410.11663

Heber, U., Drechsel, H., Østensen, R., et al. 2004, *A&A*, 420, 251

Heber, U., Irrgang, A., & Schaffenroth, J. 2018, *Open Astronomy*, 27, 35

Heber, U., Reid, I. N., & Werner, K. 1999, *A&A*, 348, L25

Hidalgo, S. L., Pietrinferni, A., Cassisi, S., et al. 2018, *ApJ*, 856, 125

Houck, J. C. & Denicola, L. A. 2000, in *Astronomical Society of the Pacific Conference Series*, Vol. 216, *Astronomical Data Analysis Software and Systems IX*, ed. N. Manset, C. Veillet, & D. Crabtree, 591

Hu, H., Dupret, M. A., Aerts, C., et al. 2008, *A&A*, 490, 243

Hu, H., Tout, C. A., Glebbeek, E., & Dupret, M. A. 2011, *MNRAS*, 418, 195

Hubeny, I., Hummer, D. G., & Lanz, T. 1994, *A&A*, 282, 151

Hubeny, I. & Lanz, T. 2011a, *Synspec: General Spectrum Synthesis Program, Astrophysics Source Code Library*, record ascl:1109.022

Hubeny, I. & Lanz, T. 2011b, *TLUSTY: Stellar Atmospheres, Accretion Disks, and Spectroscopic Diagnostics, Astrophysics Source Code Library*, record ascl:1109.021

Hubeny, I. & Lanz, T. 2017a, arXiv e-prints, arXiv:1706.01859

Hubeny, I. & Lanz, T. 2017b, arXiv e-prints, arXiv:1706.01935

Hubeny, I. & Lanz, T. 2017c, arXiv e-prints, arXiv:1706.01937

Hunter, J. D. 2007, *Computing in Science & Engineering*, 9, 90

Husser, T.-O., Wende-von Berg, S., Dreizler, S., et al. 2013, *A&A*, 553, A6

Iben, Jr., I. 1967, *ApJ*, 147, 624

Irrgang, A., Geier, S., Heber, U., et al. 2021, *A&A*, 650, A102

Irrgang, A., Kreuzer, S., Heber, U., & Brown, W. 2018, *A&A*, 615, L5

Irrgang, A., Przybilla, N., Heber, U., et al. 2014, *A&A*, 565, A63

Irrgang, A., Przybilla, N., & Meynet, G. 2022, *Nature Astronomy*, 6, 1414

Istrate, A. G., Marchant, P., Tauris, T. M., et al. 2016, *A&A*, 595, A35

Jeffery, C. S. 2020, *MNRAS*, 496, 718

Jeffery, C. S., Miszalski, B., & Snowdon, E. 2021, *MNRAS*, 501, 623

Jeffery, C. S. & Saio, H. 2006, *MNRAS*, 371, 659

Jeffery, C. S. & Saio, H. 2007, *MNRAS*, 378, 379

Justham, S., Podsiadlowski, P., & Han, Z. 2011, *MNRAS*, 410, 984

Kilkenny, D., Fontaine, G., Green, E. M., & Schuh, S. 2010, *Information Bulletin on Variable Stars*, 5927, 1

Kilkenny, D., Koen, C., O'Donoghue, D., et al. 1999, *MNRAS*, 303, 525

Koen, C. 2011, *MNRAS*, 415, 3042

Kurucz, R. L. 1996, in *Astronomical Society of the Pacific Conference Series*, Vol. 108, M.A.S.S., *Model Atmospheres and Spectrum Synthesis*, ed. S. J. Adelman, F. Kupka, & W. W. Weiss, 2

Lara, N., González, M. Á., & Gigosos, M. A. 2012, *A&A*, 542, A75

Latour, M., Fontaine, G., Chayer, P., & Brassard, P. 2013, *ApJ*, 773, 84

Latour, M., Fontaine, G., Green, E. M., & Brassard, P. 2015, *A&A*, 579, A39

Latour, M., Green, E. M., & Fontaine, G. 2019, *A&A*, 623, L12

Latour, M., Randall, S. K., Calamida, A., Geier, S., & Moehler, S. 2018, *A&A*, 618, A15

Lei, Z., He, R., Németh, P., et al. 2023, *ApJ*, 953, 122

Lindgren, L., Bastian, U., Biermann, M., et al. 2021, *A&A*, 649, A4

Mason, B. D., Wycoff, G. L., Hartkopf, W. I., Douglass, G. G., & Worley, C. E. 2001, *AJ*, 122, 3466

Maxted, P. F. L., Heber, U., Marsh, T. R., & North, R. C. 2001, *MNRAS*, 326, 1391

Maxted, P. F. L., Marsh, T. R., Heber, U., et al. 2002, *MNRAS*, 333, 231

Maxted, P. F. L., Moran, C. K. J., Marsh, T. R., & Gatti, A. A. 2000, *MNRAS*, 311, 877

Miller Bertolami, M. M., Althaus, L. G., Unglaub, K., & Weiss, A. 2008, *A&A*, 491, 253

Moehler, S. & Heber, U. 1998, *A&A*, 335, 985

Monany, Y., Piotto, G., Recio-Blanco, A., et al. 2002, *ApJ*, 576, L65

Moni Bidin, C., Villanova, S., Piotto, G., Moehler, S., & D'Antona, F. 2011, *ApJ*, 738, L10

Montalbán, J. & Noels, A. 2013, in *European Physical Journal Web of Conferences*, Vol. 43, *European Physical Journal Web of Conferences*, 03002

Morales-Rueda, L., Maxted, P. F. L., Marsh, T. R., North, R. C., & Heber, U. 2003, MNRAS, 338, 752

Napiwotzki, R., Karl, C. A., Lisker, T., et al. 2004, Ap&SS, 291, 321

Naslim, N., Jeffery, C. S., Hibbert, A., & Behara, N. T. 2013, MNRAS, 434, 1920

Newell, B. & Graham, J. A. 1976, ApJ, 204, 804

Nieva, M. F. & Przybilla, N. 2007, A&A, 467, 295

Noels-Grotsch, A. & Miglio, A. 2025, The Golden Gift of Red Giants, 2514-3433 (IOP Publishing)

Norris, J. M., Wright, J. T., Wade, R. A., Mahadevan, S., & Gettel, S. 2011, ApJ, 743, 88

Ochsenbein, F., Bauer, P., & Marcout, J. 2000, A&AS, 143, 23

Østensen, R., Heber, U., & Maxted, P. 2005, in Astronomical Society of the Pacific Conference Series, Vol. 334, 14th European Workshop on White Dwarfs, ed. D. Koester & S. Moehler, 435

Østensen, R., Heber, U., Silvotti, R., et al. 2001, A&A, 378, 466

Østensen, R. H., Jeffery, C. S., Saio, H., et al. 2020, MNRAS, 499, 3738

Østensen, R. H., Oreiro, R., Hu, H., Drechsel, H., & Heber, U. 2008, in Astronomical Society of the Pacific Conference Series, Vol. 392, Hot Subdwarf Stars and Related Objects, ed. U. Heber, C. S. Jeffery, & R. Napiwotzki, 221

Østensen, R. H., Oreiro, R., Solheim, J. E., et al. 2010, A&A, 513, A6

Østensen, R. H., Silvotti, R., Charpinet, S., et al. 2011, MNRAS, 414, 2860

Paczyński, B. 1971, Acta Astron., 21, 1

pandas development team. 2020, pandas-dev/pandas: Pandas

Pelisoli, I., Dorsch, M., Heber, U., et al. 2022, MNRAS, 515, 2496

Pereira, C. 2011, PhD thesis, Queens University Belfast, Ireland

Politano, M., Taam, R. E., van der Sluys, M., & Willems, B. 2008, ApJ, 687, L99

Przybilla, N. 2005, A&A, 443, 293

Przybilla, N. & Butler, K. 2004, ApJ, 609, 1181

Przybilla, N., Butler, K., Becker, S. R., & Kudritzki, R. P. 2006, A&A, 445, 1099

Przybilla, N., Nieva, M.-F., & Butler, K. 2011, in Journal of Physics Conference Series, Vol. 328, Journal of Physics Conference Series, 012015

Randall, S. K., Green, E. M., Van Grootel, V., et al. 2007, A&A, 476, 1317

Ricker, G. R., Winn, J. N., Vanderspek, R., et al. 2014, in Society of Photo-Optical Instrumentation Engineers (SPIE) Conference Series, Vol. 9143, Space Telescopes and Instrumentation 2014: Optical, Infrared, and Millimeter Wave, ed. J. M. Oschmann, Jr., M. Clampin, G. G. Fazio, & H. A. MacEwen, 914320

Riello, M., De Angeli, F., Evans, D. W., et al. 2021, A&A, 649, A3

Rodríguez-Segovia, N. & Ruiter, A. J. 2025, MNRAS, 539, 3273

Saffer, R. A., Bergeron, P., Koester, D., & Liebert, J. 1994, ApJ, 432, 351

Saffer, R. A., Livio, M., & Yungelson, L. R. 1998, ApJ, 502, 394

Saio, H. & Jeffery, C. S. 2000, MNRAS, 313, 671

Saio, H. & Jeffery, C. S. 2002, MNRAS, 333, 121

Salaris, M. & Cassisi, S. 2005, Evolution of Stars and Stellar Populations (Chichester, UK: John Wiley & Sons)

Sandage, A. 1962, ApJ, 135, 333

Schaffenroth, V., Pelisoli, I., Barlow, B. N., Geier, S., & Kupfer, T. 2022, A&A, 666, A182

Schneider, D. 2022, PhD thesis, Friedrich-Alexander-Universität Erlangen-Nürnberg

Schneider, D., Irrgang, A., Heber, U., Nieva, M. F., & Przybilla, N. 2018, A&A, 618, A86

Silvotti, R., Østensen, R., Heber, U., et al. 2002, A&A, 383, 239

Silvotti, R., Østensen, R. H., & Telting, J. H. 2020, arXiv e-prints, arXiv:2002.04545

Skrutskie, M. F., Cutri, R. M., Stiening, R., et al. 2006, AJ, 131, 1163

Snowdon, E. J., Jeffery, C. S., Schlaginhauf, S., & Dorsch, M. 2025, MNRAS, 537, 2079

Stark, M. A. & Wade, R. A. 2003, AJ, 126, 1455

Sweigart, A. V. 1987, ApJS, 65, 95

Taylor, M. B. 2005, in Astronomical Society of the Pacific Conference Series, Vol. 347, Astronomical Data Analysis Software and Systems XIV, ed. P. Shopbell, M. Britton, & R. Ebert, 29

Telting, J. H., Baran, A. S., Nemeth, P., et al. 2014, A&A, 570, A129

Telting, J. H., Østensen, R. H., Baran, A. S., et al. 2012, A&A, 544, A1

Théado, S., Vauclair, S., Alecian, G., & LeBlanc, F. 2009, ApJ, 704, 1262

Tody, D. 1986, in Society of Photo-Optical Instrumentation Engineers (SPIE) Conference Series, Vol. 627, Instrumentation in astronomy VI, ed. D. L. Crawford, 733

Tody, D. 1993, in Astronomical Society of the Pacific Conference Series, Vol. 52, Astronomical Data Analysis Software and Systems II, ed. R. J. Hanisch, R. J. V. Brissenden, & J. Barnes, 173

Tremblay, P. E. & Bergeron, P. 2009, ApJ, 696, 1755

Uzundag, M., Krzesinski, J., Pelisoli, I., et al. 2024, VizieR Online Data Catalog: Pulsating hot subdwarf B stars (Uzundag+, 2024), VizieR On-line Data Catalog: J/A+A/684/A118. Originally published in: 2024A&A..684A.118U

Van Grootel, V. 2008, PhD thesis, University of Montreal, Canada

Van Grootel, V., Charpinet, S., Fontaine, G., & Brassard, P. 2010, Ap&SS, 329, 217

Villaseñor, J. I., Lennon, D. J., Picco, A., et al. 2023, MNRAS, 525, 5121

Vos, J., Németh, P., Vučković, M., Østensen, R., & Parsons, S. 2018, MNRAS, 473, 693

Vos, J., Vučković, M., Chen, X., et al. 2019, MNRAS, 482, 4592

Vučković, M., Aerts, C., Østensen, R., et al. 2007, A&A, 471, 605

Webbink, R. F. 1984, ApJ, 277, 355

Wenger, M., Ochsenbein, F., Egret, D., et al. 2000, A&AS, 143, 9

Werner, K. 1996, ApJ, 457, L39

Werner, K., Reindl, N., Geier, S., & Pritzkuleit, M. 2022, MNRAS, 511, L66

Williams, T., McGraw, J. T., & Grashuis, R. 2001, PASP, 113, 490

Xiong, H., Chen, X., Podsiadlowski, P., Li, Y., & Han, Z. 2017, A&A, 599, A54

Zhang, X. & Jeffery, C. S. 2012, MNRAS, 419, 452

Zong, W., Charpinet, S., Vauclair, G., Giannicchele, N., & Van Grootel, V. 2016, A&A, 585, A22

Appendix A: Stars with composite SED

Twenty nine stars in our sample were found to have IR excess that could be reproduced by a MS companion. The stars are listed in Table A.1, where the atmospheric parameters of the hot subdwarfs are indicated, as well as the T_{eff} , radius R and luminosity L of the companion according to the best fit of the SED. Some of these systems are long period binaries for which the *Gaia* single-star astrometric solution is not necessarily accurate (when $\text{ruwe} \gtrsim 1.4$), thus we also indicate the value of this parameter in the Table. In Fig. A.1, we show the T_{eff} and luminosity of the MS companions as well as the position of the zero-age MS track for two different metallicities. Not all of the stars for which we detected IR-excess were already known to be binaries, and for some of the known binaries, it was not previously clear from the RVs whether the companion was a WD or a low-mass MS star. We briefly discuss a few cases that are of particular interest or that have not been previously reported as composite systems.

HD149382 is the brightest known hot subdwarf. It has been claimed to have a substellar companion on the basis of radial velocity measurements, however no RV variations were detected in follow-up studies (Norris et al. 2011; Silvotti et al. 2020). The star has a visual companion 1'' (75 AU) away that is probably the source of the IR-excess (Østensen et al. 2005), and likely constitute a background object (Schneider 2022).

PB7032 is a slow pulsator (Koen 2011) that has not been reported to be part of a binary system previously. Our SED fit indicates the presence of a M-dwarf companion ($T_{\text{eff}} \sim 3400$ K). The quality of the TESS data for this star is poor and we find no hint of low-frequency variability in the Lomb-Scargle periodogram (LSP) that could be associated with a reflection effect.

PG0014+068 is a rapid pulsator that has been extensively observed with time-series photometry and well-studied from an asteroseismic point of view (Brassard et al. 2001; Charpinet et al. 2005a). It has always been considered a single star and the RVs of the MMT spectra do not show large variations ($\sigma = 2.2 \text{ km s}^{-1}$ for 4 measurements taken within 12 days). However, the SED of the star shows a strong IR excess that can be reproduced with a K-type companion ($T_{\text{eff}} \sim 4700$ K). The TESS light curve of PG0014+068 does not show any sign of a reflection effect. The system possibly has a period of the order of tens of days, or longer.

PG0250+189 shows an IR-excess that corresponds to an early M or late K star ($T_{\text{eff}} \sim 3800$ K). This star is among the few objects located below the ZAEHB (see Fig. 13, but also Saffer et al. 1994). Unfortunately, neither a TESS light curve nor RV measurements were found in the literature.

PG0940+068 is a slowly pulsating sdB and a known binary with a period of 8.33 d (Maxted et al. 2000), however it was initially not clear whether the companion is a WD or dM star. Based on the absence of variations in the TESS light curve, Schaffenroth et al. (2022) classified the companion as a WD. The star's SED shows a mild IR-excess that can be reproduced with a late M-type star ($T_{\text{eff}} \sim 3250$ K).

PG1340+607 is a slowly pulsating sdB that has not previously been reported to be part of a binary system. However, the radial velocities measured from the two MMT spectra showed a difference of 10 km s^{-1} , thus suggesting a possible binary nature. The SED of the star shows a mild IR-excess that can be reproduced with a late M-type star ($T_{\text{eff}} \sim 3300$ K). The LSP of the TESS light curve shows a peak (SNR=8.7) at 3.8h that is separated from the g-modes found at shorter periods. This peak could be due to a reflection effect, although a long-period g-mode can

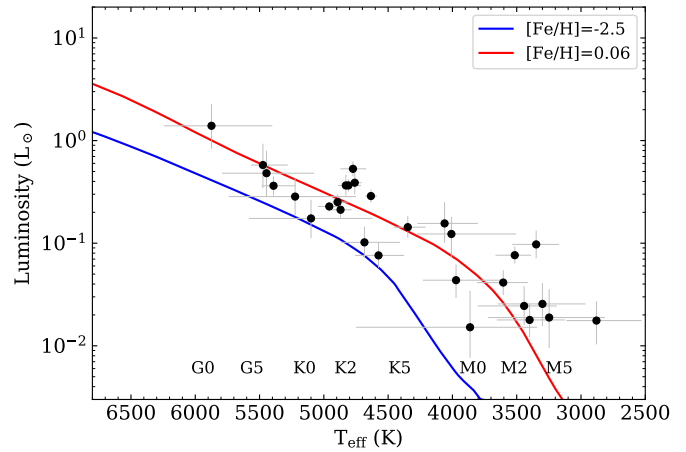


Fig. A.1: HR diagram for the stellar companions of the hot subdwarfs with composite spectra. The parameters are derived from the fits of SED. The solid lines show the expected parameters for MS stars at $[\text{Fe}/\text{H}] = 0.06$ (red) and -2.5 (blue) as obtained from BaSTI isochrones.

not be ruled out. Additional RV measurements are needed to establish the orbital period.

PG2151+100 has been reported as an RV variable star with a faint MS companion but unknown period (Green et al. 2005; Edelmann 2003). Our SED fit suggests the presence of a late M-dwarf star ($T_{\text{eff}} \sim 3300$ K). In addition, the LSP of the TESS data shows a strong signal at 40.06h in an otherwise featureless light curve. The TESS signal is most likely due to the stellar spots on the companion's surface.

PG1101+249 (Feige 36) is a known binary with a period of 8.5 h (Saffer et al. 1998) and a companion that was believed to be a WD. However, the SED shows a mild IR-excess that we reproduce with a stellar companion at $T_{\text{eff}} \sim 3300$ K. The TESS light curve does not show any variability at the orbital period.

PG2317+046 (PB5333) is a known binary for which Edelmann et al. (2004) reported a period of 22.2 h. The SED shows a strong IR excess that we reproduce with an early-M type star ($T_{\text{eff}} \sim 3500$ K). The periodogram of the TESS data shows a clear peak at 19.87 h and the presence of the first harmonic. However recent investigations by Schaffenroth et al. (priv. comm. 2024) found the system to have a much longer period (~ 92 days) and a somewhat hotter companion (K8V).

PG1154-070 is not a known binary, and did not show large RV variations in the study of Saffer et al. (1998). Its IR-excess indicates a late K-type companion ($T_{\text{eff}} \sim 4000$ K).

HS2151+0857 (a *p*-mode pulsator according to Østensen et al. 2001), HS1824+5745 and PG2303+019 (also known as HS2303+0152, and a *p*-mode pulsator according to Silvotti et al. 2002) have IR-excesses that suggest the presence of late K-type companions. The three stars are also part of the sample analyzed by Heber et al. (in prep.) who found similar properties for the companions.

PG0823+546 and PG2158+082 are two hot He-sdO composites with a visible IR-excess that corresponds to early K or late G companions (see also Williams et al. 2001). These are interesting objects given that the fraction of composite systems among He-sdOs is relatively small ($\sim 9\%$, Dorsch 2024) compared to that of sdBs ($\sim 30\%$, Stark & Wade 2003).

Table A.1: Properties of the hot subdwarf systems with IR-excess

Star	T_{eff} (K)	$\log g$ (cm s ⁻²)	$\log N(\text{He})/N(\text{H})$	$T_{\text{eff, comp}}$ (K)	R_{comp} (R_{\odot})	$\log(L_{\text{comp}})$ (L_{\odot})	<i>Gaia</i> ruwe
HD149382	35519	5.80	-1.48	2879 ⁺²³³ ₋₃₅₀	0.54 ^{+0.08} _{-0.05}	-1.75 ^{+0.19} _{-0.23}	1.20
PG0940+068	26953	5.41	-2.79	3247 ⁺⁴⁷⁴ ₋₄₃₃	0.44 ^{+0.08} _{-0.07}	-1.72 ^{+0.28} _{-0.30}	1.02
PG1340+607	25606	5.30	-2.62	3299 ⁺³⁴⁷ ₋₃₃₆	0.49 ^{+0.06} _{-0.06}	-1.59 ^{+0.20} _{-0.22}	1.07
PG2151+100	33946	5.61	-3.66	3348 ⁺¹⁸⁶ ₋₁₇₈	0.93 ^{+0.11} _{-0.09}	-1.01 ^{+0.13} _{-0.13}	2.17
PG1101+249	28841	5.67	-2.01	3399 ⁺²⁵⁵ ₋₂₇₄	0.39 ^{+0.04} _{-0.03}	-1.75 ^{+0.15} _{-0.17}	0.95
PB7032	27122	5.49	-2.82	3442 ⁺³⁶² ₋₂₅₄	0.44 ^{+0.05} _{-0.06}	-1.61 ^{+0.19} _{-0.19}	0.94
PG2317+046	44970	6.05	-2.82	3515 ⁺¹⁴⁹ ₋₁₂₇	0.74 ^{+0.04} _{-0.04}	-1.12 ^{+0.08} _{-0.08}	0.93
FEIGE34	61095	5.92	-1.89	3601 ⁺²⁰⁴ ₋₁₉₂	0.52 ^{+0.05} _{-0.04}	-1.38 ^{+0.12} _{-0.12}	2.24
PG0250+189	25562	5.75	-3.84	3858 ⁺⁹³³ ₋₅₁₁	0.27 ^{+0.04} _{-0.03}	-1.82 ^{+0.37} _{-0.29}	1.10
PG1154-070	27637	5.53	-2.40	3971 ⁺²⁵⁷ ₋₃₄₃	0.45 ^{+0.05} _{-0.04}	-1.36 ^{+0.15} _{-0.17}	3.11
PG1618+563	35405	5.83	-1.69	4006 ⁺²⁶⁸ ₋₅₀₁	0.75 ^{+0.08} _{-0.08}	-0.91 ^{+0.17} _{-0.23}	1.98
HS2151+0857	35883	5.80	-1.42	4060 ⁺²¹¹ ₋₂₅₈	0.80 ^{+0.19} _{-0.13}	-0.81 ^{+0.21} _{-0.19}	0.99
HS1824+5745	35248	5.84	-1.61	4345 ⁺¹²⁹ ₋₁₅₄	0.67 ^{+0.08} _{-0.07}	-0.85 ^{+0.11} _{-0.11}	1.20
PG2303+019	36839	5.77	-1.71	4574 ⁺¹⁸¹ ₋₁₉₉	0.44 ^{+0.05} _{-0.04}	-1.12 ^{+0.12} _{-0.12}	1.03
PG1647+253	36073	5.84	-2.08	4633 ⁺⁴⁴ ₋₄₆	0.83 ^{+0.06} _{-0.06}	-0.54 ^{+0.06} _{-0.06}	1.42
PG0014+068	35638	5.93	-1.62	4684 ⁺¹⁸¹ ₋₂₇₇	0.49 ^{+0.08} _{-0.06}	-0.99 ^{+0.15} _{-0.15}	1.15
PHL1079	32910	5.60	-2.19	4759 ⁺⁴⁸ ₋₅₃	0.92 ^{+0.12} _{-0.11}	-0.41 ^{+0.11} _{-0.11}	4.67
PG1610+519	43897	5.54	-3.14	4773 ⁺⁹⁸ ₋₁₀₃	1.07 ^{+0.08} _{-0.07}	-0.28 ^{+0.07} _{-0.07}	1.98
PG1206+165	28833	5.58	-2.44	4808 ⁺⁷⁶ ₋₇₅	0.87 ^{+0.05} _{-0.05}	-0.44 ^{+0.06} _{-0.06}	2.02
PG1018-047	31448	5.60	-4.00	4828 ⁺⁶¹ ₋₁₁₈	0.87 ^{+0.11} _{-0.09}	-0.44 ^{+0.10} _{-0.10}	3.48
TON357	65722	5.94	-1.85	4870 ⁺⁶⁶ ₋₈₆	0.65 ^{+0.06} _{-0.05}	-0.67 ^{+0.08} _{-0.07}	1.51
PG0749+658	25958	5.57	-3.31	4893 ⁺⁴⁰ ₋₈₅	0.70 ^{+0.05} _{-0.05}	-0.60 ^{+0.07} _{-0.07}	4.49
PG0934+553	45326	5.79	-0.50	4957 ⁺⁸⁹ ₋₁₀₇	0.65 ^{+0.02} _{-0.02}	-0.64 ^{+0.05} _{-0.05}	1.15
PG0823+546	75000	5.76	0.14	5099 ⁺⁴⁸² ₋₄₇₇	0.53 ^{+0.06} _{-0.05}	-0.76 ^{+0.18} _{-0.19}	1.09
PG2158+082	62500	5.86	1.75	5224 ⁺⁵¹⁶ ₋₄₇₃	0.65 ^{+0.06} _{-0.05}	-0.55 ^{+0.18} _{-0.18}	0.94
PG1701+359	33152	5.55	-4.00	5391 ⁺⁹² ₋₁₇₂	0.70 ^{+0.07} _{-0.06}	-0.44 ^{+0.09} _{-0.10}	3.51
HS0252+1025	45138	5.25	-2.65	5445 ⁺³⁴⁵ ₋₃₇₀	0.78 ^{+0.19} _{-0.15}	-0.32 ^{+0.22} _{-0.22}	3.75
PG0154+182	36755	5.69	-1.68	5473 ⁺⁹² ₋₁₉₃	0.86 ^{+0.23} _{-0.19}	-0.24 ^{+0.21} _{-0.22}	1.02
HS0127+3146	39543	5.19	-3.46	5871 ⁺³⁷⁰ ₋₄₇₃	1.16 ^{+0.26} _{-0.21}	0.14 ^{+0.21} _{-0.22}	1.04

Notes. The atmospheric parameters of the hot subdwarfs (T_{eff} , $\log g$, and $\log N(\text{He})/N(\text{H})$) are obtained from the fit of the Bok spectra. The T_{eff} , R , and L of the companions are derived from the SED fits and parallaxes.

Appendix B: Stars removed from the Bok sample

We list here the stars removed from the Bok sample, but whose spectra are still available on Vizier and shown in Fig. B.1.

- PG1704+222 is a low-mass ($\sim 0.55 M_{\odot}$) post-AGB giant star (Moehler & Heber 1998). The fit resulted in $T_{\text{eff}} = 17.5$ kK, $\log g = 2.8$ and a helium abundance close to solar, in agreement with the estimates of Moehler & Heber (1998). This places the star at the lower limit of the model grid in terms of surface gravity.
- PG1544+488 is a sdB binary composed of two similar He-rich sdB stars. This is, up to now, the only known binary system comprising two hot subdwarf stars (Ahmad et al. 2004; Şener & Jeffery 2014). The two components cannot be disentangled in our Bok spectra.
- KPD0311+4801 (WD0311+480) is a very hot DA white dwarf (see e.g. Filiz et al. 2024).
- FBS0132+370 could not be well reproduced by our model atmospheres. We estimate a relatively large T_{eff} of 54 kK, a $\log g = 6$ and some helium enrichment. The spectrum shows a few relatively strong absorption features that correspond to C IV lines. It is an object similar to those recently identi-

fied by Werner et al. (2022) as hot subdwarf stars with atmospheres strongly enhanced in carbon and oxygen, now identified as CO-sdO.

- PG1348+369 shows emission lines in its spectrum. The high Balmer lines (around 3800 Å) and H _{α} are in emission. A LAMOST spectrum was analyzed by Lei et al. (2023) and the authors classified it as a hot sdO star ($T_{\text{eff}} = 65$ kK). They did not report anything peculiar about the object. Our SED fit of the object suggests the presence of an infrared excess, at least when fitting the SED with a stellar T_{eff} of 70 kK. The star is definitely hot as indicated by the strong He II 5412 Å line. The TESS light curve shows a conspicuous periodic signal at 3.316 days along with the first harmonic. This is consistent with the interpretation of Barlow et al. (2022) that this is a reflection effect system in which the emission lines come from the heated side of the dM companion.

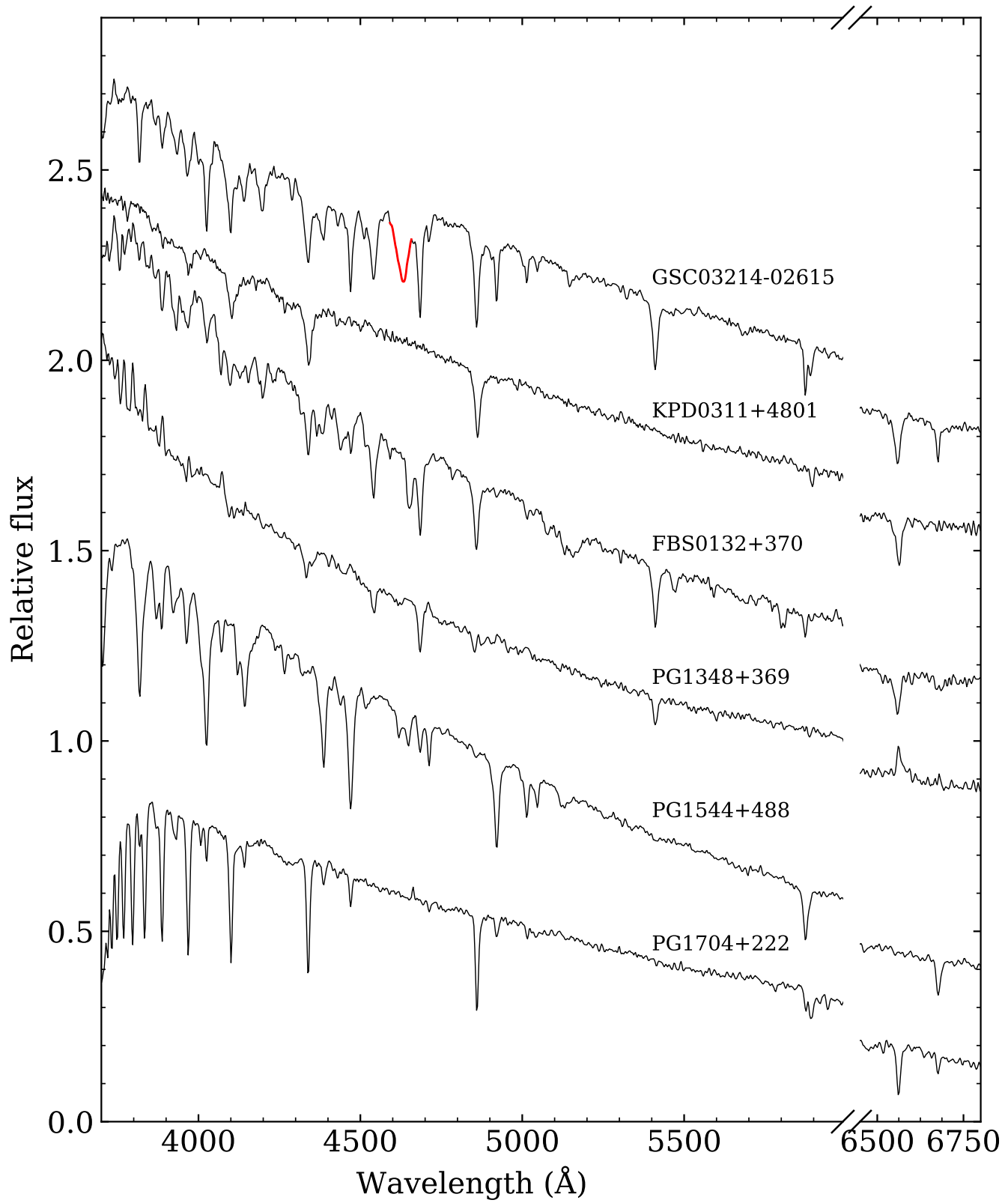


Fig. B.1: Bok spectra of six particular stars. The candidate magnetic star GSC03214-02615 is shown on top, with the distinctive absorption feature around 4600 Å highlighted in red. The five other stars were discarded from the analysis as explained in Sect. 4.1.

Appendix C: PG0215+183

Among the stars in the MMT sample, PG0215+183 stands out because of its high surface gravity obtained from the MMT spectrum. With a $\log g$ of 6.2 and a T_{eff} of 31 kK, the star lies well below the ZAEHB. Its He abundance is low and only He I 4471 Å is visible in the MMT spectrum. At first sight, the fit is good, although a thorough inspection shows that the cores of H_β and H_γ are slightly narrower than the model prediction and H_δ is slightly wider than the model (see Fig. C.1). The atmospheric parameters obtained from the Bok spectrum are significantly different with $T_{\text{eff}} = 29$ kK and $\log g = 5.8$. This is the star with a large $\log g$ difference of 0.4 dex in Fig. 8. Although the atmospheric parameters from the Bok spectrum places the star close to the ZAEHB, and the resulting mass of $0.51 M_\odot$ derived from the parallax and SED fit is normal, the atmospheric fit is obviously poor, as seen in Fig. C.1. We verified that the difference in atmospheric parameters obtained from the two spectra comes from the wavelength range used: fitting the Bok spectrum over the 4000-4950 Å range leads to the same atmospheric parameters as obtained with the MMT spectrum. Currently we do not know why the spectrum of that star cannot be properly reproduced. There are no RV variations from the eight individual MMT spectra ($\sigma_{rv} = 2.5 \text{ km s}^{-1}$), the star is not pulsating and has no IR excess. The spectral fit of spectra taken with a different instrument resulted in the same mismatch between the observed and modeled Balmer lines (H. Dawson, priv. comm. 2025). The effective temperature of the star is in the range where ^3He and stratification are observed, but the Balmer lines in the Bok spectra of the stratified stars discussed in Sect. 4.2.2 are properly reproduced (see also Fig. C.1).

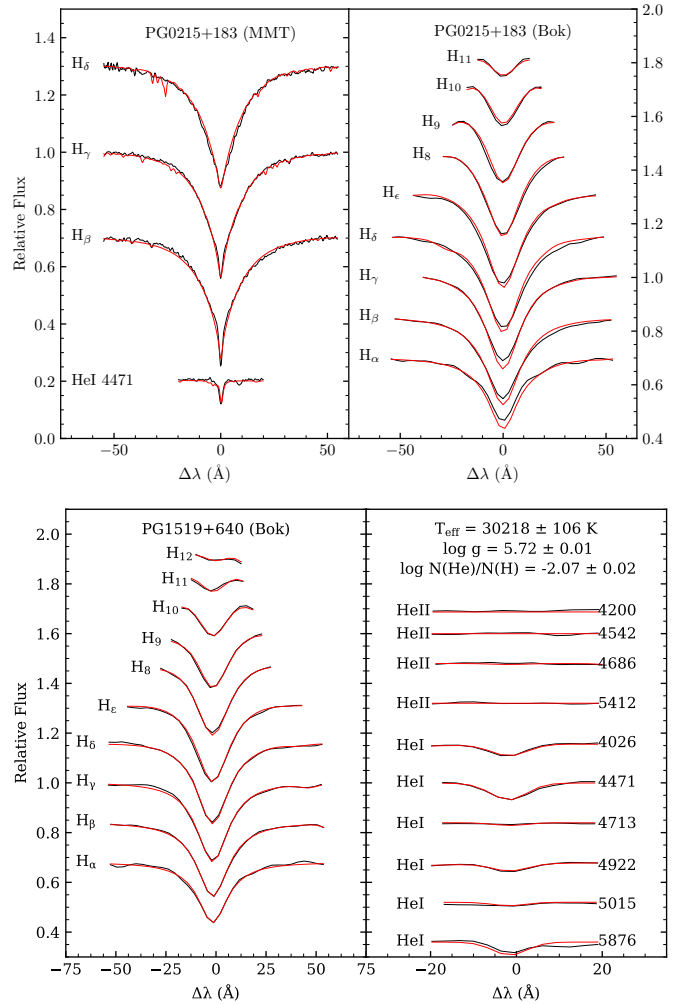


Fig. C.1: Top: respective best fits to the MMT (31.2 kK, $\log g = 6.18$, $\log N(\text{He})/N(\text{H}) = -2.8$) and Bok (28.9 kK, $\log g = 5.85$, $\log N(\text{He})/N(\text{H}) = -3$) spectra of PG0215+183. Bottom: Best fit to the Bok spectrum of PG1519+640, a star with similar atmospheric parameters as PG0215+183 and showing hints of He stratification in its MMT spectrum.

Appendix D: Table of results

Table D.1: Excerpt from the online table of results for all stars in the Bok sample

Star	Type	T_{eff} (K)	$\log g$ (cm s^{-2})	$\log N(\text{He})/N(\text{H})$	R (R_{\odot})	L (L_{\odot})	M (M_{\odot})	IR-excess	<i>Gaia</i> ruwe	Pulsation	Binarity
AGK2+81°266	sdO	59549 ⁺⁴²⁴ ₋₄₀₅	6.03 ^{+0.02} _{-0.02}	-3.07 ^{+0.05} _{-0.06}	0.090 ^{+0.003} _{-0.003}	104.7 ^{+28.8} _{-23.7}	0.36 ^{+0.07} _{-0.06}	no	1.08	no	single
BD+25°4655	He-sdO	38927 ⁺¹¹⁵ ₋₁₃₃	5.68 ^{+0.03} _{-0.04}	1.61 ^{+0.04} _{-0.04}	0.141 ^{+0.002} _{-0.002}	41.0 ^{+3.1} _{-2.9}	0.34 ^{+0.07} _{-0.06}	no	1.22	no	...
BD+28°4211	sdO	70999 ⁺⁵¹⁷ ₋₆₀₃	6.57 ^{+0.02} _{-0.02}	-1.28 ^{+0.02} _{-0.02}	0.065 ^{+0.003} _{-0.001}	99.3 ^{+22.5} _{-22.5}	0.59 ^{+0.12} _{-0.10}	no	1.17	no	single
BD+37°1977	He-sdO	50165 ⁺⁴⁴⁶ ₋₄₀₅	4.25 ^{+0.01} _{-0.00}	1.75 ^{+0.05} _{-0.11}	1.350 ^{+0.144} _{-0.144}	10420.4 ^{+3640.1} _{-2575.6}	1.19 ^{+0.42} _{-0.30}	no	1.06
BD+37°442	He-sdO	50284 ⁺⁴⁰⁸ ₋₄₅₇	4.25 ^{+0.01} _{-0.00}	1.75 ^{+0.04} _{-0.04}	1.063 ^{+0.076} _{-0.076}	6516.8 ^{+1328.0} _{-1328.0}	0.74 ^{+0.20} _{-0.15}	no	1.14
BD+39°3226	He-sdO	45709 ⁺¹²⁰ ₋₁₆₉	5.88 ^{+0.03} _{-0.04}	1.08 ^{+0.09} _{-0.07}	0.165 ^{+0.002} _{-0.002}	107.1 ^{+13.1} _{-12.0}	0.76 ^{+0.16} _{-0.13}	no	1.12	no	...
BD+42°3250	sdB	29000 ⁺¹¹¹ ₋₁₅₀	5.20 ^{+0.02} _{-0.02}	-1.47 ^{+0.02} _{-0.01}	0.261 ^{+0.003} _{-0.003}	43.4 ^{+2.3} _{-2.2}	0.40 ^{+0.07} _{-0.06}	no	1.20	no	binary
BD+48°1777	He-sdO	46462 ⁺⁹² ₋₁₄₂	6.01 ^{+0.02} _{-0.02}	1.15 ^{+0.06} _{-0.08}	0.160 ^{+0.003} _{-0.003}	108.1 ^{+14.5} _{-13.1}	0.95 ^{+0.20} _{-0.16}	no	1.21	no	...
BD+48°2721	sdB	21949 ⁺⁹⁷ ₋₁₃₅	4.95 ^{+0.01} _{-0.01}	-2.09 ^{+0.02} _{-0.02}	0.373 ^{+0.005} _{-0.005}	29.1 ^{+1.7} _{-1.6}	0.45 ^{+0.08} _{-0.06}	no	1.17	no	single
BD+75°325	He-sdO	53733 ⁺²⁸⁸ ₋₃₀₀	5.77 ^{+0.04} _{-0.04}	0.03 ^{+0.02} _{-0.03}	0.153 ^{+0.002} _{-0.002}	175.1 ^{+35.3} _{-35.3}	0.50 ^{+0.11} _{-0.09}	no	1.30	no	...
BD-03°2179	sdO	57033 ⁺⁴⁶⁶ ₋₁₁₀₄	4.38 ^{+0.04} _{-0.02}	-0.57 ^{+0.03} _{-0.03}	0.756 ^{+0.064} _{-0.055}	5445.0 ^{+1802.3} _{-1404.1}	0.51 ^{+0.14} _{-0.11}	no	1.11	no	single
BS15621-0027	sdB	28206 ⁺⁶⁵ ₋₁₀₀	5.51 ^{+0.01} _{-0.01}	-2.89 ^{+0.03} _{-0.03}	0.181 ^{+0.006} _{-0.006}	18.7 ^{+1.5} _{-1.4}	0.39 ^{+0.07} _{-0.06}	no	0.63	no	single
Balloon083500005	MS-B	14326 ⁺¹²⁷ ₋₁₁₉	4.07 ^{+0.03} _{-0.02}	-2.24 ^{+0.09} _{-0.09}	3.083 ^{+0.615} _{-0.440}	360.9 ^{+160.5} _{-97.2}	4.13 ^{+2.00} _{-1.22}	no	1.08
Balloon090100001	sdB	29080 ⁺⁵⁰ ₋₁₃₆	5.48 ^{+0.01} _{-0.01}	-2.73 ^{+0.04} _{-0.04}	0.210 ^{+0.004} _{-0.004}	28.5 ^{+1.7} _{-1.6}	0.49 ^{+0.08} _{-0.07}	no	0.86	h	single
Balloon090100003	MS-B	15148 ⁺⁷² ₋₇₂	4.64 ^{+0.01} _{-0.01}	-1.78 ^{+0.05} _{-0.07}	3.400 ^{+0.275} _{-0.237}	548.7 ^{+97.2} _{-78.1}	18.63 ^{+4.51} _{-3.54}	no	1.12
Balloon090100004	MS-B	15100 ⁺²¹⁴ ₋₈₉	4.51 ^{+0.04} _{-0.02}	-1.64 ^{+0.05} _{-0.09}	2.753 ^{+0.294} _{-0.243}	358.6 ^{+84.9} _{-63.6}	9.10 ^{+2.76} _{-2.00}	no	0.95
Balloon090900004	sdO	45869 ⁺²²⁶ ₋₂₄₉	5.58 ^{+0.02} _{-0.02}	-3.35 ^{+0.05} _{-0.05}	0.190 ^{+0.011} _{-0.010}	144.6 ^{+25.0} _{-21.3}	0.50 ^{+0.12} _{-0.09}	no	0.72	no	single
CBS115	sdB	26863 ⁺⁷³ ₋₁₁₉	5.42 ^{+0.02} _{-0.01}	-2.69 ^{+0.03} _{-0.03}	0.238 ^{+0.008} _{-0.008}	26.6 ^{+2.3} _{-2.1}	0.55 ^{+0.10} _{-0.08}	no	0.69	g	binary
CHSS3497	sdB	30601 ⁺⁶² ₋₁₅₅	5.82 ^{+0.01} _{-0.01}	-2.40 ^{+0.03} _{-0.03}	0.134 ^{+0.003} _{-0.003}	14.1 ^{+1.0} _{-0.9}	0.43 ^{+0.07} _{-0.06}	no	1.05	...	binary
CS22949-0042	sdB	35812 ⁺⁶⁷ ₋₁₅₉	5.80 ^{+0.01} _{-0.01}	-1.50 ^{+0.01} _{-0.01}	0.125 ^{+0.005} _{-0.005}	23.1 ^{+2.9} _{-2.2}	0.36 ^{+0.08} _{-0.06}	no	1.15
CS22963-0036	sdB	26189 ⁺⁸⁷ ₋₁₀₅	5.43 ^{+0.01} _{-0.01}	-2.53 ^{+0.02} _{-0.02}	0.221 ^{+0.006} _{-0.006}	20.7 ^{+1.6} _{-1.4}	0.48 ^{+0.08} _{-0.07}	no	1.03	no	single
EGB5	sdB	35799 ⁺²¹⁷ ₋₁₁₇	5.96 ^{+0.01} _{-0.01}	-2.88 ^{+0.04} _{-0.04}	0.119 ^{+0.004} _{-0.004}	20.9 ^{+2.0} _{-1.8}	0.47 ^{+0.09} _{-0.08}	no	1.16	no	binary
FBS0033+376	sdO	43268 ⁺³⁰⁵ ₋₃₀₅	5.97 ^{+0.03} _{-0.03}	-3.90 ^{+0.10} _{-0.10}	0.107 ^{+0.004} _{-0.004}	35.9 ^{+4.0} _{-4.0}	0.39 ^{+0.07} _{-0.07}	no	1.04	no	binary
FBS0730+617	He-sdO	49011 ⁺¹⁴⁸ ₋₂₂₀	5.98 ^{+0.03} _{-0.02}	0.73 ^{+0.07} _{-0.05}	0.153 ^{+0.007} _{-0.007}	121.6 ^{+23.1} _{-19.8}	0.82 ^{+0.19} _{-0.15}	no	1.01	no	...
FBS0938+788	sdB	27534 ⁺¹⁰⁴ ₋₁₃₅	5.48 ^{+0.01} _{-0.01}	-2.95 ^{+0.05} _{-0.05}	0.209 ^{+0.003} _{-0.003}	22.7 ^{+1.2} _{-1.2}	0.48 ^{+0.08} _{-0.07}	no	1.05	g	sd+MS
FBS1133+754	sdO	39864 ⁺¹³⁴ ₋₉₈	6.05 ^{+0.02} _{-0.01}	-2.24 ^{+0.03} _{-0.03}	0.108 ^{+0.002} _{-0.002}	26.7 ^{+2.2} _{-2.1}	0.48 ^{+0.09} _{-0.07}	no	0.88	no	single
FBS1224+780	sdB	26744 ⁺¹³⁴ ₋₁₂₈	5.46 ^{+0.02} _{-0.02}	-2.75 ^{+0.05} _{-0.05}	0.219 ^{+0.004} _{-0.004}	22.2 ^{+1.4} _{-1.3}	0.51 ^{+0.07} _{-0.07}	no	0.94	g	single
FBS1249+749	sdB	26340 ⁺¹¹⁸ ₋₁₀₈	5.33 ^{+0.02} _{-0.02}	-2.54 ^{+0.03} _{-0.03}	0.243 ^{+0.004} _{-0.004}	25.6 ^{+1.5} _{-1.4}	0.40 ^{+0.08} _{-0.07}	no	1.13	g	single
FBS1529+799	sdO	36362 ⁺¹²³ ₋₈₁	5.63 ^{+0.01} _{-0.01}	-3.49 ^{+0.11} _{-0.20}	0.171 ^{+0.003} _{-0.003}	46.0 ^{+3.2} _{-3.0}	0.45 ^{+0.09} _{-0.07}	no	1.31	no	single
FBS1804+439	BHB	14654 ⁺¹³² ₋₁₁₉	4.28 ^{+0.04} _{-0.03}	-2.44 ^{+0.10} _{-0.10}	1.023 ^{+0.060} _{-0.054}	43.6 ^{+5.9} _{-5.1}	0.73 ^{+0.17} _{-0.13}	no	1.00
FBS2227+379	BHB	14665 ⁺⁵⁸ ₋₇₀	4.09 ^{+0.02} _{-0.01}	-3.42 ^{+0.20} _{-0.34}	1.207 ^{+0.105} _{-0.089}	60.7 ^{+11.5} _{-9.1}	0.65 ^{+0.17} _{-0.13}	no	1.07
FBS2227+383	sdO	44042 ⁺¹⁷⁷ ₋₂₂₉	5.72 ^{+0.02} _{-0.02}	-3.63 ^{+0.10} _{-0.10}	0.148 ^{+0.005} _{-0.005}	74.0 ^{+9.6} _{-8.6}	0.42 ^{+0.09} _{-0.07}	no	1.03	no	single
FEIGE108	sdB	33814 ⁺⁸⁸ ₋₁₂₆	5.88 ^{+0.01} _{-0.01}	-2.92 ^{+0.04} _{-0.04}	0.122 ^{+0.004} _{-0.004}	17.7 ^{+1.5} _{-1.4}	0.42 ^{+0.08} _{-0.06}	no	1.01	no	sd+WD
FEIGE110	sdO	45236 ⁺¹⁵⁷ ₋₁₈₇	6.00 ^{+0.01} _{-0.01}	-1.75 ^{+0.02} _{-0.00}	0.107 ^{+0.002} _{-0.002}	43.5 ^{+5.4} _{-4.9}	0.42 ^{+0.07} _{-0.07}	no	1.14	no	single
FEIGE14	sdB	28748 ⁺⁸¹ ₋₁₀₆	5.69 ^{+0.01} _{-0.01}	-2.83 ^{+0.04} _{-0.04}	0.167 ^{+0.004} _{-0.004}	17.1 ^{+1.2} _{-1.1}	0.49 ^{+0.08} _{-0.07}	no	0.85	no	single
FEIGE26	He-sdO	58221 ⁺⁵⁴² ₋₅₃₅	5.28 ^{+0.04} _{-0.04}	3.50 ^{+0.76} _{-0.76}	0.249 ^{+0.022} _{-0.022}	641.8 ^{+232.9} _{-171.9}	0.43 ^{+0.14} _{-0.10}	no	0.90	no	...
FEIGE34	sdO	61095 ⁺³²⁶ ₋₃₀₂	5.92 ^{+0.01} _{-0.01}	-1.89 ^{+0.01} _{-0.01}	0.102 ^{+0.004} _{-0.004}	131.5 ^{+30.2} _{-30.2}	0.32 ^{+0.05} _{-0.05}	yes	2.24	no	...
FEIGE46	iHe-sdOB	36788 ⁺¹⁰² ₋₁₀	5.92 ^{+0.01} _{-0.01}	-0.34 ^{+0.01} _{-0.01}	0.119 ^{+0.004} _{-0.004}	23.6 ^{+2.1} _{-1.9}	0.44 ^{+0.07} _{-0.07}	no	1.00	g	single
FEIGE48	sdB	30043 ⁺⁷⁴ ₋₁₁₄	5.53 ^{+0.01} _{-0.01}	-2.78 ^{+0.04} _{-0.04}	0.213 ^{+0.006} _{-0.006}	33.4 ^{+2.5} _{-2.3}	0.56 ^{+0.09} _{-0.08}	no	1.01	h	sd+MS
FEIGE66	sdB	35112 ⁺¹³⁹ ₋₁₄₁	5.94 ^{+0.02} _{-0.02}	-1.75 ^{+0.02} _{-0.02}	0.128 ^{+0.002} _{-0.002}	22.6 ^{+1.4} _{-1.3}	0.52 ^{+0.09} _{-0.08}	no	1.28	no	single
FEIGE67	sdO	62153 ⁺⁵⁸² ₋₆₁₈	5.86 ^{+0.02} _{-0.02}	-1.61 ^{+0.02} _{-0.02}	0.114 ^{+0.004} _{-0.004}	174.8 ^{+49.5} _{-40.3}	0.35 ^{+0.07} _{-0.06}	no	1.37	no	single
FEIGE86	BHB	18859 ⁺¹⁹⁹ ₋₁₃₇	4.66 ^{+0.03} _{-0.02}	-2.37 ^{+0.04} _{-0.04}	0.630 ^{+0.012} _{-0.011}	45.3 ^{+3.3} _{-3.0}	0.66 ^{+0.12} _{-0.10}	no	1.09	no	...
FEIGE90	MS-B	14640 ⁺²² ₋₁₄	4.23 ^{+0.01} _{-0.01}	-1.09 ^{+0.01} _{-0.01}	2.794 ^{+0.798} _{-0.508}	323.3 ^{+212.0} _{-107.6}	5.13 ^{+3.52} _{-1.80}	no	1.07
FEIGE91	sdB	30810 ⁺⁶⁰ ₋₇₆	5.93 ^{+0.01} _{-0.01}	-1.99 ^{+0.01} _{-0.01}	0.120 ^{+0.002} _{-0.002}	11.7 ^{+0.7} _{-0.6}	0.45 ^{+0.07} _{-0.06}	no	0.97	no	single
GSC03214-02615	He-sdO	43014 ⁺⁸⁴ ₋₃₆₃	5.72 ^{+0.03} _{-0.03}	0.44 ^{+0.04} _{-0.03}	0.169 ^{+0.006} _{-0.006}	88.0 ^{+10.8} _{-9.8}	0.55 ^{+0.12} _{-0.10}	no	0.98	no	...
NGC 188 2091	sdB	30771 ⁺¹⁴⁹ ₋₁₈₁	5.75 ^{+0.02} _{-0.02}	-2.28 ^{+0.04} _{-0.04}	0.176 ^{+0.014} _{-0.014}	25.2 ^{+3.9} _{-3.9}	0.65 ^{+0.17} _{-0.13}	no	1.03	no	binary
HD149382	sdB	35519 ⁺⁷⁰ ₋₉₉	5.80 ^{+0.01} _{-0.01}	-1.48 ^{+0.01} _{-0.01}	0.137 ^{+0.002} _{-0.002}	27.0 ^{+1.7} _{-1.6}	0.44 ^{+0.08} _{-0.06}	yes	1.20	no	...
HD4539	sdB	24393 ⁺¹²² ₋₁₂₂	5.31 ^{+0.01} _{-0.01}	-2.32 ^{+0.02} _{-0.02}	0.235 ^{+0.004} _{-0.004}	17.6 ^{+1.0} _{-1.0}	0.41 ^{+0.07} _{-0.06}	no	1.47	g	single
HD76431	sdB	30563 ⁺¹²⁵ ₋₁₆₅	4.65 ^{+0.01} _{-0.01}	-1.67 ^{+0.02} _{-0.02}	0.555 ^{+0.011} _{-0.011}	242.1 ^{+15.6} _{-14.8}	0.				

Table D.1: continued.

Star	Type	T_{eff} (K)	$\log g$ (cm s^{-2})	$\log N(\text{He})/N(\text{H})$	R (R_{\odot})	L (L_{\odot})	M (M_{\odot})	IR-excess	<i>Gaia</i> ruwe	Pulsation	Binarity
HS0352+1019	sdB	25996 ⁺⁸⁴ ₋₁₄₃	5.52 ^{+0.01} _{-0.01}	-2.84 ^{+0.04} _{-0.04}	0.214 ^{+0.005} _{-0.005}	18.9 ^{+1.3} _{-1.2}	0.55 ^{+0.09} _{-0.08}	no	1.01	g	single
HS0430+7712	sdB	27065 ⁺⁸⁰ ₋₉₃	5.51 ^{+0.01} _{-0.01}	-2.89 ^{+0.04} _{-0.04}	0.218 ^{+0.005} _{-0.005}	22.9 ^{+1.4} _{-1.4}	0.56 ^{+0.09} _{-0.08}	no	1.16	g	single
HS0444+0458	sdB	35246 ⁺¹⁶³ ₋₁₆₆	5.79 ^{+0.02} _{-0.02}	-1.75 ^{+0.01} _{-0.00}	0.143 ^{+0.013} _{-0.011}	28.6 ^{+5.5} _{-4.4}	0.46 ^{+0.09} _{-0.09}	no	1.02	p	single
HS0457+0907	sdB	37364 ⁺¹⁴¹ ₋₁₅₄	5.88 ^{+0.02} _{-0.02}	-1.51 ^{+0.01} _{-0.01}	0.132 ^{+0.005} _{-0.005}	30.5 ^{+3.1} _{-2.8}	0.48 ^{+0.08} _{-0.08}	no	1.02	no	single
HS0546+8009	sdB	36363 ⁺¹²⁰ ₋₁₉₂	5.87 ^{+0.02} _{-0.02}	-2.15 ^{+0.04} _{-0.04}	0.134 ^{+0.003} _{-0.003}	28.2 ^{+2.1} _{-2.0}	0.49 ^{+0.09} _{-0.08}	no	1.01	no	single
HS0702+6043	sdB	28206 ⁺⁶⁸ ₋₁₆	5.48 ^{+0.01} _{-0.01}	-2.95 ^{+0.03} _{-0.03}	0.219 ^{+0.013} _{-0.011}	27.3 ^{+3.5} _{-3.0}	0.52 ^{+0.10} _{-0.09}	no	0.98	h	single
HS0705+6700	sdB	29562 ⁺¹⁰⁴ ₋₁₆₆	5.53 ^{+0.02} _{-0.02}	-2.75 ^{+0.05} _{-0.05}	0.215 ^{+0.009} _{-0.009}	31.9 ^{+3.3} _{-3.0}	0.58 ^{+0.11} _{-0.09}	no	1.03	no	sd+MS
HS1741+2133	sdO	40431 ⁺²³¹ ₋₁₈₄	5.63 ^{+0.02} _{-0.02}	-2.52 ^{+0.05} _{-0.05}	0.177 ^{+0.005} _{-0.005}	75.8 ^{+7.4} _{-6.7}	0.49 ^{+0.10} _{-0.08}	no	1.04	...	sd+WD
HS1824+5745	sdB	35248 ⁺¹⁰¹ ₋₁₈₇	5.84 ^{+0.01} _{-0.01}	-1.61 ^{+0.02} _{-0.02}	0.125 ^{+0.012} _{-0.012}	21.8 ^{+5.5} _{-4.1}	0.40 ^{+0.12} _{-0.09}	yes	1.20	p	...
HS2126+8320	sdB	27617 ⁺¹⁰² ₋₁₃₀	5.46 ^{+0.02} _{-0.02}	-2.80 ^{+0.05} _{-0.05}	0.205 ^{+0.004} _{-0.004}	22.1 ^{+4.4} _{-3.3}	0.45 ^{+0.07} _{-0.06}	no	0.99	no	single
HS2149+0847	sdB	37469 ⁺¹⁷⁹ ₋₁₇₆	5.87 ^{+0.02} _{-0.02}	-1.75 ^{+0.01} _{-0.00}	0.189 ^{+0.111} _{-0.051}	63.2 ^{+96.2} _{-29.8}	0.96 ^{+1.48} _{-0.46}	no	1.01	p	...
HS2151+0857	sdB	35883 ⁺²³⁸ ₋₁₆₃	5.80 ^{+0.03} _{-0.03}	-1.42 ^{+0.03} _{-0.03}	0.137 ^{+0.031} _{-0.022}	28.2 ^{+14.6} _{-8.4}	0.44 ^{+0.24} _{-0.14}	yes	0.99	p	...
HS2201+2610	sdB	28848 ⁺⁸⁵ ₋₉₈	5.48 ^{+0.01} _{-0.01}	-3.01 ^{+0.04} _{-0.04}	0.226 ^{+0.010} _{-0.010}	31.9 ^{+3.5} _{-3.1}	0.56 ^{+0.11} _{-0.09}	no	1.01	h	single
HS2224+2618	sdB	21769 ⁺¹⁴⁷ ₋₁₆₇	4.76 ^{+0.02} _{-0.02}	-1.89 ^{+0.01} _{-0.01}	0.469 ^{+0.021} _{-0.020}	44.6 ^{+4.9} _{-4.3}	0.46 ^{+0.09} _{-0.07}	no	1.15	no	single
HS2231+2441	sdB	28377 ⁺⁸³ ₋₁₃₂	5.55 ^{+0.01} _{-0.02}	-2.84 ^{+0.04} _{-0.04}	0.189 ^{+0.008} _{-0.008}	20.9 ^{+2.3} _{-2.0}	0.44 ^{+0.08} _{-0.07}	no	1.14	no	sd+MS
HS2333+3927	sdB	38212 ⁺¹⁷⁶ ₋₁₈₃	5.72 ^{+0.02} _{-0.02}	-2.38 ^{+0.03} _{-0.03}	0.175 ^{+0.008} _{-0.008}	59.0 ^{+7.0} _{-6.1}	0.59 ^{+0.12} _{-0.10}	no	1.10	no	sd+MS
HS2357+2201	sdB	28048 ⁺⁶⁸ ₋₈₀	5.62 ^{+0.01} _{-0.01}	-2.71 ^{+0.04} _{-0.04}	0.177 ^{+0.006} _{-0.006}	17.5 ^{+1.5} _{-1.3}	0.48 ^{+0.08} _{-0.07}	no	1.07	no	single
HZ1	He-sdO	39237 ⁺⁴³ ₋₃₅	5.65 ^{+0.01} _{-0.01}	3.50 ^{+0.00} _{-0.00}	0.147 ^{+0.003} _{-0.003}	46.0 ^{+3.8} _{-3.5}	0.35 ^{+0.06} _{-0.05}	no	0.73	no	...
HZ3	He-sdO	42945 ⁺¹¹⁸ ₋₁₂₂	5.84 ^{+0.03} _{-0.03}	0.49 ^{+0.02} _{-0.02}	0.140 ^{+0.005} _{-0.005}	59.8 ^{+7.2} _{-6.4}	0.49 ^{+0.11} _{-0.09}	no	0.98	no	...
HZ44	iHe-sdOB	39182 ⁺¹⁰⁴ ₋₁₂₅	5.84 ^{+0.03} _{-0.03}	0.03 ^{+0.02} _{-0.02}	0.173 ^{+0.004} _{-0.004}	63.5 ^{+5.7} _{-5.2}	0.76 ^{+0.13} _{-0.13}	no	1.33	no	single
KPD0025+5402	sdB	27529 ⁺⁷⁴ ₋₉₇	5.46 ^{+0.01} _{-0.01}	-3.00 ^{+0.04} _{-0.04}	0.206 ^{+0.005} _{-0.005}	22.0 ^{+1.4} _{-1.4}	0.44 ^{+0.06} _{-0.06}	no	1.07	g	binary
KPD0054+5406	sdO	37649 ⁺¹⁶⁴ ₋₁₉₀	5.38 ^{+0.02} _{-0.02}	-2.91 ^{+0.05} _{-0.06}	0.263 ^{+0.009} _{-0.009}	125.5 ^{+12.0} _{-10.9}	0.61 ^{+0.12} _{-0.10}	no	1.01	no	single
KPD0422+5421	sdB	25957 ⁺¹¹⁵ ₋₁₃₇	5.57 ^{+0.02} _{-0.01}	-2.29 ^{+0.02} _{-0.02}	0.197 ^{+0.004} _{-0.004}	15.8 ^{+1.0} _{-0.9}	0.52 ^{+0.09} _{-0.07}	no	1.05	no	sd+WD
KPD0629-0016	sdB	26373 ⁺⁸⁰ ₋₁₀₄	5.53 ^{+0.01} _{-0.01}	-2.81 ^{+0.03} _{-0.03}	0.218 ^{+0.008} _{-0.007}	20.8 ^{+1.8} _{-1.6}	0.59 ^{+0.10} _{-0.09}	no	1.05	g	binary
KPD0716+0258	sdB	25690 ⁺¹⁰⁶ ₋₁₄₉	5.31 ^{+0.02} _{-0.02}	-2.54 ^{+0.03} _{-0.03}	0.252 ^{+0.013} _{-0.012}	24.8 ^{+2.9} _{-2.5}	0.47 ^{+0.08} _{-0.08}	no	0.96	g	single
KPD1901+1607	sdB	27075 ⁺¹⁸³ ₋₁₄₄	5.57 ^{+0.02} _{-0.01}	-2.53 ^{+0.04} _{-0.04}	0.137 ^{+0.008} _{-0.008}	9.1 ^{+1.1} _{-1.1}	0.25 ^{+0.05} _{-0.04}	no	1.65
KPD1924+2932	sdB	30675 ⁺¹⁰⁸ ₋₁₈₇	4.79 ^{+0.02} _{-0.02}	-1.97 ^{+0.02} _{-0.02}	0.559 ^{+0.029} _{-0.027}	248.7 ^{+29.6} _{-25.7}	0.70 ^{+0.14} _{-0.12}	no	1.03	...	single
KPD1930+2752	sdB	36438 ⁺⁹¹ ₋₁₄₂	5.61 ^{+0.01} _{-0.02}	-1.56 ^{+0.01} _{-0.01}	0.213 ^{+0.007} _{-0.007}	71.8 ^{+6.9} _{-6.2}	0.68 ^{+0.13} _{-0.11}	no	1.89	p	sd+WD
KPD1946+4340	sdB	35145 ⁺¹³⁰ ₋₁₂₆	5.37 ^{+0.02} _{-0.02}	-1.39 ^{+0.01} _{-0.01}	0.216 ^{+0.006} _{-0.006}	64.4 ^{+5.4} _{-5.0}	0.40 ^{+0.07} _{-0.06}	no	1.04	no	sd+WD
KPD2026+2205	He-sdO	41726 ⁺⁷³ ₋₁₀₃	5.87 ^{+0.02} _{-0.03}	0.97 ^{+0.03} _{-0.03}	0.151 ^{+0.008} _{-0.007}	62.0 ^{+8.4} _{-7.4}	0.61 ^{+0.14} _{-0.11}	no	1.03
KPD2048+3515	sdO	59031 ⁺⁶⁵⁹ ₋₄₄₃	5.78 ^{+0.03} _{-0.03}	-1.19 ^{+0.03} _{-0.03}	0.148 ^{+0.006} _{-0.006}	239.3 ^{+68.5} _{-55.3}	0.48 ^{+0.11} _{-0.09}	no	1.02	no	single
KPD2109+4401	sdB	30991 ⁺¹⁰⁹ ₋₁₁₃	5.66 ^{+0.02} _{-0.02}	-2.33 ^{+0.02} _{-0.02}	0.160 ^{+0.003} _{-0.003}	21.4 ^{+1.3} _{-1.2}	0.43 ^{+0.06} _{-0.06}	no	0.90	p	single
KPD2118+3841	sdB	31376 ⁺¹³⁶ ₋₁₈₈	5.78 ^{+0.02} _{-0.02}	-1.77 ^{+0.02} _{-0.02}	0.138 ^{+0.003} _{-0.003}	16.6 ^{+1.1} _{-1.0}	0.41 ^{+0.06} _{-0.06}	no	1.02	no	single
KPD2215+5037	sdB	30424 ⁺²³⁸ ₋₂₃₈	5.69 ^{+0.02} _{-0.02}	-2.30 ^{+0.03} _{-0.03}	0.168 ^{+0.004} _{-0.004}	21.8 ^{+1.4} _{-1.4}	0.50 ^{+0.07} _{-0.07}	no	1.02	no	sd+MS
KPD2259+5149	He-sdO	39717 ⁺¹⁰⁸ ₋₇₄	5.45 ^{+0.03} _{-0.02}	2.33 ^{+0.21} _{-0.14}	0.189 ^{+0.006} _{-0.006}	79.6 ^{+7.6} _{-7.0}	0.37 ^{+0.08} _{-0.06}	no	1.04	no	...
KPD2322+4933	He-sdO	55210 ⁺⁶⁷⁰ ₋₃₆₁	4.47 ^{+0.03} _{-0.03}	0.89 ^{+0.06} _{-0.06}	0.770 ^{+0.071} _{-0.071}	4980.5 ^{+1856.1} _{-1350.9}	0.65 ^{+0.21} _{-0.15}	no	1.06	no	...
KUV02445+3633	He-sdO	43152 ⁺⁵² ₋₃₃	5.82 ^{+0.01} _{-0.01}	3.00 ^{+0.50} _{-0.01}	0.179 ^{+0.009} _{-0.009}	99.8 ^{+14.5} _{-12.5}	0.77 ^{+0.17} _{-0.14}	no	1.07	no	...
KUV04402+1455	He-sdO	45283 ⁺¹⁹⁶ ₋₂₇₇	5.76 ^{+0.04} _{-0.05}	1.11 ^{+0.10} _{-0.10}	0.213 ^{+0.004} _{-0.004}	174.4 ^{+21.3} _{-19.5}	0.90 ^{+0.22} _{-0.19}	no	0.94	no	...
KUV04421+1416	sdB	31645 ⁺⁸⁹ ₋₉₅	5.67 ^{+0.01} _{-0.01}	-2.44 ^{+0.03} _{-0.03}	0.176 ^{+0.004} _{-0.004}	27.8 ^{+1.9} _{-1.7}	0.53 ^{+0.09} _{-0.08}	no	1.01	p	sd+MS
KUV08159+4243	sdB	34545 ⁺¹⁰ ₋₁₀	5.95 ^{+0.01} _{-0.01}	-2.12 ^{+0.03} _{-0.03}	0.139 ^{+0.016} _{-0.016}	24.7 ^{+8.3} _{-5.6}	0.63 ^{+0.24} _{-0.16}	no	0.97	p	binary
KUV16256+4034	sdB	23904 ⁺²⁹ ₋₁₆₄	5.45 ^{+0.01} _{-0.01}	-3.00 ^{+0.03} _{-0.03}	0.206 ^{+0.004} _{-0.004}	12.4 ^{+0.8} _{-0.8}	0.43 ^{+0.07} _{-0.06}	no	0.90	g	sd+WD
KUV20417+7604	sdB	26526 ⁺²⁰⁸ ₋₁₀₆	5.37 ^{+0.03} _{-0.01}	-2.86 ^{+0.04} _{-0.04}	0.222 ^{+0.004} _{-0.004}	22.1 ^{+1.4} _{-1.3}	0.42 ^{+0.06} _{-0.06}	no	0.99	g	single
LSI+63°198	sdB	37376 ⁺⁵⁹ ₋₁₄₂	5.84 ^{+0.01} _{-0.01}	-1.62 ^{+0.01} _{-0.01}	0.141 ^{+0.002} _{-0.002}	34.7 ^{+2.4} _{-2.3}	0.50 ^{+0.07} _{-0.07}	no	0.81	no	single
LSII+18°9	sdO	59875 ⁺⁷¹⁰ ₋₆₆₄	5.78 ^{+0.03} _{-0.03}	-1.95 ^{+0.03} _{-0.03}	0.099 ^{+0.004} _{-0.004}	114.3 ^{+32.5} _{-26.4}	0.22 ^{+0.05} _{-0.04}	no	1.12	...	single
LSII+22°21	sdO	71151 ⁺⁸³⁶ ₋₆₄₄	6.38 ^{+0.03} _{-0.03}	-1.06 ^{+0.02} _{-0.02}	0.073 ^{+0.002} _{-0.002}	126.2 ^{+35.7} _{-28.8}	0.48 ^{+0.11} _{-0.08}	no	0.68	no	single
LSIV+00°21	sdB	37303 ⁺¹²² ₋₁₀₃	5.85 ^{+0.01} _{-0.01}	-1.73 ^{+0.01} _{-0.01}	0.128 ^{+0.003} _{-0.003}	28.0 ^{+2.4} _{-2.2}	0.43 ^{+0.07} _{-0.07}	no	0.62	no	single
LSIV+10°9	He-sdO	44568 ⁺³²⁹ ₋₃₁₅	5.80 ^{+0.07} _{-0.07}	1.23 ^{+0.12} _{-0.08}	0.195 ^{+0.006} _{-0.006}	134.8 ^{+17.7} _{-15.8}	0.87 ^{+0.19} _{-0.19}	no	1.05	no	...
PB3524	sdB	29834 ⁺¹¹² ₋₁₀₄	5.77 ^{+0.02} _{-0.02}	-1.88 ^{+0.01} _{-0.01}	0.151 ^{+0.003} _{-0.003}	16.2 ^{+1.1} _{-1.0}	0.49 ^{+0.07} _{-0.07}	no	1.07	no	single
PB5450	sdB	28743 ⁺⁴⁴ ₋₁₂₈	5.74 ^{+0.02} _{-0.02}	-2.80 ^{+0.03} _{-0.03}	0.130 ^{+0.007} _{-0.007}	10.4 ^{+1.4} _{-1.1}	0.34 ^{+0.06} _{-0.06}	no	0.99</		

Table D.1: continued.

Star	Type	T_{eff} (K)	$\log g$ (cm s^{-2})	$\log N(\text{He})/N(\text{H})$	R (R_{\odot})	L (L_{\odot})	M (M_{\odot})	IR-excess	<i>Gaia</i> ruwe	Pulsation	Binarity
PG0032+247	sdO	38221 $^{+147}_{-159}$	5.63 $^{+0.02}_{-0.02}$	-3.20 $^{+0.07}_{-0.07}$	0.172 $^{+0.008}_{-0.008}$	56.7 $^{+6.9}_{-6.0}$	0.46 $^{+0.10}_{-0.08}$	no	0.99	...	single
PG0033+266	sdB	26706 $^{+158}_{-108}$	5.58 $^{+0.02}_{-0.02}$	-2.45 $^{+0.03}_{-0.03}$	0.182 $^{+0.007}_{-0.007}$	15.2 $^{+1.4}_{-1.3}$	0.46 $^{+0.08}_{-0.07}$	no	1.11	no	single
PG0039+135	He-sdO	47860 $^{+145}_{-156}$	5.97 $^{+0.03}_{-0.03}$	1.03 $^{+0.08}_{-0.06}$	0.195 $^{+0.008}_{-0.007}$	180.6 $^{+30.2}_{-26.3}$	1.31 $^{+0.24}_{-0.24}$	no	0.95	no	...
PG0057+155	sdB	34736 $^{+65}_{-91}$	5.75 $^{+0.01}_{-0.01}$	-1.68 $^{+0.01}_{-0.01}$	0.143 $^{+0.003}_{-0.003}$	26.9 $^{+1.9}_{-1.7}$	0.42 $^{+0.07}_{-0.06}$	no	1.03	no	single
PG0101+039	sdB	27108 $^{+72}_{-72}$	5.53 $^{+0.01}_{-0.01}$	-2.75 $^{+0.03}_{-0.03}$	0.187 $^{+0.004}_{-0.004}$	17.0 $^{+1.0}_{-1.0}$	0.43 $^{+0.07}_{-0.06}$	no	0.85	g	sd+WD
PG0105+276	He-sdO	64031 $^{+800}_{-710}$	5.47 $^{+0.04}_{-0.04}$	0.42 $^{+0.03}_{-0.00}$	0.275 $^{+0.046}_{-0.035}$	1150.5 $^{+546.4}_{-357.0}$	0.82 $^{+0.36}_{-0.23}$	no	0.94
PG0108+195	sdO	45672 $^{+284}_{-326}$	6.11 $^{+0.03}_{-0.03}$	-2.13 $^{+0.05}_{-0.05}$	0.122 $^{+0.005}_{-0.005}$	58.0 $^{+9.4}_{-8.1}$	0.69 $^{+0.16}_{-0.13}$	no	0.93	no	single
PG0123+159	sdB	29215 $^{+104}_{-133}$	5.62 $^{+0.02}_{-0.02}$	-2.41 $^{+0.04}_{-0.04}$	0.185 $^{+0.007}_{-0.007}$	22.4 $^{+2.1}_{-1.9}$	0.52 $^{+0.08}_{-0.08}$	no	1.09	no	single
PG0133+114	sdB	29112 $^{+104}_{-145}$	5.68 $^{+0.01}_{-0.02}$	-2.43 $^{+0.02}_{-0.02}$	0.155 $^{+0.005}_{-0.005}$	15.5 $^{+1.3}_{-1.2}$	0.42 $^{+0.07}_{-0.06}$	no	0.83	no	sd+WD
PG0142+148	sdB	29176 $^{+68}_{-130}$	5.48 $^{+0.01}_{-0.01}$	-3.11 $^{+0.06}_{-0.06}$	0.197 $^{+0.007}_{-0.006}$	25.2 $^{+2.1}_{-1.9}$	0.43 $^{+0.07}_{-0.06}$	no	0.95	no	binary
PG0154+182	sdB	36755 $^{+153}_{-178}$	5.69 $^{+0.02}_{-0.02}$	-1.68 $^{+0.02}_{-0.02}$	0.133 $^{+0.008}_{-0.016}$	29.3 $^{+1.7}_{-6.7}$	0.33 $^{+0.20}_{-0.09}$	yes	1.02	p	...
PG0206+225	sdB	31579 $^{+94}_{-146}$	5.76 $^{+0.01}_{-0.02}$	-2.52 $^{+0.02}_{-0.02}$	0.150 $^{+0.004}_{-0.004}$	20.1 $^{+1.5}_{-1.4}$	0.47 $^{+0.08}_{-0.07}$	no	1.09	no	single
PG0209-015	sdB	24679 $^{+111}_{-140}$	5.29 $^{+0.02}_{-0.02}$	-2.64 $^{+0.03}_{-0.03}$	0.258 $^{+0.012}_{-0.011}$	22.2 $^{+2.4}_{-2.1}$	0.48 $^{+0.09}_{-0.08}$	no	0.95	g	single
PG0215+183	sdB	28902 $^{+10}_{-10}$	5.85 $^{+0.01}_{-0.01}$	-3.01 $^{+0.04}_{-0.05}$	0.140 $^{+0.004}_{-0.004}$	12.3 $^{+0.9}_{-0.8}$	0.51 $^{+0.09}_{-0.07}$	no	1.18	no	single
PG0229+064	BHB	20413 $^{+173}_{-168}$	4.68 $^{+0.03}_{-0.03}$	-0.88 $^{+0.01}_{-0.01}$	0.556 $^{+0.018}_{-0.017}$	48.4 $^{+4.3}_{-3.9}$	0.54 $^{+0.10}_{-0.09}$	no	1.17	g	...
PG0240+046	iHe-sdOB	36150 $^{+140}_{-185}$	6.00 $^{+0.03}_{-0.04}$	0.30 $^{+0.01}_{-0.01}$	0.116 $^{+0.004}_{-0.004}$	20.8 $^{+2.0}_{-1.8}$	0.49 $^{+0.10}_{-0.08}$	no	1.19	no	single
PG0242+132	sdB	31341 $^{+104}_{-113}$	5.32 $^{+0.01}_{-0.02}$	-1.55 $^{+0.02}_{-0.02}$	0.237 $^{+0.007}_{-0.007}$	48.8 $^{+3.8}_{-3.5}$	0.43 $^{+0.08}_{-0.07}$	no	0.90	no	single
PG0250+189	sdB	25562 $^{+46}_{-39}$	5.75 $^{+0.01}_{-0.01}$	-3.84 $^{+0.10}_{-0.10}$	0.147 $^{+0.004}_{-0.006}$	8.2 $^{+0.6}_{-0.7}$	0.44 $^{+0.07}_{-0.06}$	yes	1.10	no	...
PG0314+146	He-sdO	47199 $^{+112}_{-171}$	5.93 $^{+0.02}_{-0.03}$	3.50 $^{+0.00}_{-0.00}$	0.167 $^{+0.005}_{-0.005}$	124.1 $^{+18.9}_{-16.7}$	0.86 $^{+0.15}_{-0.15}$	no	1.03	no	...
PG0342+026	sdB	25713 $^{+45}_{-46}$	5.52 $^{+0.01}_{-0.01}$	-2.73 $^{+0.03}_{-0.03}$	0.191 $^{+0.002}_{-0.002}$	14.4 $^{+0.7}_{-0.7}$	0.44 $^{+0.06}_{-0.06}$	no	1.09	g	single
PG0749+658	sdB	25958 $^{+97}_{-74}$	5.57 $^{+0.01}_{-0.01}$	-3.31 $^{+0.07}_{-0.07}$	0.148 $^{+0.007}_{-0.007}$	9.0 $^{+1.4}_{-1.0}$	0.30 $^{+0.05}_{-0.05}$	yes	4.49	g	...
PG0823+546	He-sdO	75000 $^{+1485}_{-1485}$	5.76 $^{+0.04}_{-0.04}$	0.14 $^{+0.03}_{-0.03}$	0.130 $^{+0.010}_{-0.010}$	476.6 $^{+159.3}_{-124.3}$	0.36 $^{+0.08}_{-0.08}$	yes	1.09	no	...
PG0838+133	He-sdO	47177 $^{+174}_{-191}$	5.82 $^{+0.04}_{-0.04}$	1.04 $^{+0.07}_{-0.07}$	0.234 $^{+0.013}_{-0.013}$	243.7 $^{+38.3}_{-38.3}$	1.32 $^{+0.28}_{-0.28}$	no	1.01	no	...
PG0848+186	BHB	19156 $^{+180}_{-147}$	4.69 $^{+0.03}_{-0.03}$	-0.83 $^{+0.02}_{-0.02}$	0.527 $^{+0.025}_{-0.025}$	33.7 $^{+4.1}_{-3.6}$	0.49 $^{+0.10}_{-0.09}$	no	1.00	g	...
PG0849+319	sdB	28697 $^{+32}_{-96}$	5.51 $^{+0.01}_{-0.01}$	-3.08 $^{+0.06}_{-0.07}$	0.191 $^{+0.011}_{-0.011}$	22.3 $^{+3.1}_{-2.6}$	0.43 $^{+0.07}_{-0.07}$	no	1.08	no	sd+WD
PG0850+170	sdB	26722 $^{+75}_{-107}$	5.44 $^{+0.01}_{-0.01}$	-2.74 $^{+0.03}_{-0.03}$	0.189 $^{+0.008}_{-0.008}$	16.3 $^{+1.6}_{-1.5}$	0.35 $^{+0.06}_{-0.06}$	no	1.08	g	sd+WD
PG0856+121	sdB	24890 $^{+41}_{-85}$	5.60 $^{+0.01}_{-0.01}$	-3.80 $^{+0.08}_{-0.08}$	0.169 $^{+0.004}_{-0.004}$	9.9 $^{+0.7}_{-0.6}$	0.42 $^{+0.06}_{-0.06}$	no	1.02	no	single
PG0902+057	He-sdO	40845 $^{+55}_{-45}$	5.82 $^{+0.02}_{-0.02}$	1.82 $^{+0.06}_{-0.05}$	0.138 $^{+0.007}_{-0.007}$	47.5 $^{+6.7}_{-5.8}$	0.45 $^{+0.10}_{-0.08}$	no	1.20	no	...
PG0907+123	sdB	26645 $^{+50}_{-90}$	5.40 $^{+0.01}_{-0.01}$	-2.92 $^{+0.03}_{-0.03}$	0.208 $^{+0.007}_{-0.007}$	19.6 $^{+1.7}_{-1.5}$	0.40 $^{+0.06}_{-0.06}$	no	1.01	g	sd+WD
PG0909+164	sdO	40781 $^{+10}_{-10}$	5.58 $^{+0.01}_{-0.01}$	-3.18 $^{+0.05}_{-0.05}$	0.206 $^{+0.012}_{-0.011}$	105.9 $^{+15.7}_{-13.3}$	0.59 $^{+0.13}_{-0.11}$	no	0.98	no	binary
PG0909+276	iHe-sdOB	36300 $^{+82}_{-93}$	5.87 $^{+0.01}_{-0.01}$	-0.92 $^{+0.01}_{-0.01}$	0.112 $^{+0.003}_{-0.003}$	19.7 $^{+1.5}_{-1.4}$	0.34 $^{+0.06}_{-0.05}$	no	0.70	no	single
PG0911+456	sdB	31988 $^{+55}_{-87}$	5.81 $^{+0.01}_{-0.01}$	-2.50 $^{+0.01}_{-0.01}$	0.160 $^{+0.008}_{-0.008}$	24.1 $^{+2.5}_{-2.5}$	0.60 $^{+0.12}_{-0.10}$	no	0.97	p	binary
PG0918+029	sdB	31387 $^{+167}_{-117}$	5.83 $^{+0.02}_{-0.01}$	-2.42 $^{+0.02}_{-0.02}$	0.127 $^{+0.004}_{-0.004}$	14.1 $^{+1.1}_{-1.0}$	0.40 $^{+0.06}_{-0.06}$	no	1.04	no	sd+WD
PG0919+273	sdB	32791 $^{+78}_{-84}$	5.86 $^{+0.01}_{-0.01}$	-2.34 $^{+0.02}_{-0.02}$	0.118 $^{+0.004}_{-0.004}$	14.6 $^{+1.2}_{-1.1}$	0.37 $^{+0.06}_{-0.06}$	no	0.70	no	sd+WD
PG0920+029	sdB	28641 $^{+76}_{-160}$	5.41 $^{+0.01}_{-0.01}$	-3.01 $^{+0.06}_{-0.06}$	0.205 $^{+0.011}_{-0.011}$	25.4 $^{+3.2}_{-2.8}$	0.39 $^{+0.08}_{-0.06}$	no	1.10	no	single
PG0933+004	sdB	37201 $^{+92}_{-217}$	5.84 $^{+0.01}_{-0.01}$	-1.55 $^{+0.02}_{-0.02}$	0.148 $^{+0.007}_{-0.007}$	37.9 $^{+4.7}_{-4.1}$	0.56 $^{+0.12}_{-0.10}$	no	1.04	no	single
PG0934+186	sdO	37291 $^{+177}_{-142}$	5.75 $^{+0.02}_{-0.01}$	-3.37 $^{+0.07}_{-0.07}$	0.168 $^{+0.006}_{-0.006}$	48.9 $^{+5.1}_{-4.5}$	0.58 $^{+0.09}_{-0.09}$	no	0.98	no	sd+WD
PG0934+553	sdO	45326 $^{+83}_{-113}$	5.79 $^{+0.01}_{-0.01}$	-0.50 $^{+0.01}_{-0.01}$	0.150 $^{+0.004}_{-0.004}$	85.9 $^{+11.4}_{-10.2}$	0.50 $^{+0.10}_{-0.09}$	yes	1.15	no	...
PG0940+068	sdB	26953 $^{+83}_{-101}$	5.41 $^{+0.01}_{-0.01}$	-2.79 $^{+0.03}_{-0.03}$	0.214 $^{+0.009}_{-0.009}$	21.9 $^{+2.2}_{-1.9}$	0.44 $^{+0.08}_{-0.07}$	yes	1.02	g	sd+WD
PG0941+280	sdB	29372 $^{+77}_{-116}$	5.57 $^{+0.01}_{-0.01}$	-3.44 $^{+0.06}_{-0.06}$	0.196 $^{+0.007}_{-0.007}$	25.8 $^{+2.3}_{-2.1}$	0.53 $^{+0.09}_{-0.08}$	no	1.04	no	sd+WD
PG0942-029	sdO	45122 $^{+154}_{-177}$	6.26 $^{+0.01}_{-0.02}$	-4.00 $^{+0.00}_{-0.00}$	0.081 $^{+0.003}_{-0.002}$	24.5 $^{+3.2}_{-2.9}$	0.43 $^{+0.09}_{-0.07}$	no	1.05	no	single
PG0952+519	He-sdO	49416 $^{+116}_{-116}$	6.14 $^{+0.03}_{-0.03}$	1.22 $^{+0.14}_{-0.09}$	0.155 $^{+0.006}_{-0.005}$	128.3 $^{+23.9}_{-20.5}$	1.20 $^{+0.22}_{-0.22}$	no	0.62	no	...
PG0958-073	sdB	26496 $^{+52}_{-64}$	5.64 $^{+0.01}_{-0.01}$	-3.55 $^{+0.08}_{-0.08}$	0.155 $^{+0.003}_{-0.003}$	10.6 $^{+0.6}_{-0.6}$	0.38 $^{+0.06}_{-0.05}$	no	0.97	no	sd+WD
PG1000+408	sdO	43062 $^{+160}_{-163}$	5.54 $^{+0.02}_{-0.02}$	-3.00 $^{+0.03}_{-0.03}$	0.207 $^{+0.009}_{-0.009}$	132.2 $^{+18.4}_{-16.1}$	0.54 $^{+0.12}_{-0.10}$	no	1.01	no	sd+WD
PG1008+689	BHB	18461 $^{+60}_{-109}$	4.54 $^{+0.01}_{-0.01}$	-2.00 $^{+0.02}_{-0.02}$	0.585 $^{+0.018}_{-0.017}$	35.8 $^{+2.9}_{-2.7}$	0.44 $^{+0.08}_{-0.06}$	no	1.01
PG1017-086	sdB	30564 $^{+70}_{-84}$	5.63 $^{+0.01}_{-0.01}$	-2.84 $^{+0.04}_{-0.04}$	0.197 $^{+0.009}_{-0.009}$	30.4 $^{+3.1}_{-3.1}$	0.60 $^{+0.12}_{-0.10}$	no	1.04	no	binary
PG1018-047	sdB	31448 $^{+147}_{-134}$	5.60 $^{+0.02}_{-0.02}$	-4.00 $^{+0.00}_{-0.00}$	0.199 $^{+0.019}_{-0.019}$	34.8 $^{+8.9}_{-6.5}$	0.57 $^{+0.13}_{-0.13}$	yes	3.48	no	...
PG1032+406	sdB	31601 $^{+85}_{-88}$	5.86 $^{+0.01}_{-0.01}$	-2.28 $^{+0.02}_{-0.02}$	0.130 $^{+0.002}_{-0.002}$	15.2 $^{+0.8}_{-0.8}$	0.45 $^{+0.06}_{-0.06}$	no	1.29	no	sd+WD
PG1039+219	sdB	33988 $^{+115}_{-107}$	5.80 $^{+0.02}_{-0.02}$	-2.19 $^{+0.02}_{-0.02}$	0.146 $^{+0.005}_{-0.005}$	25.6 $^{+2.0}_{-2.0}$	0.49 $^{+0.08}_{-0.08}$	no	1.01	no	single
PG1043+760	sdB	28262 $^{+27}_{-79}$	5.59 $^{+0.01}_{-0.01}$	-3.06 $^{+0.06}_{-0.06}$	0.182 $^{+0.004}_{-0.004}$	19.0 $^{+1.1}_{-1.1}$	0.47 $^{+0.07}_{-0.07}$	no	1.06	g	sd+WD
PG1047+003	sdB	36125 $^{+57}_{-144}$	5.86 $^{+0.01}_{-0.01}$	-1.93 $^{+0.$							

Table D.1: continued.

Star	Type	T_{eff} (K)	$\log g$ (cm s^{-2})	$\log N(\text{He})/N(\text{H})$	R (R_{\odot})	L (L_{\odot})	M (M_{\odot})	IR-excess	<i>Gaia</i> ruwe	Pulsation	Binarity
PG1116+301	sdB	32044 ⁺⁸⁶ ₋₁₁₁	5.78 ^{+0.01} _{-0.02}	-2.07 ^{+0.03} _{-0.04}	0.142 ^{+0.005} _{-0.005}	19.2 ^{+1.7} _{-1.6}	0.44 ^{+0.08} _{-0.07}	no	1.02	no	sd+WD
PG1118+061	sdB	28695 ⁺¹¹⁰ ₋₁₄₅	5.51 ^{+0.02} _{-0.02}	-3.46 ^{+0.11} _{-0.15}	0.219 ^{+0.010} _{-0.009}	29.4 ^{+3.1} _{-2.7}	0.57 ^{+0.11} _{-0.09}	no	1.03	...	single
PG1127+019	He-sdO	42713 ⁺¹³¹ ₋₁₄₅	5.93 ^{+0.03} _{-0.03}	1.86 ^{+0.19} _{-0.16}	0.164 ^{+0.009} _{-0.008}	80.9 ^{+12.3} _{-10.5}	0.84 ^{+0.20} _{-0.16}	no	1.13	no	...
PG1154-070	sdB	27637 ⁺⁷¹ ₋₁₄₉	5.53 ^{+0.01} _{-0.02}	-2.40 ^{+0.03} _{-0.03}	0.121 ^{+0.011} _{-0.010}	7.7 ^{+1.6} _{-1.2}	0.18 ^{+0.04} _{-0.04}	yes	3.11	no	...
PG1156-037	sdB	27548 ⁺⁵⁷ ₋₇₅	5.52 ^{+0.01} _{-0.01}	-2.89 ^{+0.03} _{-0.03}	0.196 ^{+0.006} _{-0.006}	20.0 ^{+1.6} _{-1.5}	0.47 ^{+0.08} _{-0.07}	no	1.12	g	single
PG1206+165	sdB	28833 ⁺⁹⁹ ₋₁₀₀	5.58 ^{+0.01} _{-0.01}	-2.44 ^{+0.03} _{-0.03}	0.174 ^{+0.009} _{-0.008}	18.9 ^{+2.2} _{-1.9}	0.42 ^{+0.08} _{-0.07}	yes	2.02	no	...
PG1214+031	sdB	28608 ⁺¹⁰² ₋₁₁₉	5.59 ^{+0.02} _{-0.02}	-2.29 ^{+0.02} _{-0.03}	0.180 ^{+0.008} _{-0.008}	19.5 ^{+2.1} _{-1.8}	0.45 ^{+0.09} _{-0.07}	no	1.11	no	single
PG1219+534	sdB	34886 ⁺⁵¹ ₋₈₅	5.85 ^{+0.01} _{-0.01}	-1.52 ^{+0.01} _{-0.01}	0.139 ^{+0.003} _{-0.003}	25.7 ^{+1.8} _{-1.7}	0.50 ^{+0.09} _{-0.07}	no	0.93	p	single
PG1224+672	sdB	26458 ⁺¹⁸⁶ ₋₁₈₄	4.60 ^{+0.02} _{-0.02}	-1.78 ^{+0.02} _{-0.03}	0.599 ^{+0.023} _{-0.023}	158.3 ^{+15.9} _{-14.2}	0.52 ^{+0.10} _{-0.08}	no	1.15	no	single
PG1230+052	sdB	27317 ⁺⁷⁴ ₋₉₁	5.58 ^{+0.01} _{-0.01}	-2.87 ^{+0.03} _{-0.03}	0.198 ^{+0.006} _{-0.006}	19.6 ^{+1.5} _{-1.4}	0.54 ^{+0.09} _{-0.08}	no	0.98	g	sd+WD
PG1230+067	He-sdO	41939 ⁺¹⁰⁶ ₋₇₃	5.81 ^{+0.03} _{-0.02}	1.39 ^{+0.05} _{-0.05}	0.160 ^{+0.007} _{-0.007}	71.1 ^{+9.6} _{-8.4}	0.60 ^{+0.14} _{-0.11}	no	1.04	no	...
PG1232-136	sdB	27739 ⁺⁸⁰ ₋₉₈	5.73 ^{+0.02} _{-0.01}	-1.40 ^{+0.01} _{-0.02}	0.144 ^{+0.003} _{-0.003}	11.1 ^{+0.7} _{-0.7}	0.43 ^{+0.07} _{-0.06}	no	0.92	no	sd+WD
PG1233+427	sdB	25922 ⁺⁸⁶ ₋₁₀₅	5.53 ^{+0.01} _{-0.01}	-2.56 ^{+0.03} _{-0.03}	0.190 ^{+0.004} _{-0.004}	14.7 ^{+0.9} _{-0.8}	0.44 ^{+0.07} _{-0.06}	no	1.17	g	single
PG1238+515	He-sdO	42618 ⁺¹⁰¹ ₋₇₉	5.92 ^{+0.02} _{-0.03}	1.36 ^{+0.05} _{-0.06}	0.171 ^{+0.007} _{-0.006}	87.0 ^{+10.8} _{-9.6}	0.89 ^{+0.19} _{-0.16}	no	1.01	no	...
PG1241-084	sdB	28648 ⁺⁵⁰ ₋₈₂	5.66 ^{+0.01} _{-0.01}	-2.38 ^{+0.02} _{-0.02}	0.193 ^{+0.003} _{-0.003}	22.6 ^{+1.3} _{-1.2}	0.62 ^{+0.10} _{-0.09}	no	1.14	h	sd+MS
PG1244+113	sdO	37713 ⁺²⁰⁶ ₋₂₇₅	5.65 ^{+0.03} _{-0.03}	-3.50 ^{+0.17} _{-0.23}	0.173 ^{+0.011} _{-0.010}	54.7 ^{+8.0} _{-6.8}	0.49 ^{+0.11} _{-0.09}	no	1.09	...	sd+WD
PG1245-042	BHB	18004 ⁺¹⁰⁸ ₋₇₀	4.36 ^{+0.01} _{-0.01}	-2.40 ^{+0.04} _{-0.04}	0.834 ^{+0.049} _{-0.049}	65.9 ^{+9.7} _{-8.1}	0.58 ^{+0.13} _{-0.10}	no	1.03
PG1247+554	iHe-sdB	31359 ⁺⁷¹ ₋₄₉	6.21 ^{+0.01} _{-0.01}	-0.94 ^{+0.00} _{-0.00}	0.088 ^{+0.002} _{-0.002}	6.7 ^{+0.4} _{-0.4}	0.45 ^{+0.07} _{-0.06}	no	0.72	no	sd+WD
PG1248+164	sdB	26491 ⁺¹⁸ ₋₂₅	5.65 ^{+0.01} _{-0.01}	-2.63 ^{+0.05} _{-0.05}	0.161 ^{+0.006} _{-0.006}	11.5 ^{+1.0} _{-0.9}	0.42 ^{+0.06} _{-0.06}	no	1.09	no	sd+WD
PG1255+547	sdB	34388 ⁺⁷⁵ ₋₁₃₁	5.79 ^{+0.01} _{-0.01}	-1.48 ^{+0.01} _{-0.01}	0.140 ^{+0.008} _{-0.008}	24.6 ^{+2.2} _{-2.8}	0.44 ^{+0.07} _{-0.07}	no	1.02	no	single
PG1256+278	iHe-sdOB	35594 ⁺²⁴³ ₋₁₂₇	5.95 ^{+0.02} _{-0.01}	-0.72 ^{+0.01} _{-0.01}	0.115 ^{+0.005} _{-0.005}	19.0 ^{+2.1} _{-1.9}	0.43 ^{+0.09} _{-0.07}	no	1.06	no	single
PG1257+171	sdB	38131 ⁺¹⁵² ₋₁₇₀	5.98 ^{+0.03} _{-0.03}	-1.65 ^{+0.03} _{-0.03}	0.113 ^{+0.004} _{-0.004}	24.3 ^{+2.5} _{-2.2}	0.45 ^{+0.09} _{-0.08}	no	1.09	no	single
PG1258-030	BHB	15025 ⁺²⁸ ₋₆₃	4.41 ^{+0.01} _{-0.01}	-2.48 ^{+0.09} _{-0.09}	0.922 ^{+0.054} _{-0.054}	39.0 ^{+4.8} _{-4.8}	0.79 ^{+0.14} _{-0.14}	no	1.08
PG1300+279	sdB	28713 ⁺⁶⁸ ₋₉₈	5.44 ^{+0.01} _{-0.01}	-2.73 ^{+0.04} _{-0.04}	0.216 ^{+0.012} _{-0.011}	28.5 ^{+3.6} _{-3.1}	0.46 ^{+0.08} _{-0.08}	no	1.05	no	binary
PG1303-114	sdB	32033 ⁺⁶⁶ ₋₁₀₆	5.83 ^{+0.01} _{-0.01}	-2.63 ^{+0.04} _{-0.04}	0.125 ^{+0.004} _{-0.004}	14.8 ^{+1.1} _{-1.0}	0.39 ^{+0.07} _{-0.06}	no	0.97	no	single
PG1304+491	sdB	32039 ⁺¹³⁵ ₋₁₃₉	5.77 ^{+0.02} _{-0.02}	-1.80 ^{+0.02} _{-0.02}	0.151 ^{+0.004} _{-0.004}	21.6 ^{+1.5} _{-1.4}	0.49 ^{+0.09} _{-0.07}	no	0.98	no	single
PG1325+102	sdB	37083 ⁺⁶³ ₋₈₈	5.88 ^{+0.01} _{-0.01}	-1.70 ^{+0.01} _{-0.01}	0.135 ^{+0.005} _{-0.005}	31.0 ^{+3.1} _{-2.8}	0.50 ^{+0.10} _{-0.08}	no	0.94	p	single
PG1329+159	sdB	27865 ⁺⁷² ₋₈₆	5.44 ^{+0.01} _{-0.01}	-2.93 ^{+0.04} _{-0.04}	0.222 ^{+0.007} _{-0.007}	26.7 ^{+2.2} _{-2.0}	0.49 ^{+0.07} _{-0.07}	no	1.05	no	sd+MS
PG1336-018	sdB	32534 ⁺⁸³ ₋₆₂	5.79 ^{+0.01} _{-0.01}	-3.04 ^{+0.05} _{-0.12}	0.157 ^{+0.005} _{-0.004}	24.9 ^{+1.9} _{-1.7}	0.56 ^{+0.10} _{-0.08}	no	0.98	p	sd+MS
PG1338+481	sdB	27244 ⁺⁴⁵ ₋₂₄	5.42 ^{+0.01} _{-0.01}	-2.84 ^{+0.03} _{-0.03}	0.220 ^{+0.006} _{-0.006}	24.0 ^{+1.8} _{-1.7}	0.46 ^{+0.08} _{-0.07}	no	1.03	g	binary
PG1340+607	sdB	25606 ⁺¹³⁰ ₋₁₅₂	5.30 ^{+0.02} _{-0.02}	-2.62 ^{+0.04} _{-0.04}	0.249 ^{+0.007} _{-0.007}	24.0 ^{+1.9} _{-1.7}	0.45 ^{+0.08} _{-0.07}	yes	1.07	g	...
PG1343-102	sdB	27930 ⁺¹⁰⁷ ₋₁₀₅	5.50 ^{+0.02} _{-0.02}	-3.15 ^{+0.07} _{-0.07}	0.207 ^{+0.008} _{-0.007}	23.4 ^{+2.1} _{-1.9}	0.49 ^{+0.09} _{-0.07}	no	1.12	g	binary
PG1350+372	sdB	23672 ⁺¹⁵² ₋₁₅₂	5.34 ^{+0.02} _{-0.02}	-2.85 ^{+0.04} _{-0.04}	0.215 ^{+0.007} _{-0.007}	13.1 ^{+1.2} _{-1.1}	0.37 ^{+0.07} _{-0.06}	no	1.13	g	single
PG1352-023	sdO	44241 ⁺¹¹⁴ ₋₁₅₄	6.01 ^{+0.01} _{-0.01}	-1.75 ^{+0.00} _{-0.00}	0.103 ^{+0.003} _{-0.003}	36.7 ^{+3.9} _{-3.9}	0.40 ^{+0.07} _{-0.07}	no	1.07	no	single
PG1355-064	He-sdO	61956 ⁺⁴⁹⁷ ₋₄₆₀	5.72 ^{+0.03} _{-0.03}	3.50 ^{+0.53} _{-0.53}	0.198 ^{+0.013} _{-0.013}	521.6 ^{+128.5} _{-128.5}	0.76 ^{+0.15} _{-0.15}	no	1.03
PG1403+316	sdB	30848 ⁺⁶⁶ ₋₁₀₃	5.74 ^{+0.02} _{-0.01}	-2.35 ^{+0.02} _{-0.02}	0.147 ^{+0.004} _{-0.004}	17.6 ^{+1.2} _{-1.2}	0.44 ^{+0.08} _{-0.06}	no	1.04	no	sd+WD
PG1407-013	sdO	38469 ⁺⁹⁰ ₋₂₅₃	5.42 ^{+0.01} _{-0.01}	-3.54 ^{+0.16} _{-0.16}	0.229 ^{+0.011} _{-0.011}	103.7 ^{+13.2} _{-11.5}	0.51 ^{+0.11} _{-0.09}	no	0.97	no	single
PG1408+098	sdB	37849 ⁺¹¹⁹ ₋₂₀₇	5.74 ^{+0.01} _{-0.02}	-1.79 ^{+0.02} _{-0.02}	0.136 ^{+0.005} _{-0.005}	34.2 ^{+3.3} _{-3.3}	0.37 ^{+0.07} _{-0.06}	no	0.96	no	single
PG1415-043	sdB	37225 ⁺⁹² ₋₁₄₂	5.99 ^{+0.02} _{-0.01}	-1.52 ^{+0.01} _{-0.01}	0.113 ^{+0.003} _{-0.003}	22.2 ^{+1.9} _{-1.8}	0.46 ^{+0.09} _{-0.07}	no	0.99	no	single
PG1417+257	sdB	26165 ⁺¹⁰² ₋₁₁₃	5.39 ^{+0.01} _{-0.02}	-2.78 ^{+0.04} _{-0.04}	0.246 ^{+0.010} _{-0.010}	25.6 ^{+2.5} _{-2.2}	0.55 ^{+0.10} _{-0.08}	no	1.14	g	single
PG1426+213	sdB	32941 ⁺¹⁵⁵ ₋₇₇	5.85 ^{+0.03} _{-0.02}	-1.72 ^{+0.02} _{-0.01}	0.124 ^{+0.003} _{-0.003}	16.3 ^{+1.2} _{-1.1}	0.40 ^{+0.06} _{-0.06}	no	1.33	no	single
PG1432+004	sdB	23208 ⁺¹⁵⁵ ₋₁₁₇	5.27 ^{+0.02} _{-0.01}	-2.40 ^{+0.02} _{-0.02}	0.265 ^{+0.009} _{-0.009}	18.3 ^{+1.7} _{-1.5}	0.48 ^{+0.09} _{-0.07}	no	0.94	no	single
PG1432+159	sdB	26001 ⁺⁵⁹ ₋₇₅	5.61 ^{+0.01} _{-0.01}	-2.49 ^{+0.02} _{-0.02}	0.157 ^{+0.005} _{-0.005}	10.2 ^{+0.7} _{-0.7}	0.36 ^{+0.06} _{-0.05}	no	1.01	no	binary
PG1433+239	sdB	27681 ⁺¹²² ₋₁₀₇	5.41 ^{+0.02} _{-0.02}	-3.00 ^{+0.04} _{-0.04}	0.236 ^{+0.008} _{-0.008}	29.4 ^{+2.6} _{-2.3}	0.52 ^{+0.09} _{-0.08}	no	0.92	h	single
PG1438-029	sdB	28223 ⁺¹¹³ ₋₁₅₇	5.52 ^{+0.02} _{-0.02}	-2.94 ^{+0.05} _{-0.05}	0.183 ^{+0.010} _{-0.010}	19.1 ^{+2.6} _{-2.2}	0.40 ^{+0.07} _{-0.07}	no	1.14	no	sd+MS
PG1439-013	sdO	44394 ⁺⁶⁴ ₋₂₆₆	5.63 ^{+0.02} _{-0.02}	-3.48 ^{+0.07} _{-0.07}	0.198 ^{+0.010} _{-0.010}	137.6 ^{+21.9} _{-18.8}	0.61 ^{+0.14} _{-0.11}	no	1.02	no	binary
PG1451+492	sdB	21427 ⁺¹⁴⁸ ₋₁₄₈	4.81 ^{+0.01} _{-0.01}	-2.19 ^{+0.02} _{-0.02}	0.481 ^{+0.016} _{-0.016}	43.9 ^{+3.6} _{-3.6}	0.54 ^{+0.08} _{-0.08}	no	1.00	no	single
PG1452+198	sdB	29034 ⁺⁸⁵ ₋₆₂	5.72 ^{+0.01} _{-0.01}	-1.97 ^{+0.01} _{-0.01}	0.148 ^{+0.003} _{-0.003}	14.1 ^{+0.8} _{-0.8}	0.42 ^{+0.06} _{-0.06}	no	0.69	no	binary
PG1457+193	sdB	37304 ⁺¹⁰ ₋₁₀	5.86 ^{+0.02} _{-0.02}	-1.49 ^{+0.01} _{-0.01}	0.121 ^{+0.004} _{-0.004}	25.8 ^{+2.1} _{-2.1}	0.39 ^{+0.06} _{-0.06}	no	1.04	no	single
PG1458+423	sdB	28972<									

Table D.1: continued.

Star	Type	T_{eff} (K)	$\log g$ (cm s^{-2})	$\log N(\text{He})/N(\text{H})$	R (R_{\odot})	L (L_{\odot})	M (M_{\odot})	IR-excess	<i>Gaia</i> ruwe	Pulsation	Binarity
PG1554+222	He-sdO	64114 $^{+866}_{-920}$	5.45 $^{+0.05}_{-0.05}$	-0.06 $^{+0.03}_{-0.04}$	0.217 $^{+0.014}_{-0.013}$	719.2 $^{+221.4}_{-175.5}$	0.48 $^{+0.13}_{-0.10}$	no	0.98	no	...
PG1604+504	sdB	30566 $^{+99}_{-200}$	5.75 $^{+0.01}_{-0.02}$	-1.60 $^{+0.02}_{-0.02}$	0.132 $^{+0.003}_{-0.003}$	13.8 $^{+0.9}_{-0.9}$	0.36 $^{+0.06}_{-0.05}$	no	0.88	no	single
PG1605+072	sdB	33082 $^{+140}_{-147}$	5.34 $^{+0.01}_{-0.02}$	-2.60 $^{+0.04}_{-0.05}$	0.248 $^{+0.015}_{-0.014}$	66.1 $^{+9.1}_{-7.7}$	0.49 $^{+0.10}_{-0.09}$	no	0.55	p	single
PG1607+174	iHe-sdB	29882 $^{+189}_{-244}$	5.19 $^{+0.03}_{-0.03}$	-0.48 $^{+0.02}_{-0.02}$	0.302 $^{+0.013}_{-0.012}$	65.4 $^{+6.5}_{-5.9}$	0.51 $^{+0.10}_{-0.09}$	no	0.94	no	single
PG1610+519	sdO	43897 $^{+297}_{-263}$	5.54 $^{+0.02}_{-0.03}$	-3.14 $^{+0.10}_{-0.09}$	0.175 $^{+0.011}_{-0.010}$	102.6 $^{+17.6}_{-15.1}$	0.39 $^{+0.09}_{-0.08}$	yes	1.98	no	...
PG1610+529	sdB	29195 $^{+132}_{-128}$	5.64 $^{+0.02}_{-0.02}$	-2.23 $^{+0.03}_{-0.03}$	0.162 $^{+0.004}_{-0.004}$	17.1 $^{+1.1}_{-1.0}$	0.41 $^{+0.07}_{-0.06}$	no	0.91	no	binary
PG1613+426	sdB	36279 $^{+205}_{-291}$	5.76 $^{+0.04}_{-0.04}$	-1.61 $^{+0.03}_{-0.03}$	0.142 $^{+0.005}_{-0.005}$	31.3 $^{+3.0}_{-2.7}$	0.42 $^{+0.07}_{-0.07}$	no	1.04	p	single
PG1616+144	sdB	37063 $^{+67}_{-10}$	5.87 $^{+0.01}_{-0.01}$	-1.49 $^{+0.01}_{-0.00}$	0.130 $^{+0.003}_{-0.003}$	28.7 $^{+2.2}_{-2.1}$	0.46 $^{+0.08}_{-0.07}$	no	0.97	no	binary
PG1618+563	sdB	35405 $^{+81}_{-227}$	5.83 $^{+0.01}_{-0.02}$	-1.69 $^{+0.02}_{-0.02}$	0.145 $^{+0.007}_{-0.007}$	29.8 $^{+3.3}_{-3.3}$	0.52 $^{+0.11}_{-0.09}$	yes	1.98	p	...
PG1619+522	sdB	32605 $^{+97}_{-265}$	5.80 $^{+0.02}_{-0.02}$	-2.03 $^{+0.03}_{-0.03}$	0.132 $^{+0.003}_{-0.003}$	17.7 $^{+1.2}_{-1.2}$	0.40 $^{+0.07}_{-0.06}$	no	1.10	no	sd+WD
PG1626+471	sdB	29662 $^{+97}_{-203}$	5.54 $^{+0.02}_{-0.02}$	-3.03 $^{+0.06}_{-0.08}$	0.197 $^{+0.005}_{-0.005}$	27.0 $^{+2.0}_{-1.9}$	0.50 $^{+0.09}_{-0.07}$	no	0.96	no	single
PG1627+017	sdB	23573 $^{+64}_{-129}$	5.34 $^{+0.01}_{-0.01}$	-2.94 $^{+0.03}_{-0.03}$	0.239 $^{+0.006}_{-0.006}$	15.8 $^{+1.2}_{-1.1}$	0.45 $^{+0.08}_{-0.07}$	no	0.67	g	binary
PG1627+112	sdB	26466 $^{+219}_{-213}$	5.21 $^{+0.03}_{-0.03}$	-2.78 $^{+0.07}_{-0.07}$	0.169 $^{+0.011}_{-0.010}$	12.6 $^{+1.9}_{-1.6}$	0.17 $^{+0.04}_{-0.03}$	no	2.27
PG1629+081	sdO	43145 $^{+259}_{-152}$	5.32 $^{+0.02}_{-0.02}$	-2.98 $^{+0.06}_{-0.06}$	0.237 $^{+0.011}_{-0.011}$	176.1 $^{+24.8}_{-21.6}$	0.43 $^{+0.10}_{-0.08}$	no	0.68	...	binary
PG1629+466	He-sdO	38711 $^{+10}_{-18}$	5.89 $^{+0.01}_{-0.01}$	0.79 $^{+0.01}_{-0.01}$	0.136 $^{+0.004}_{-0.004}$	37.6 $^{+3.4}_{-3.1}$	0.53 $^{+0.10}_{-0.08}$	no	1.06	no	...
PG1632+088	BHB	13869 $^{+64}_{-73}$	3.92 $^{+0.03}_{-0.02}$	-2.21 $^{+0.10}_{-0.09}$	1.384 $^{+0.075}_{-0.075}$	63.9 $^{+8.6}_{-7.3}$	0.59 $^{+0.13}_{-0.10}$	no	0.97
PG1633+099	sdB	28889 $^{+117}_{-98}$	5.54 $^{+0.02}_{-0.02}$	-2.66 $^{+0.06}_{-0.06}$	0.206 $^{+0.007}_{-0.007}$	26.7 $^{+2.4}_{-2.2}$	0.54 $^{+0.10}_{-0.08}$	no	1.01	...	single
PG1634+061	sdB	30014 $^{+10}_{-10}$	5.60 $^{+0.01}_{-0.01}$	-2.65 $^{+0.06}_{-0.06}$	0.117 $^{+0.005}_{-0.005}$	10.0 $^{+1.1}_{-1.0}$	0.20 $^{+0.04}_{-0.03}$	no	2.78
PG1635+414	sdB	26126 $^{+44}_{-124}$	5.40 $^{+0.02}_{-0.02}$	-2.83 $^{+0.05}_{-0.05}$	0.201 $^{+0.006}_{-0.006}$	17.0 $^{+1.3}_{-1.2}$	0.37 $^{+0.07}_{-0.05}$	no	1.22	g	binary
PG1647+253	sdB	36073 $^{+219}_{-215}$	5.84 $^{+0.03}_{-0.03}$	-2.08 $^{+0.06}_{-0.06}$	0.104 $^{+0.005}_{-0.005}$	16.6 $^{+2.1}_{-1.9}$	0.28 $^{+0.06}_{-0.05}$	yes	1.42	no	...
PG1654+138	BHB	17524 $^{+88}_{-266}$	3.87 $^{+0.05}_{-0.03}$	-2.43 $^{+0.07}_{-0.07}$	1.584 $^{+0.157}_{-0.132}$	215.2 $^{+50.0}_{-38.1}$	0.68 $^{+0.15}_{-0.15}$	no	0.88
PG1701+359	sdB	33152 $^{+95}_{-101}$	5.55 $^{+0.01}_{-0.01}$	-4.00 $^{+0.00}_{-0.00}$	0.157 $^{+0.010}_{-0.010}$	26.8 $^{+5.0}_{-3.5}$	0.32 $^{+0.06}_{-0.06}$	yes	3.51	no	...
PG1705+537	BHB	20864 $^{+168}_{-168}$	4.58 $^{+0.01}_{-0.01}$	-2.35 $^{+0.03}_{-0.03}$	0.776 $^{+0.030}_{-0.030}$	103.1 $^{+9.8}_{-9.8}$	0.84 $^{+0.16}_{-0.13}$	no	0.99
PG1708+602	sdO	62936 $^{+462}_{-438}$	5.72 $^{+0.02}_{-0.02}$	-0.82 $^{+0.01}_{-0.01}$	0.151 $^{+0.007}_{-0.007}$	320.7 $^{+92.1}_{-74.5}$	0.44 $^{+0.10}_{-0.08}$	no	1.03	no	single
PG1710+490	sdB	29290 $^{+88}_{-10}$	5.61 $^{+0.01}_{-0.01}$	-2.47 $^{+0.02}_{-0.02}$	0.168 $^{+0.004}_{-0.003}$	18.6 $^{+1.1}_{-1.1}$	0.41 $^{+0.07}_{-0.06}$	no	0.77	no	single
PG1716+426	sdB	26587 $^{+103}_{-103}$	5.44 $^{+0.01}_{-0.01}$	-2.95 $^{+0.04}_{-0.04}$	0.199 $^{+0.005}_{-0.005}$	17.8 $^{+1.2}_{-1.1}$	0.40 $^{+0.07}_{-0.06}$	no	1.01	g	sd+WD
PG1722+286	sdB	37387 $^{+131}_{-181}$	6.04 $^{+0.03}_{-0.02}$	-1.75 $^{+0.02}_{-0.02}$	0.112 $^{+0.002}_{-0.002}$	22.1 $^{+1.6}_{-1.5}$	0.51 $^{+0.10}_{-0.08}$	no	1.02	no	single
PG1725+252	sdB	27894 $^{+50}_{-106}$	5.44 $^{+0.01}_{-0.01}$	-3.02 $^{+0.06}_{-0.06}$	0.217 $^{+0.005}_{-0.005}$	25.8 $^{+1.7}_{-1.6}$	0.48 $^{+0.08}_{-0.07}$	no	0.95	no	binary
PG1738+505	sdB	29784 $^{+167}_{-176}$	5.41 $^{+0.02}_{-0.02}$	-1.84 $^{+0.02}_{-0.02}$	0.227 $^{+0.005}_{-0.005}$	36.4 $^{+2.5}_{-2.4}$	0.48 $^{+0.08}_{-0.07}$	no	0.99	no	single
PG1739+489	sdB	26304 $^{+92}_{-106}$	5.42 $^{+0.01}_{-0.01}$	-2.84 $^{+0.03}_{-0.03}$	0.216 $^{+0.006}_{-0.005}$	20.2 $^{+1.4}_{-1.3}$	0.45 $^{+0.07}_{-0.06}$	no	1.10	g	binary
PG1743+477	sdB	26731 $^{+21}_{-10}$	5.49 $^{+0.01}_{-0.01}$	-2.16 $^{+0.02}_{-0.02}$	0.200 $^{+0.004}_{-0.004}$	18.4 $^{+1.2}_{-1.1}$	0.45 $^{+0.07}_{-0.06}$	no	1.10	g	sd+WD
PG2111+023	MS-B	16050 $^{+155}_{-112}$	4.43 $^{+0.02}_{-0.02}$	-1.27 $^{+0.04}_{-0.04}$	1.996 $^{+0.224}_{-0.224}$	239.0 $^{+75.7}_{-51.9}$	3.90 $^{+1.43}_{-0.98}$	no	0.95
PG2151+100	sdB	33946 $^{+93}_{-10}$	5.61 $^{+0.01}_{-0.01}$	-3.66 $^{+0.19}_{-0.17}$	0.219 $^{+0.022}_{-0.018}$	57.2 $^{+12.5}_{-9.6}$	0.71 $^{+0.20}_{-0.15}$	yes	2.17	no	...
PG2158+082	He-sdO	62500 $^{+14}_{-34}$	5.86 $^{+0.04}_{-0.04}$	1.75 $^{+0.02}_{-0.02}$	0.191 $^{+0.013}_{-0.012}$	498.7 $^{+153.0}_{-121.4}$	0.96 $^{+0.24}_{-0.20}$	yes	0.94	no	...
PG2159+051	MS-B	17112 $^{+212}_{-313}$	3.98 $^{+0.04}_{-0.04}$	-2.25 $^{+0.06}_{-0.06}$	3.996 $^{+0.764}_{-0.764}$	1225.2 $^{+430.3}_{-340.3}$	5.61 $^{+4.23}_{-2.07}$	no	0.91
PG2213-006	He-sdO	47238 $^{+121}_{-223}$	5.88 $^{+0.03}_{-0.03}$	0.80 $^{+0.06}_{-0.04}$	0.209 $^{+0.012}_{-0.012}$	196.4 $^{+38.5}_{-32.1}$	1.20 $^{+0.30}_{-0.24}$	no	1.04	no	...
PG2223+143	sdB	36521 $^{+169}_{-175}$	5.32 $^{+0.02}_{-0.02}$	-2.64 $^{+0.05}_{-0.05}$	0.207 $^{+0.018}_{-0.018}$	69.0 $^{+15.9}_{-12.0}$	0.33 $^{+0.09}_{-0.07}$	no	1.53	no	...
PG2303+019	sdB	36839 $^{+59}_{-65}$	5.77 $^{+0.02}_{-0.02}$	-1.71 $^{+0.03}_{-0.03}$	0.119 $^{+0.014}_{-0.011}$	23.7 $^{+6.0}_{-4.4}$	0.31 $^{+0.10}_{-0.07}$	yes	1.03	p	...
PG2304+193	He-sdO	48749 $^{+242}_{-294}$	5.86 $^{+0.04}_{-0.04}$	0.81 $^{+0.15}_{-0.09}$	0.176 $^{+0.021}_{-0.021}$	158.1 $^{+60.0}_{-40.5}$	0.82 $^{+0.35}_{-0.24}$	no	0.96
PG2314+076	sdB	27188 $^{+10}_{-10}$	5.69 $^{+0.01}_{-0.01}$	-3.91 $^{+0.11}_{-0.09}$	0.140 $^{+0.003}_{-0.003}$	9.7 $^{+0.6}_{-0.6}$	0.35 $^{+0.06}_{-0.05}$	no	1.20	no	single
PG2317+046	sdO	44970 $^{+176}_{-175}$	6.05 $^{+0.02}_{-0.02}$	-2.82 $^{+0.04}_{-0.04}$	0.125 $^{+0.004}_{-0.004}$	57.5 $^{+7.8}_{-7.0}$	0.64 $^{+0.14}_{-0.11}$	yes	0.93	no	...
PG2321+214	He-sdO	40431 $^{+82}_{-82}$	5.71 $^{+0.02}_{-0.02}$	2.13 $^{+0.08}_{-0.09}$	0.179 $^{+0.007}_{-0.007}$	77.5 $^{+9.0}_{-8.1}$	0.61 $^{+0.11}_{-0.11}$	no	1.03	no	...
PG2337+070	sdB	29894 $^{+115}_{-115}$	5.76 $^{+0.01}_{-0.01}$	-2.04 $^{+0.02}_{-0.02}$	0.153 $^{+0.003}_{-0.003}$	16.9 $^{+1.0}_{-1.0}$	0.49 $^{+0.07}_{-0.07}$	no	1.08	no	binary
PG2345+318	sdB	26118 $^{+10}_{-10}$	5.57 $^{+0.01}_{-0.01}$	-2.58 $^{+0.03}_{-0.03}$	0.181 $^{+0.006}_{-0.006}$	13.7 $^{+1.1}_{-1.0}$	0.44 $^{+0.08}_{-0.06}$	no	1.04	no	sd+WD
PG2349+002	sdB	27502 $^{+106}_{-144}$	5.69 $^{+0.01}_{-0.01}$	-3.78 $^{+0.10}_{-0.10}$	0.154 $^{+0.003}_{-0.003}$	12.2 $^{+0.8}_{-0.7}$	0.42 $^{+0.07}_{-0.06}$	no	1.07	no	single
PG2351+198	BHB	17155 $^{+102}_{-102}$	4.25 $^{+0.01}_{-0.01}$	-2.25 $^{+0.04}_{-0.04}$	0.868 $^{+0.061}_{-0.061}$	58.9 $^{+8.5}_{-8.5}$	0.49 $^{+0.09}_{-0.09}$	no	1.13
PG2352+181	He-sdO	46004 $^{+242}_{-242}$	5.91 $^{+0.01}_{-0.01}$	1.28 $^{+0.09}_{-0.09}$	0.188 $^{+0.008}_{-0.008}$	143.0 $^{+19.6}_{-19.6}$	1.04 $^{+0.19}_{-0.19}$	no	0.93	no	...
PG2356+167	iHe-sdB	23152 $^{+304}_{-304}$	4.99 $^{+0.03}_{-0.03}$	-0.68 $^{+0.01}_{-0.01}$	0.367 $^{+0.022}_{-0.022}$	34.5 $^{+5.4}_{-4.5}$	0.48 $^{+0.09}_{-0.09}$	no	1.09	no	single
PG2358+107	sdB	26830 $^{+93}_{-93}$	5.56 $^{+0.01}_{-0.01}$	-2.69 $^{+0.03}_{-0.03}$	0.183 $^{+0.005}_{-0.005}$	15.7 $^{+1.1}_{-1.0}$	0.44 $^{+0.07}_{-0.06}$	no	1.13	g	binary
PHL1079	sdB	32910 $^{+209}_{-28}$	5.60 $^{+0.01}_{-0.02}$	-2.19 $^{+0.04}_{-0.05}$	0.123 $^{+0.011}_{-0.011}$	16.0 $^{+3.6}_{-2.9}$	0.22 $^{+0.06}_{-0.05}$	yes	4.67	no	...
PHL1548	sdB	39381 $^{+118}_{-152}$	5.89 $^{+0.02}_{-0.02}$	-1.88 $^{+0.03}_{-0.03}$	0.121 $^{+0.$						

Table D.1: continued.

Star	Type	T_{eff} (K)	$\log g$ (cm s^{-2})	$\log N(\text{He})/N(\text{H})$	R (R_{\odot})	L (L_{\odot})	M (M_{\odot})	IR-excess	<i>Gaia</i> r _{uwe}	Pulsation	Binarity
TIC396954061	sdB	34682 ⁺⁸⁴ ₋₁₉₃	5.92 ^{+0.01} _{-0.01}	-1.70 ^{+0.02} _{-0.02}	0.134 ^{+0.004} _{-0.004}	23.3 ^{+1.9} _{-1.8}	0.54 ^{+0.10} _{-0.08}	no	1.15	p	single
TIC437043466	sdB	28811 ⁺³⁶ ₋₁₂₆	5.56 ^{+0.01} _{-0.01}	-2.98 ^{+0.04} _{-0.04}	0.197 ^{+0.006} _{-0.005}	24.0 ^{+1.8} _{-1.6}	0.51 ^{+0.09} _{-0.07}	no	0.60	h	single
TIC95765924	sdB	35464 ⁺⁸⁹ ₋₆₁	5.79 ^{+0.01} _{-0.01}	-1.69 ^{+0.02} _{-0.02}	0.141 ^{+0.005} _{-0.005}	28.2 ^{+2.6} _{-2.4}	0.45 ^{+0.08} _{-0.07}	no	1.10	no	single
TON357	sdO	65722 ⁺⁸⁰⁶ ₋₇₇₀	5.94 ^{+0.03} _{-0.03}	-1.85 ^{+0.03} _{-0.03}	0.101 ^{+0.009} _{-0.007}	170.7 ^{+56.7} _{-43.5}	0.32 ^{+0.07} _{-0.07}	yes	1.51	no	...
TON835	sdO	54691 ⁺⁴⁶⁴ ₋₅₃₉	5.93 ^{+0.02} _{-0.03}	-2.20 ^{+0.04} _{-0.04}	0.117 ^{+0.007} _{-0.006}	110.7 ^{+32.0} _{-25.8}	0.43 ^{+0.10} _{-0.08}	no	1.10	no	single
TYC1773-399-1	sdB	34434 ⁺⁸⁷ ₋₁₂₁	5.85 ^{+0.01} _{-0.01}	-1.66 ^{+0.02} _{-0.02}	0.141 ^{+0.003} _{-0.003}	25.2 ^{+1.6} _{-1.5}	0.51 ^{+0.09} _{-0.07}	no	1.20	no	single
TYC1943-2305-1	MS-B	19178 ⁺¹⁰¹ ₋₇₇	4.67 ^{+0.01} _{-0.01}	-2.45 ^{+0.04} _{-0.04}	1.820 ^{+0.255} _{-0.200}	404.0 ^{+123.7} _{-85.6}	5.72 ^{+2.01} _{-1.39}	no	0.93
TYC1961-572-1	MS-B	15558 ⁺⁹² ₋₁₀₉	4.36 ^{+0.02} _{-0.02}	-2.36 ^{+0.08} _{-0.08}	3.130 ^{+1.089} _{-0.643}	516.8 ^{+424.3} _{-191.6}	8.24 ^{+7.00} _{-3.18}	no	1.07
TYC3449-677-1	sdO	42461 ⁺¹²⁷ ₋₂₁₄	5.49 ^{+0.01} _{-0.02}	-3.26 ^{+0.06} _{-0.06}	0.220 ^{+0.010} _{-0.010}	141.5 ^{+19.8} _{-17.3}	0.55 ^{+0.12} _{-0.10}	no	0.64	no	single
TYC4121-1326-1	BHB	16350 ⁺¹⁶² ₋₁₅₀	4.39 ^{+0.03} _{-0.02}	-2.25 ^{+0.05} _{-0.05}	0.720 ^{+0.027} _{-0.026}	33.4 ^{+3.4} _{-3.0}	0.47 ^{+0.09} _{-0.07}	no	0.86
TYC4406-285-1	sdB	25246 ⁺⁴⁹ ₋₈₂	5.59 ^{+0.01} _{-0.01}	-4.00 ^{+0.08} _{-0.09}	0.164 ^{+0.002} _{-0.002}	9.8 ^{+0.5} _{-0.5}	0.38 ^{+0.06} _{-0.05}	no	0.90	no	single
Ton930	sdB	26854 ⁺⁷⁶ ₋₁₂₃	5.54 ^{+0.02} _{-0.02}	-2.50 ^{+0.02} _{-0.02}	0.223 ^{+0.010} _{-0.010}	23.6 ^{+2.5} _{-2.2}	0.64 ^{+0.12} _{-0.10}	no	1.03	no	binary
US719	sdB	26141 ⁺²⁷ ₋₅₈	5.40 ^{+0.01} _{-0.01}	-2.50 ^{+0.01} _{-0.01}	0.224 ^{+0.007} _{-0.006}	21.0 ^{+1.6} _{-1.5}	0.46 ^{+0.08} _{-0.07}	no	0.66	g	single
CW83 0512-08	iHe-sdOB	38320 ⁺²²⁴ ₋₁₃₅	5.84 ^{+0.03} _{-0.05}	-0.88 ^{+0.01} _{-0.01}	0.118 ^{+0.002} _{-0.002}	27.1 ^{+2.1} _{-1.9}	0.35 ^{+0.07} _{-0.06}	no	1.36	no	single
CW83 0711+22	He-sdO	40226 ⁺⁶⁶ ₋₄₉	5.69 ^{+0.02} _{-0.02}	1.60 ^{+0.04} _{-0.04}	0.175 ^{+0.005} _{-0.005}	72.6 ^{+6.8} _{-6.3}	0.55 ^{+0.11} _{-0.09}	no	0.97	no	...
CW83 0825+15	iHe-sdOB	37189 ⁺⁹⁰ ₋₁₀₈	5.92 ^{+0.02} _{-0.02}	-0.51 ^{+0.01} _{-0.01}	0.130 ^{+0.003} _{-0.003}	29.1 ^{+2.1} _{-2.0}	0.51 ^{+0.09} _{-0.08}	no	1.18	yes	single
CW83 0832-01	He-sdO	46312 ⁺¹⁴⁴ ₋₂₂₅	5.96 ^{+0.04} _{-0.04}	1.02 ^{+0.08} _{-0.04}	0.184 ^{+0.006} _{-0.005}	140.1 ^{+20.0} _{-17.9}	1.14 ^{+0.26} _{-0.21}	no	1.19	no	...
CW83 0904-02	He-sdO	48687 ⁺¹¹⁵ ₋₁₃₃	5.98 ^{+0.02} _{-0.03}	0.98 ^{+0.06} _{-0.06}	0.199 ^{+0.008} _{-0.007}	200.0 ^{+35.3} _{-30.6}	1.39 ^{+0.31} _{-0.25}	no	0.99	no	...
CW83 1735+22	sdO	42593 ⁺¹⁶⁰ ₋₁₆₈	5.54 ^{+0.01} _{-0.02}	-3.08 ^{+0.04} _{-0.05}	0.185 ^{+0.005} _{-0.005}	101.1 ^{+11.0} _{-10.0}	0.43 ^{+0.09} _{-0.07}	no	1.35	no	sd+WD
CW83 1758+36	sdB	32250 ⁺⁹⁰ ₋₁₃₆	5.77 ^{+0.01} _{-0.02}	-1.63 ^{+0.01} _{-0.01}	0.127 ^{+0.002} _{-0.002}	15.8 ^{+0.9} _{-0.8}	0.35 ^{+0.06} _{-0.05}	no	1.07	no	sd+MS
Balloon082000001	BHB	20955 ⁺²²⁸ ₋₁₃₇	4.87 ^{+0.02} _{-0.02}	-1.00 ^{+0.01} _{-0.01}	0.403 ^{+0.012} _{-0.012}	28.3 ^{+2.5} _{-2.2}	0.44 ^{+0.07} _{-0.07}	no	0.95
PG1400+389	BHB	19182 ⁺¹¹⁰ ₋₉₉	4.79 ^{+0.02} _{-0.02}	-0.74 ^{+0.03} _{-0.03}	0.480 ^{+0.014} _{-0.014}	28.1 ^{+2.4} _{-2.2}	0.52 ^{+0.10} _{-0.08}	no	1.04	g	...
FBS1531+381	sdB	28774 ⁺⁵⁵ ₋₆₁	5.63 ^{+0.01} _{-0.02}	-2.43 ^{+0.02} _{-0.02}	0.180 ^{+0.004} _{-0.004}	20.0 ^{+1.4} _{-1.3}	0.51 ^{+0.09} _{-0.07}	no	0.99	no	sd+MS
KIC002697388	sdB	25099 ⁺¹³⁰ ₋₁₂₆	5.53 ^{+0.02} _{-0.02}	-2.88 ^{+0.04} _{-0.04}	0.198 ^{+0.008} _{-0.007}	14.0 ^{+1.3} _{-1.2}	0.48 ^{+0.09} _{-0.07}	no	1.03	g	single
KIC003527751	sdB	28122 ⁺⁸⁴ ₋₁₁₂	5.52 ^{+0.01} _{-0.01}	-3.00 ^{+0.04} _{-0.04}	0.216 ^{+0.009} _{-0.009}	26.3 ^{+2.6} _{-2.3}	0.57 ^{+0.10} _{-0.09}	no	1.11	h	single
KIC007668647	sdB	28016 ⁺⁷⁵ ₋₈₉	5.63 ^{+0.01} _{-0.02}	-2.67 ^{+0.04} _{-0.03}	0.187 ^{+0.008} _{-0.008}	19.4 ^{+2.0} _{-1.7}	0.54 ^{+0.10} _{-0.08}	no	1.04	g	sd+WD
KIC008054179	iHe-sdOB	38428 ⁺¹⁰⁶ ₋₈₄	5.86 ^{+0.02} _{-0.04}	-0.87 ^{+0.01} _{-0.01}	0.114 ^{+0.002} _{-0.002}	25.5 ^{+2.0} _{-1.9}	0.34 ^{+0.06} _{-0.06}	no	0.98	no	single
KIC010001893	sdB	27811 ⁺⁵¹ ₋₆₉	5.57 ^{+0.01} _{-0.01}	-2.94 ^{+0.04} _{-0.04}	0.186 ^{+0.012} _{-0.012}	18.7 ^{+3.1} _{-2.5}	0.47 ^{+0.11} _{-0.09}	no	1.02	g	single
KIC010139564	sdB	32947 ⁺¹¹⁴ ₋₁₄₂	5.82 ^{+0.02} _{-0.02}	-2.29 ^{+0.03} _{-0.03}	0.161 ^{+0.011} _{-0.010}	27.4 ^{+4.2} _{-3.5}	0.62 ^{+0.14} _{-0.11}	no	1.08	p	single
KIC011558725	sdB	27900 ⁺¹¹⁹ ₋₁₁₃	5.54 ^{+0.02} _{-0.02}	-3.30 ^{+0.07} _{-0.07}	0.196 ^{+0.008} _{-0.007}	21.0 ^{+2.0} _{-1.8}	0.48 ^{+0.09} _{-0.07}	no	1.10	g	sd+WD
LSIV-14°116	iHe-sdOB	35174 ⁺⁶² ₋₅₀	5.88 ^{+0.01} _{-0.01}	-0.66 ^{+0.01} _{-0.00}	0.121 ^{+0.004} _{-0.004}	20.4 ^{+1.7} _{-1.6}	0.41 ^{+0.07} _{-0.06}	no	0.85	g	single
PG1427+196	He-sdO	49932 ⁺¹³³ ₋₁₉₁	6.00 ^{+0.02} _{-0.04}	0.58 ^{+0.05} _{-0.04}	0.190 ^{+0.013} _{-0.011}	203.1 ^{+46.2} _{-37.8}	1.32 ^{+0.33} _{-0.27}	no	1.00

Notes. Uncertainties on the atmospheric parameters (T_{eff} , $\log g$, and, $\log N(\text{He})/N(\text{H})$) are only statistical.

Appendix E: Additional Figures

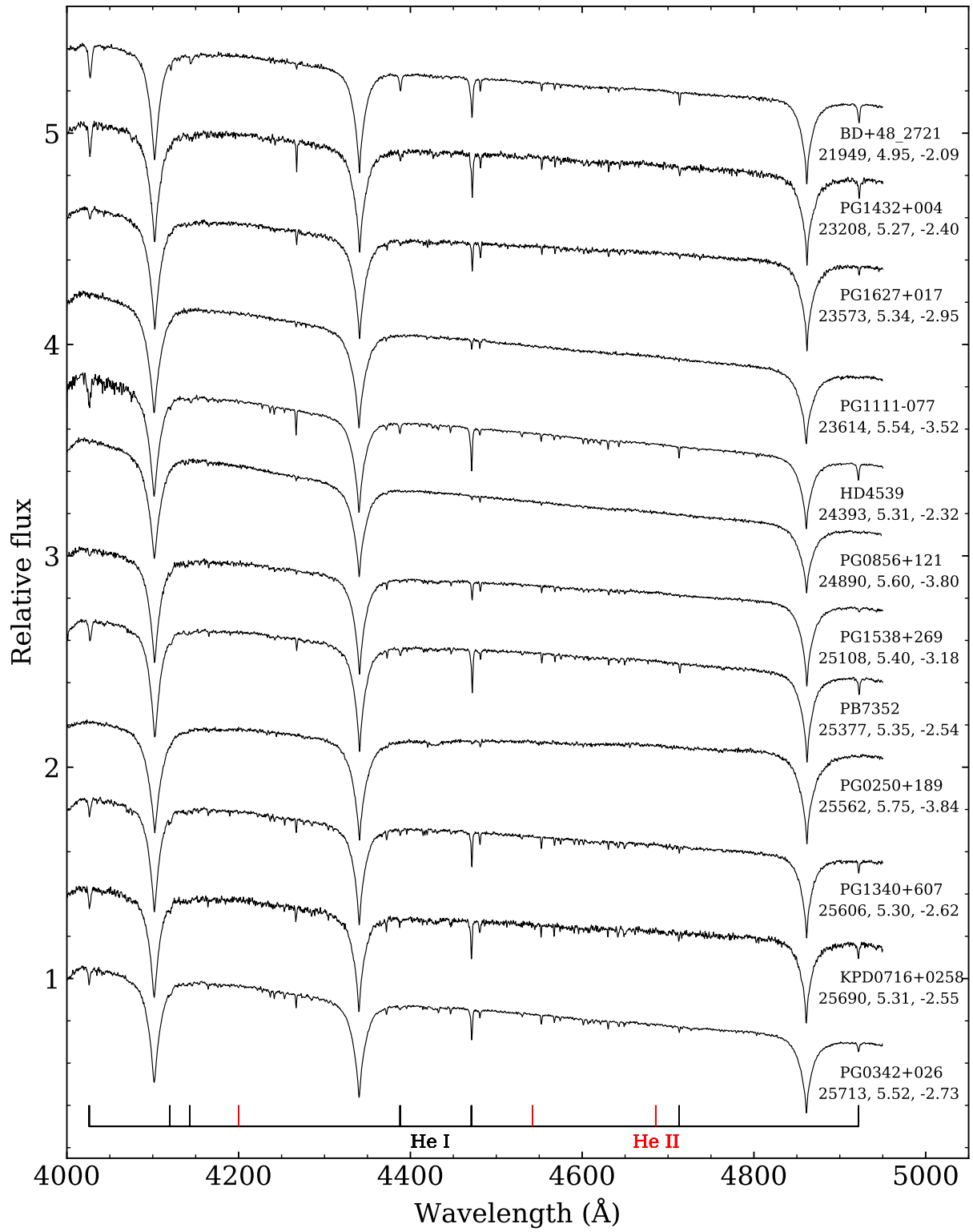


Fig. E.1: MMT spectra of all stars in the MMT sample ordered by increasing T_{eff} . Under the name of each star, we indicate the T_{eff} , $\log g$, and helium abundance ($\log N(\text{He})/N(\text{H})$) of the stars, obtained from the fit of their Bok spectrum. None of the stars is sufficiently hot and He-rich to display the He II lines at 4200 Å and 4542 Å. The spectra of the most reddened stars, show a small diffuse interstellar band absorption around 4450 Å. Examples are PG0250+189, PG0215+183 and some of the KPD objects.

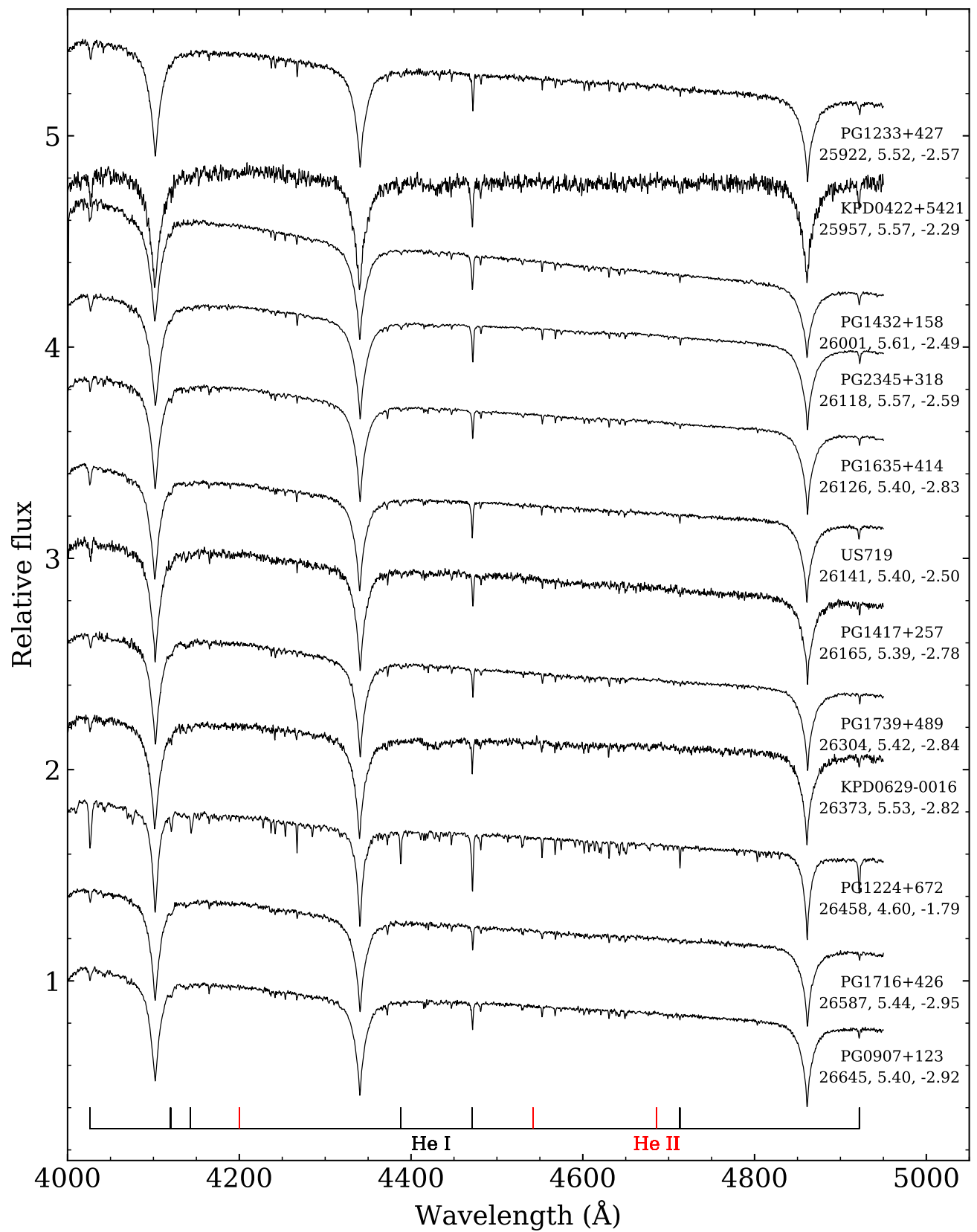


Fig. E.1: Continued.

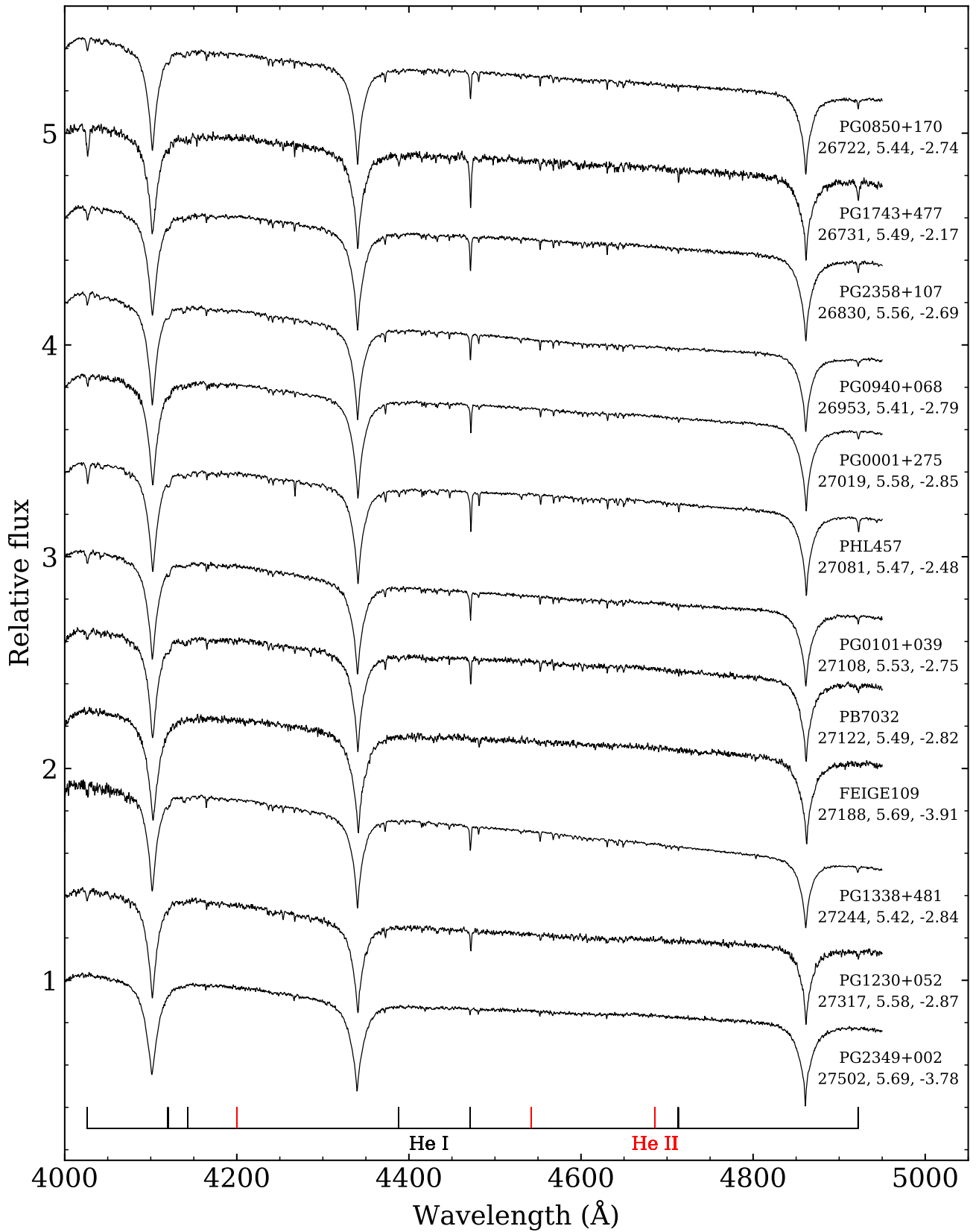


Fig. E.1: Continued.

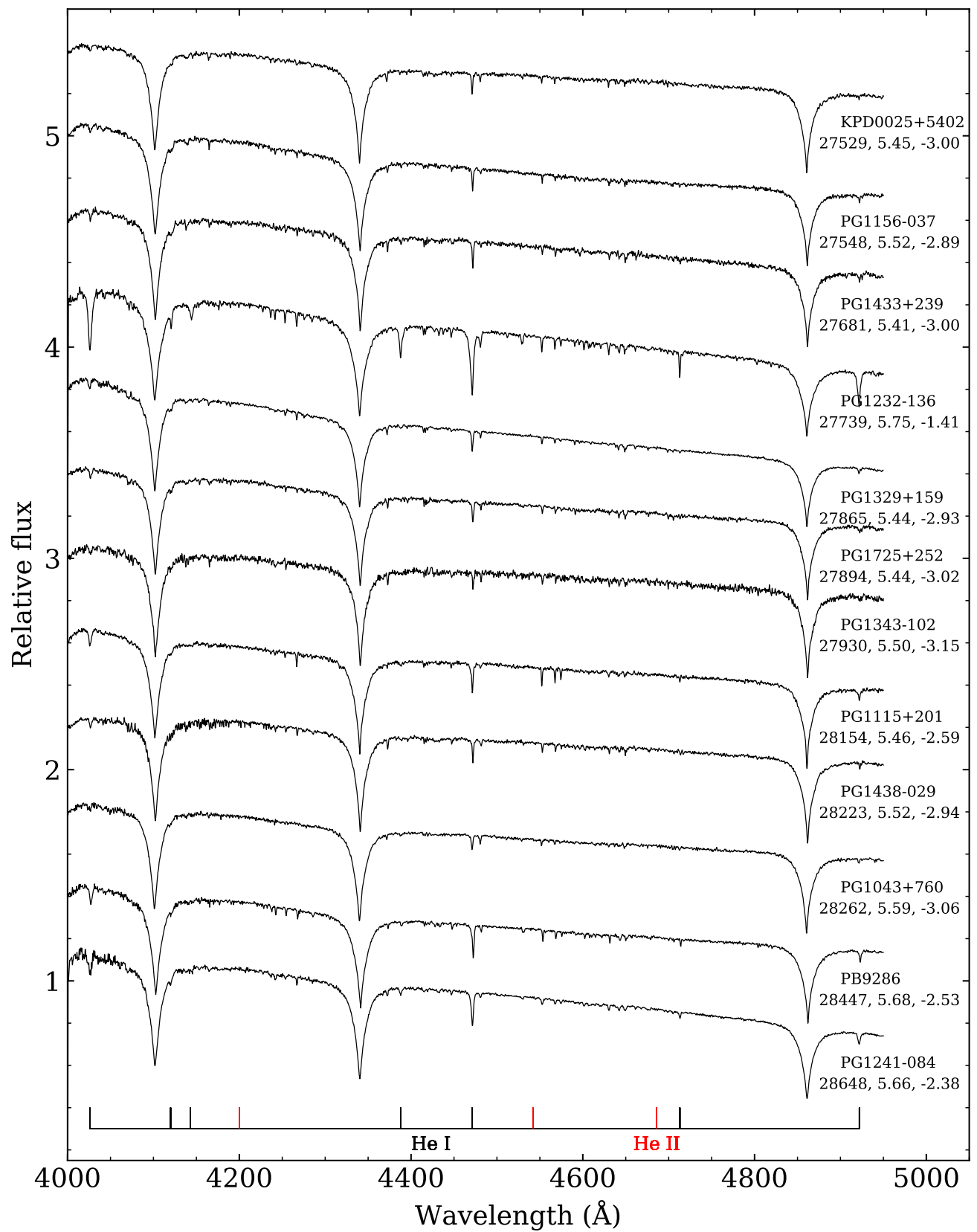


Fig. E.1: Continued.

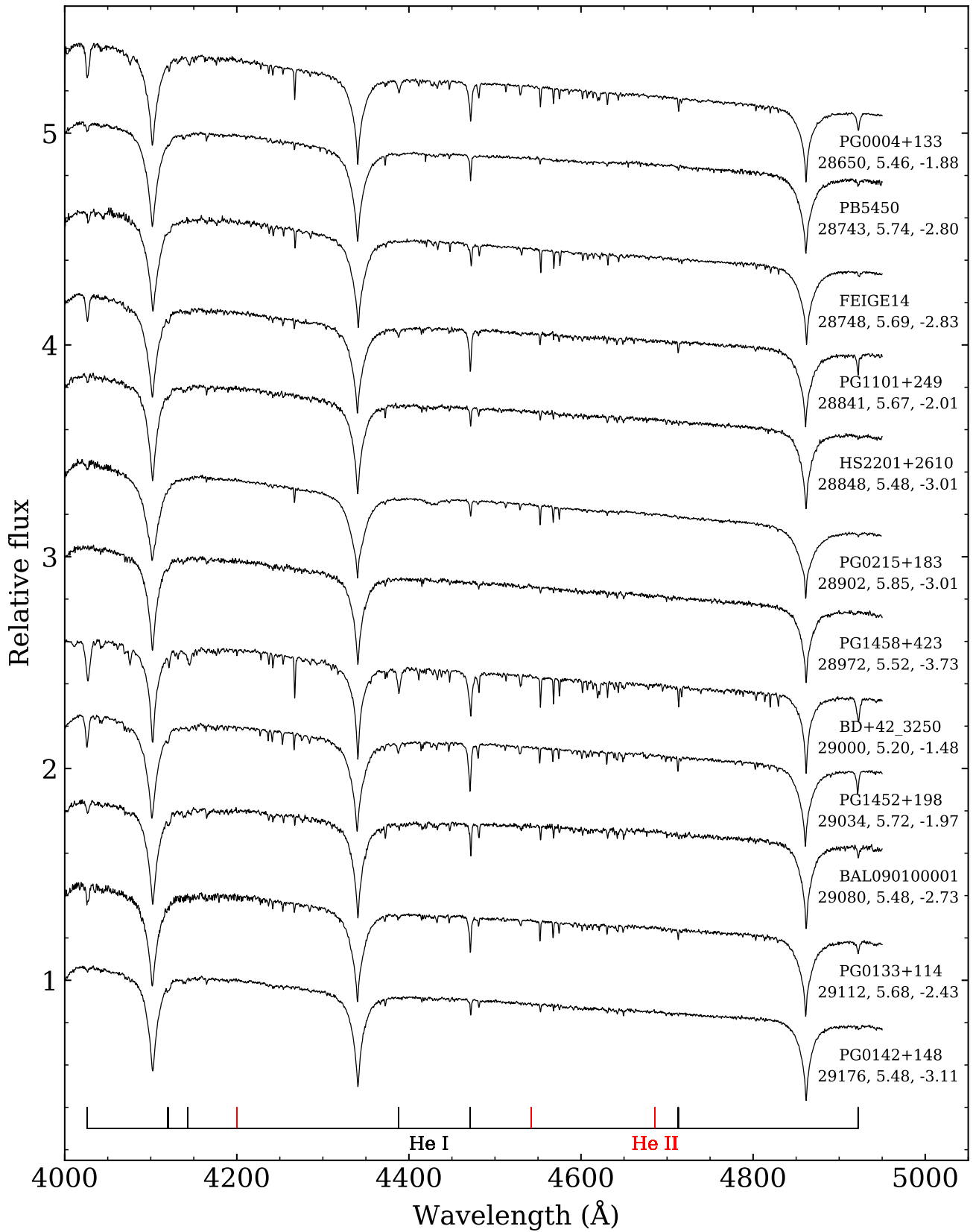


Fig. E.1: Continued.

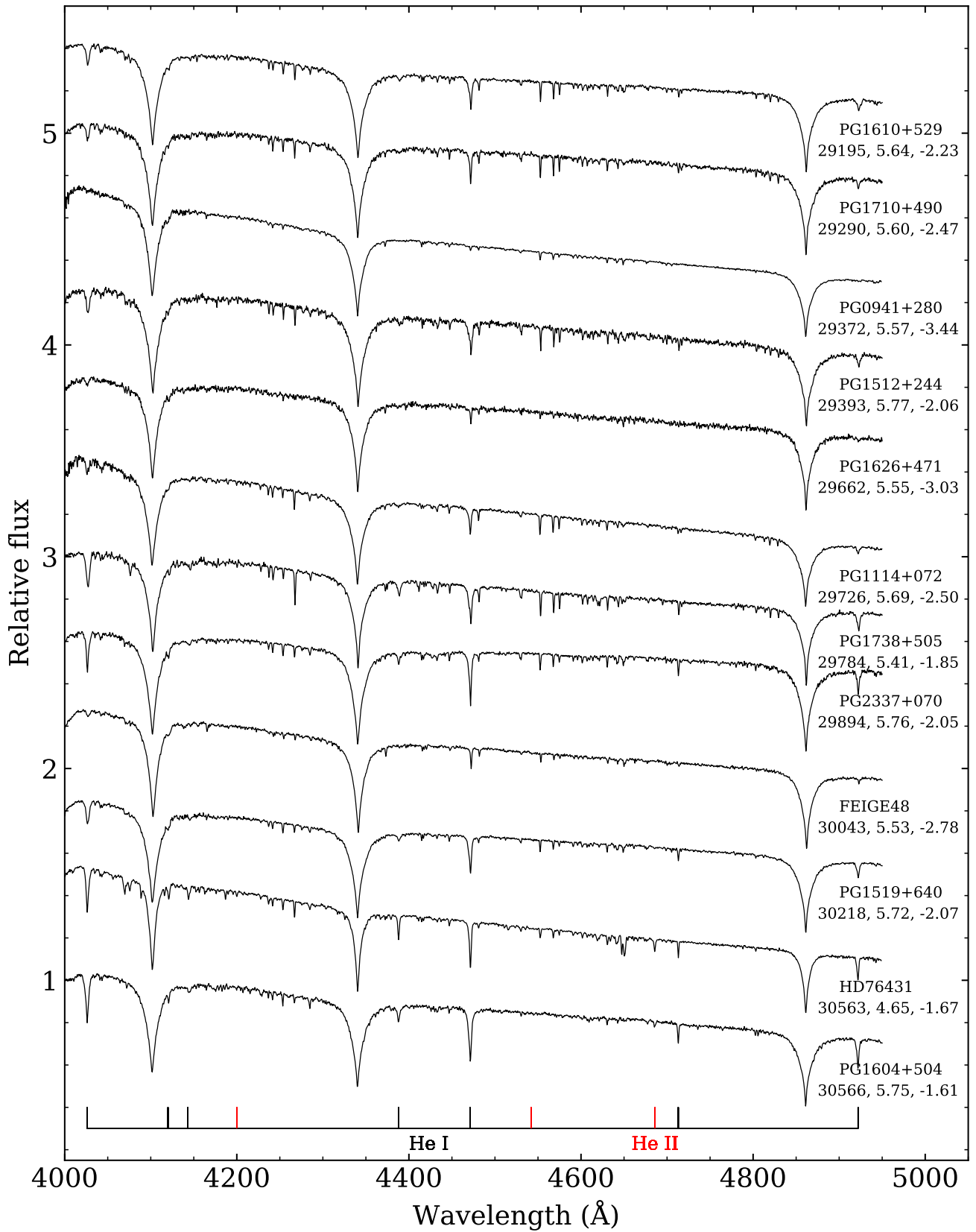


Fig. E.1: Continued.

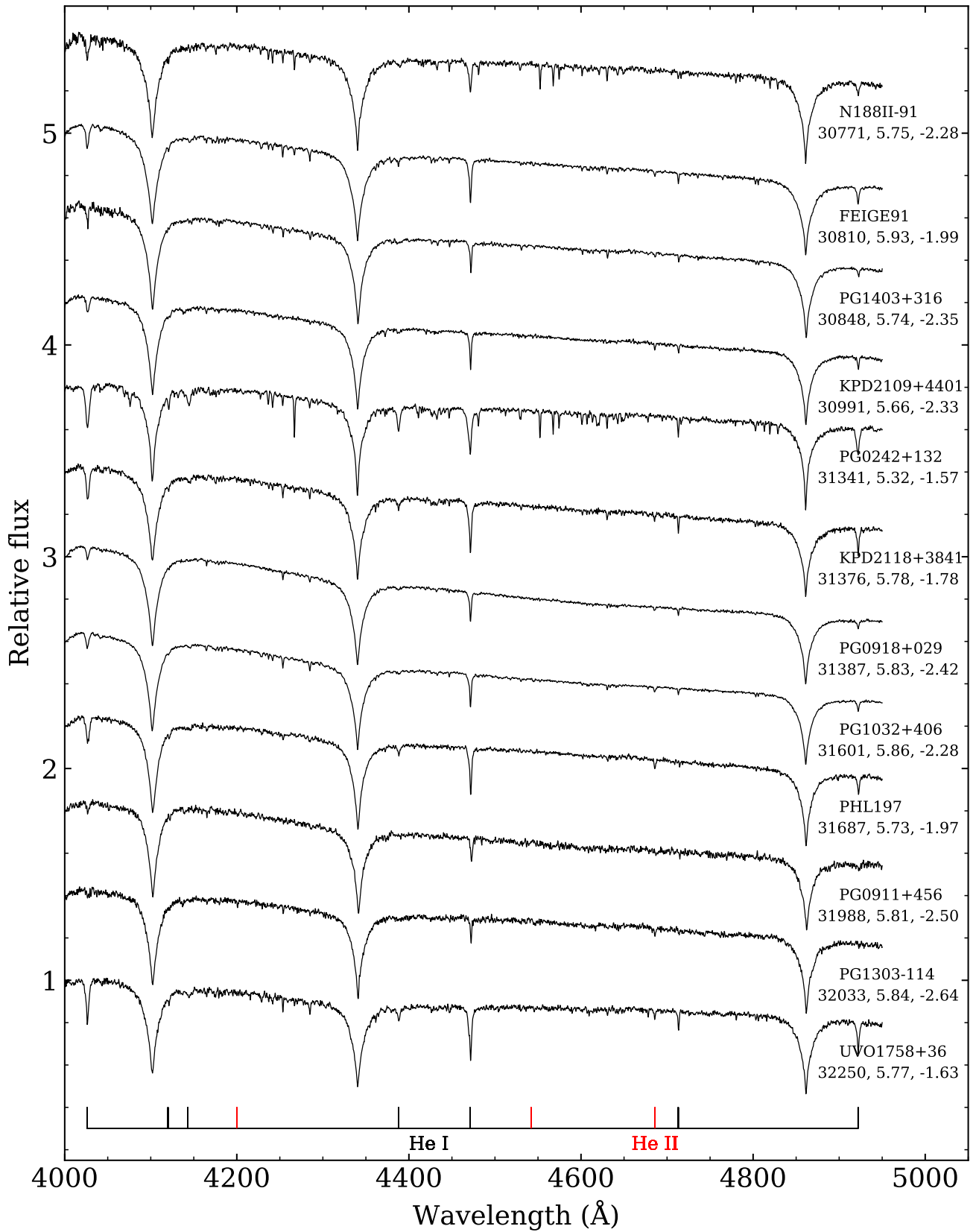


Fig. E.1: Continued.

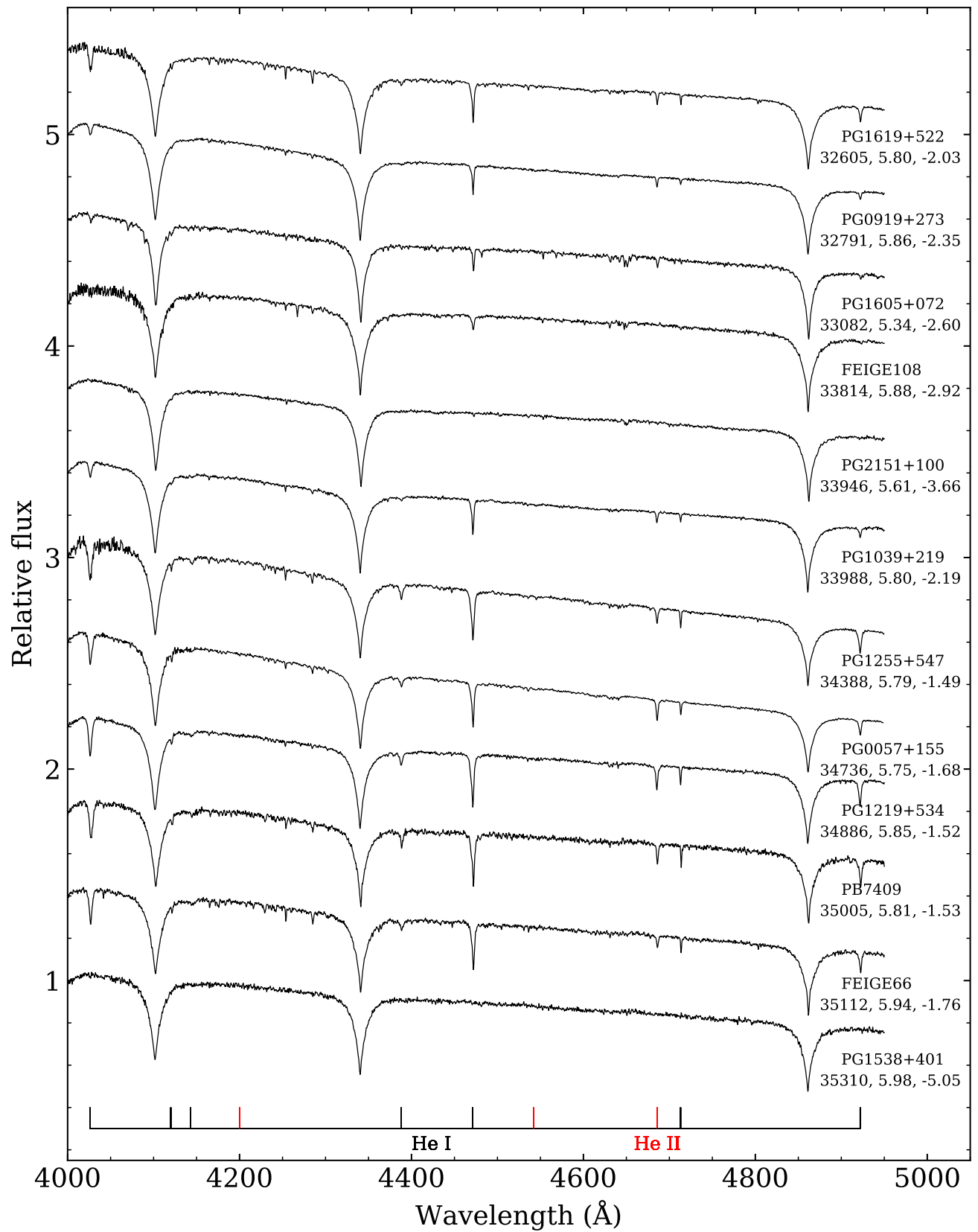


Fig. E.1: Continued.

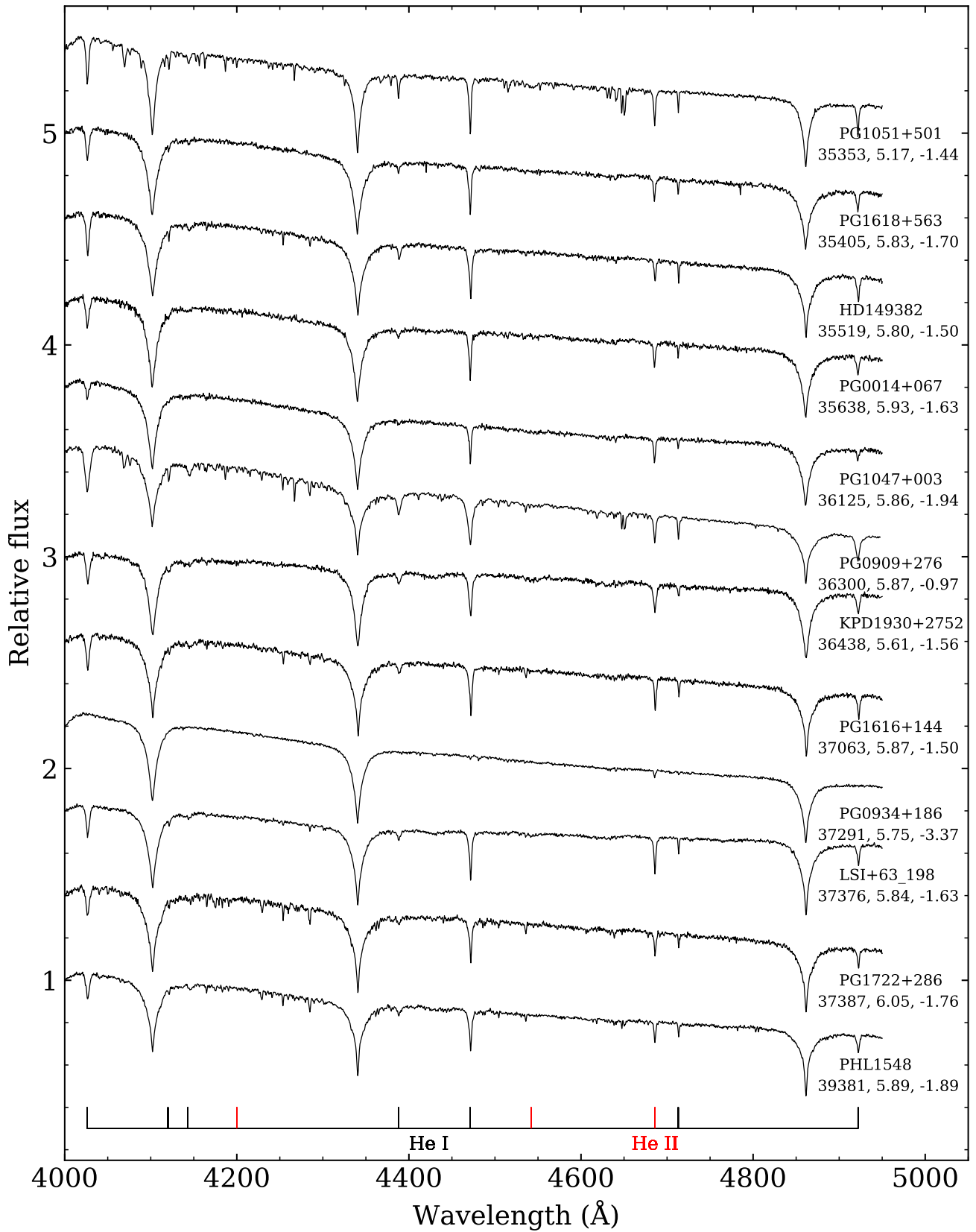


Fig. E.1: Continued.

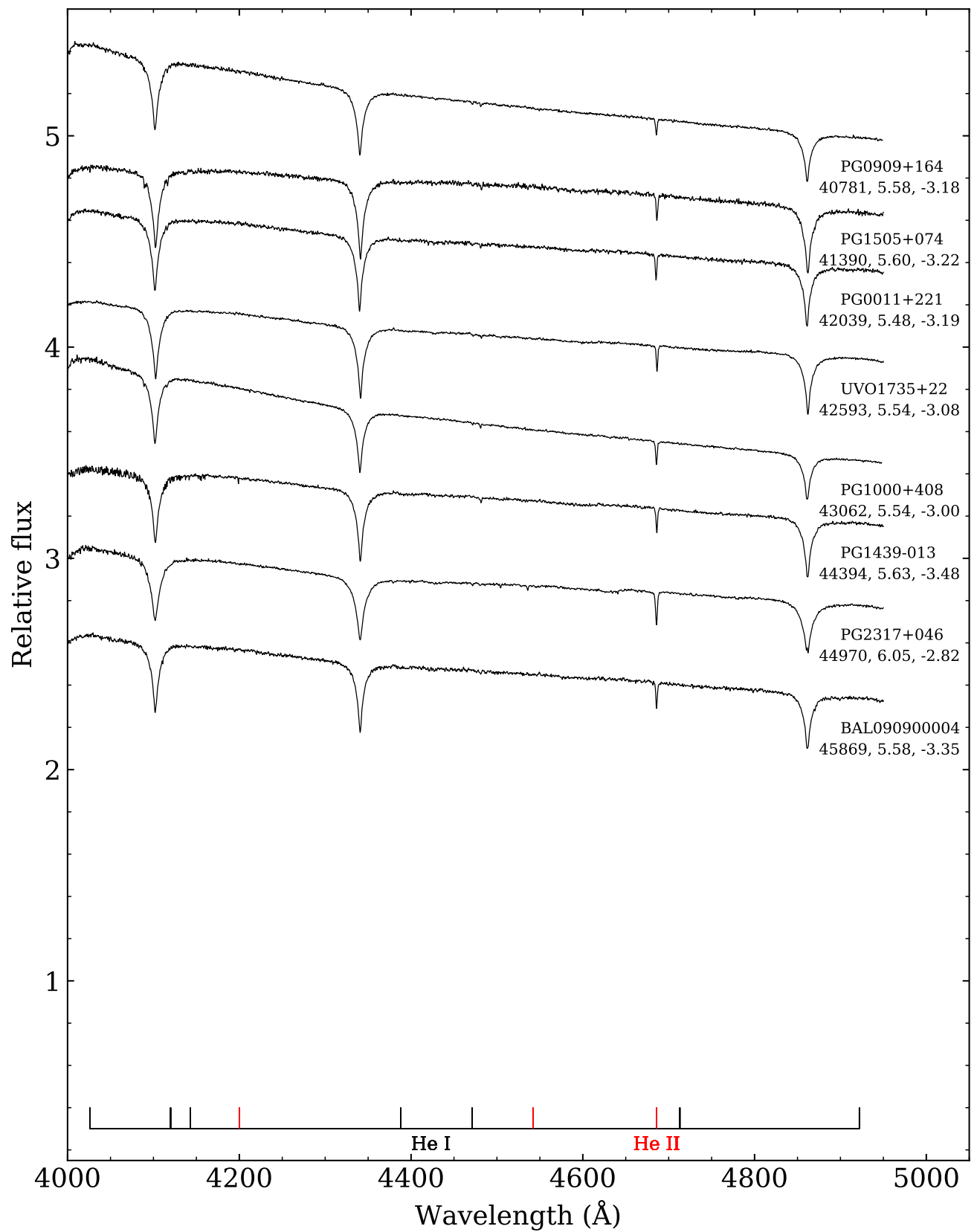


Fig. E.1: Continued.